Springer Theses
Recognizing Outstanding Ph.D. Research

Alejandro Cámara

Optical Beam Characterization via Phase-Space Tomography

Springer

Springer Theses

Recognizing Outstanding Ph.D. Research

Aims and Scope

The series "Springer Theses" brings together a selection of the very best Ph.D. theses from around the world and across the physical sciences. Nominated and endorsed by two recognized specialists, each published volume has been selected for its scientific excellence and the high impact of its contents for the pertinent field of research. For greater accessibility to non-specialists, the published versions include an extended introduction, as well as a foreword by the student's supervisor explaining the special relevance of the work for the field. As a whole, the series will provide a valuable resource both for newcomers to the research fields described, and for other scientists seeking detailed background information on special questions. Finally, it provides an accredited documentation of the valuable contributions made by today's younger generation of scientists.

Theses are accepted into the series by invited nomination only and must fulfill all of the following criteria

- They must be written in good English.
- The topic should fall within the confines of Chemistry, Physics, Earth Sciences, Engineering and related interdisciplinary fields such as Materials, Nanoscience, Chemical Engineering, Complex Systems and Biophysics.
- The work reported in the thesis must represent a significant scientific advance.
- If the thesis includes previously published material, permission to reproduce this must be gained from the respective copyright holder.
- They must have been examined and passed during the 12 months prior to nomination.
- Each thesis should include a foreword by the supervisor outlining the significance of its content.
- The theses should have a clearly defined structure including an introduction accessible to scientists not expert in that particular field.

More information about this series at http://www.springer.com/series/8790

Alejandro Cámara

Optical Beam Characterization via Phase-Space Tomography

Doctoral Thesis accepted by
the Complutense University of Madrid, Spain

Springer

Author
Dr. Alejandro Cámara
Departamento de Óptica
Complutense University of Madrid
Madrid
Spain

Supervisors
Prof. Tatiana Alieva
Departamento de Óptica
Complutense University of Madrid
Madrid
Spain

Prof. María Luisa Calvo Padilla
Departamento de Óptica
Complutense University of Madrid
Madrid
Spain

ISSN 2190-5053 ISSN 2190-5061 (electronic)
Springer Theses
ISBN 978-3-319-19979-5 ISBN 978-3-319-19980-1 (eBook)
DOI 10.1007/978-3-319-19980-1

Library of Congress Control Number: 2015942790

Springer Cham Heidelberg New York Dordrecht London

Printed on acid-free paper

Springer International Publishing AG Switzerland is part of Springer Science+Business Media (www.springer.com)

To mom

Supervisor's Foreword

Light characterization is the basis for the development of numerous instruments and techniques in science and technology. The analysis of the parameters defining light spectral content, polarization, intensity distribution and statistics provides valuable information about the light source, the medium where light propagates, and the object from which light is scattered. The more light characteristics are available the more detailed description of the process or object under study is obtained. While the measurements of some characteristics are well established, the identification of light statistical properties is still a challenging task. However, spatial and temporal coherence are becoming prominent for data acquisition and transmission because they provide additional degrees of freedom to be exploited. A famous historical example illustrating the relevance of light statistics is found in astronomy where the size of a star was estimated from the measurement of the degree of spatial coherence of the light emitted by the star using a stellar Michelson interferometer. Modern temporal and/or spatial coherence inspired techniques include optical coherence tomography, where a low (temporal) coherence source is used for formation of three-dimensional images, ghost imaging, coherence controlled microscopy, holography and lithography. Moreover, partially coherent light has been found beneficial for free-space optical communications and inertial confinement fusion.

Further exploration of the advantages of partially coherent light requires the development of efficient techniques and optical systems for its characterization. This problem is rather difficult because even in the scalar quasi-monochromatic case and under hypothesis of Gaussian statistics, a two-dimensional beam is described in paraxial approximation by a four-dimensional function called mutual intensity (MI), which is also referred to as equal-time mutual coherence function. The MI gauges the correlation of the field at two points. Alternatively, the Wigner distribution (WD) or Ambiguity function can be used for beam description. Neither of these functions can be measured directly and have to be reconstructed from the interference or diffraction patterns. While interferometry is the original technique used for coherence analysis, it proves inefficient for analysis of two-dimensional

beams. Diffraction-based coherence characterization methods, which have been developed during the past three decades, are less known and rarely explained in optics books. However, I believe that at least one of these methods—phase-space tomography—is worth the attention of the scientific community since it has great potential for practical applications. It is my pleasure to write this foreword to Alejandro Cámara's thesis-book devoted to the development of different phase-space tomographic methods supported by experimental set-ups. His work serves as an excellent introduction to phase-space optics of classical light for readers inexperienced in this topic. I believe the book is interesting for any scientist working in this field thanks to Álex's original contributions.

Phase-space tomography is based on two concepts: the rotation of beam WD during beam propagation through ABCD systems and the fact that the WD projection corresponds to the intensity distribution at the output of such ABCD system. Although phase-space tomography has been established more than 20 years ago, it is not widely used for beam coherence analysis due to three principal reasons: the lack of a robust and easily controlled optical setup for rapid acquisition of the required WD projections, the computational complexities of processing the considerable number of projections required, and the difficulties in the further analysis of the resulting four-dimensional functions. Álex was able to find practical solutions for all these theoretical and experimental problems. He has demonstrated that the beam symmetry can significantly simplify the beam analysis process and therefore the corresponding experimental set-up. Álex's proposal for the characterization of a general (asymmetric) beam is worth a special mention. Based on WD projection diversity he was able to find the optimal projection set and order of projection acquisition that allows measuring, processing and analyzing the experimental data concurrently. Three experimental set-ups suitable for the measurement of WD projections have been proposed and experimentally verified. Two of them use spatial light modulators for the implementation of digital lenses. They can be digitally aligned and adjusted to the desired kind and number of projection measurements. The application of spatial light modulators also allows fast video-rate acquisition of the WD projections of two-dimensional beams. The team's contribution to Álex's work are acknowledged in the thesis but I would like to underline the importance of previous work of Dr. Jose Rodrigo in designing, building and testing phase-space rotator devices, which were adapted by Álex for the acquisition of appropriate WD projections. I hope that the readers enjoy this thesis-book, which I consider a guide to understanding and applying the phase-space tomography beam characterization techniques. Finally, it is worth mentioning that the developed software for processing experimental data is released under an open source license in github.com/SoyYuma/gico-core.

Madrid
April 2015

Prof. Tatiana Alieva

Abstract

Partially coherent light enhances the results of many applications originally proposed for coherent light. For example, it reduces the speckle caused by laser light in microscopy, improving the quality of image. In optical communications, partially coherent beams are more robust against channel noise and increase the information throughput.

Despite all their advantages, partially coherent beams are still not widely used. The major drawback preventing its full adoption is the lack of appropriate methods for the complete characterization of partially coherent beams. Many techniques have been proposed to address this problem. Some of them have succeeded for particular cases, like beams satisfying certain symmetries, but none has been demonstrated to be suitable for real-world applications involving 2D partially coherent beams with arbitrary spatial structure.

This thesis establishes four techniques to efficiently characterize partially coherent optical beams, providing meaningful information about the beam coherence state in a timely manner. Three methods rely on exploiting beam symmetries to simplify the characterization process. The fourth method addresses the general case, where there are no beam symmetries to exploit. It provides incremental information of the spatial structure of an a priori unknown beam. All techniques are accompanied by suitable optical system for their experimental execution.

Acknowledgments

The research carried out in this thesis, as with all successful projects, has been developed thanks to the aid of multiple people. Foremost, I would like to express my sincere gratitude to my advisors, Prof. Tatiana Alieva for her continuous support, patience, and motivation and Prof. María Luisa Calvo for convincing me of doing a Ph.D. in Optics. Besides my advisors, I would want to thank the research group GICO, with a special mention to Dr. José A. Rodrigo for his enlightening discussions. My sincere love goes to my family, in special my mother, who always believed I could be whatever I wanted to be, and Maru, whose emotional support and stability was essential during the Ph.D. period. Finally, I would like to acknowledge the financial support of the Spanish national research projects TEC2008-04105, TEC2011-23629, and of the Consejería de Educación de la Comunidad de Madrid and the European Social Fund.

Contents

Chapter 1
Introduction

Within the classical framework, light is an electromagnetic wave composed by the superposition of wave contributions generated by random processes. As such, light must be treated as a stochastic process itself. In the context of optical beams—quasi-monochromatic highly-directional linearly-polarized light waves with visible mean wavelength—the contributions from random processes are so numerous that they follow Gaussian statistics. Therefore, the beam can be completely described by its mutual intensity (MI), the function that establishes the correlation between the wave field at two points, which in the paraxial approximation belong to the plane transverse to the beam propagation [Goo00]. When there is a perfect correlation between the wave field at any pair of points, light is spatially coherent; when there is no correlation at all, light is spatially incoherent. These two situations are limit cases for spatially partially coherent beams, for which the correlation is not perfect nor inexistant, but partial.

Even though partially coherent light enhance the results of many applications originally proposed for coherent light, like digital holography microscopy [Dub99] and free-space optical communications [Ric03, Wan08], it is not widely used. The major drawback preventing its full adoption is the lack of appropriate methods for its complete characterization, i.e. determining its MI. Many interferometric and diffractive techniques have been proposed to experimentally retrieve the MI. Some of them have succeeded for particular cases, like beams satisfying certain symmetries, or by making strong assumptions on the beam coherence model. Nevertheless, none of them has been demonstrated to be suitable for real-world applications involving 2D partially coherent beams with arbitrary spatial structure.

Young double-slit interferometer [Zer38] was probably the first technique that allowed the experimental determination of the MI of an optical beam. It consists in spatially dividing the beam by means of an opaque mask with two apertures. The beams emerging from the mask, corresponding in approximation to the light perturbation at the aperture points, interfere forming a fringe pattern or interferogram. The correlation between the field at the aperture positions is proportional to the fringe visibility in the interferogram. Sadly, obtaining the MI by means of the Young experiment presents three inconveniences:

A. Cámara, *Optical Beam Characterization via Phase-Space Tomography*,
Springer Theses, DOI 10.1007/978-3-319-19980-1_1

1. it is cumbersome since the measurement has to be repeated for every pair of points of the plane where the beam coherence is analyzed,
2. it is energetically inefficient since the light from each aperture spreads over the entire measurement plane, and
3. the geometry and size of the mask apertures affect the results.

Modern interferometric techniques are more convenient, but still do not provide a solution for a general case. Consider, for example, using a reversed-wavefront Young interferometer [San06] or a non-redundant array of apertures as proposed in [Gon11]. Although the methods require a significantly smaller amount of measurements, the problem of energy efficiency and interferogram alteration are still present. Other methods, based on shearing interferometers [Ito86, Iac96, Men98, Mar99] look more promising. Since they do not use a blocking mask with apertures, they conserve beam energy and prevent interferogram alterations. Unfortunately, they are only convenient for the analysis of one-dimensional (1D) profiles of beams. Their trivial 2D generalizations are as cumbersome as the original Young interferometer.

There are alternatives to interferometric techniques to recover the MI of optical beams. For instance, it was recently proposed in [Cho12] a method which consists in measuring the intensity distribution of a beam propagating in free space for two situations: with and without a planar phase mask covering part of its path. The MI between the beam at any pair of points centered at the phase mask edge can be obtained from the difference between the two intensity measurements by a simple Fourier transform. Despite its robustness and simplicity, it has not been yet proved suitable for the characterization of 2D beams.

Instead of defining the beam by its MI, it is possible to rely on equivalent descriptions like the Wigner distribution (WD) or the ambiguity function (AF). The advantage of these alternative functions is that they can be experimentally recovered from intensity measurements applying a technique called phase-space tomography (PST) [Ray94]. Although the method requires a large amount of intensity measurements and an intensive data processing, its suitability has been demonstrated for some simplified situations. For instance, successful PST methods have been proposed for 1D beams [Men96], rotationally invariant beams [Dra00, Aga00], and beams which are almost incoherent [Wal12] or composed by a small number of incoherent modes [Tia12]. Nevertheless, the experimental feasibility of PST is yet to be demonstrated for 2D beams of arbitrary spatial structure.

Based on PST, this book proposes several original techniques for beam coherence state characterization. This includes a novel procedure to recover the MI of 2D beams of arbitrary spatial structure that is demonstrated on several examples involving partially coherent light. In addition, other original techniques for characterizing optical beams satisfying certain symmetry conditions are proposed and experimentally demonstrated. All methods are coherence-agnostic—they do not rely on the beam having a particular coherence spatial structure—and include a verification procedure of the symmetry hypothesis, if any. The proposed techniques are experimentally demonstrated using custom optical systems designed or modified for the thesis goal.

The book is structured as follows. In the rest of this chapter we present the foundations that support the methods proposed in the book. In particular, we introduce fractional Fourier transform PST, a general method for reconstructing the beam WD. It consists in measuring WD projections—beam intensity distributions measured at the output of optical systems that perform the rotation the beam WD in phase space—and applying a tomographic reconstruction algorithm like the filtered back-projection algorithm. We also introduce the fractional Fourier transform (FRFT), a theoretical and optical tool to perform a crucial type of rotation of the beam WD. All proposed methods rely on an optical system that implements a FRFT processor to measure the required WD projections, also called fractional power spectra due to its relation with the FRFT.

Chapter 2 considers the Radon-Wigner display (RWD), an optical system that allows characterizing 1D signals by registering in a single measurement all of the needed beam fractional power spectra, also known as full-range Radon-Wigner transform (RWT). We introduce our own implementation of a RWD setup that is based on spatial light modulators (SLMs). Not only the recovered beam information resulting from a conventional usage of our RWD is comparable to the results from analogical RWDs, but in addition, the versatility of SLMs allows the applications of other characterization schemes.

On the one hand, we propose a scheme for which multiple measurements of different parts of the beam fractional power spectra are assembled into a single full-range RWT. This results in a recovered WD with increased resolution, as is demonstrated in the experimental reconstruction of a test signal. On the other hand, the RWD can be used to measure a narrow region of the beam fractional power spectra. This increases the resolution of the region of interest with respect of a regular measurement of the full fractional power spectra. This is specially useful for the retrieval of beam characteristics that are localised in a certain region the beam RWT, like the chirp parameters of a multi-chirp signal.

Chapter 3 presents a method that is suitable for the recovery of the coherence picture of beams that are separable in Cartesian coordinates. We demonstrate that in such case the antisymmetrical fractional power spectra of the beam are sufficient for a complete coherence characterization. In addition, we show that a simple system formed by assemblies of two cylindrical lenses is convenient for taking the required measurements. We demonstrate the experimental feasibility of the technique by characterizing a Hermite-Gaussian (HG) beam, which is a widely used example of separable beam. Finally, we propose a experimental test to determine if an unknown beam is separable in Cartesian coordinates.

Chapter 4 proposes a novel technique for characterization of beams that are rotationally symmetric, i.e. beams whose MI is invariant respect to rotations of the transverse plane. Completely and partially coherent optical vortices are the most notorious examples of rotationally symmetric beams (RSBs). We prove that, as in the case of beams separable in Cartesian coordinates, the antisymmetric fractional power is spectra is sufficient for the characterization of the coherence state of RSBs. Using the optical setup based on conventional cylindrical lenses that can be used for the analysis of separable beams, we demonstrate the feasibility of the method

in numerical simulations and an experiment. As in the case of separable beams, we propose a simple test to determine if a beam is rotationally symmetric. This method together with the optical system are the subject of an application patent.

Although the techniques for separable and RSBs are considerably different, we show that both require the same reduced set of fractional power spectra associated with the antisymmetrical FRFT. We demonstrate that this provides an enormous advantage compared to the general PST method. In particular, the number of measurements reduces from N^2 in the general case to N in the separable case and $N/2$ in the rotationally symmetric case.

The general method that we propose in Chap. 5 is called phase-space tomographic coherenscopy (PSTC) because it recovers the coherence information of the beam. We designed it with two ideas in mind. First, to take advantage of concurrency to perform multiple processes at a time. Second, to provide the coherence information incrementally, i.e. not all measured data has to be processed to obtain some coherence information. The resulting technique utilises non-standard WD projections that allows recovering the MI of 1D beam profiles contained in parallel lines of the transverse plane. While we would need to gather N^2 intensity distributions to recover this information using Young interferometer, only N measurements are required following our technique. Moreover, we overcome the typical problems for interferometric measurements such as the artefacts related to the pinhole aperture and the low signal to noise ratio.

We show that the measurements required for the MI reconstruction of all parallel beam profiles for a given angle are independent to the measurements required to obtain the MI along parallel lines for another angle. As a result, the technique provides part of the beam coherence picture earlier than conventional PST as it does not require to process all projections to obtain it.

We demonstrate the experimental feasibility of the method in three experiments involving coherent light and partially coherent light generated by illuminating a computer-generated hologram (CGH) using a Gaussian Schell-model beam (GSMB) and by incoherently summing orthogonal modes. In addition, we provide two optical systems; one for the generation of the beams used in the experiments, and the other to acquire the required WD projections. The proposed technique provides valuable advantages respect to conventional PST, namely a speed boost for acquiring and processing the input data into the beam coherence state, and an early analysis of information since the part of the coherence state is recovered before all projections are processed.

We close the dissertation with an algorithm that incorporates all four techniques and determines which method is optimal for characterizing an unknown beam according to its symmetries.

1.1 Optical Beams

In this book we consider quasi-monochromatic scalar optical beams, i.e. linearly polarised light waves that are highly directional and whose spectral width is negligible compared to the beam mean frequency. Within this context, and without loss of generality, we assume that the beam is propagating along the z axis of a Cartesian coordinate system and omit the terms indicating temporal dependence. As a result, the beam is described at a plane transverse to its propagation direction by a scalar complex-valued function called *complex amplitude*, $f(\mathbf{r})$, where $\mathbf{r} = (x, y)$ is a vector in the transverse plane. Since light is commonly generated by random processes like the stimulated or spontaneous emission from excited atoms, optical beams have to be statistically treated. The beam amplitude, f, becomes a particular realisation of the statistical ensemble, $\{f(\mathbf{r})\}$. Since in most cases light is formed by a massive amount of independent contributions, we consider that the random process describing light follows Gaussian statistics. This implies that the second-order statistics of the beam are sufficient for a complete characterization. In particular, the MI defined as the following two-point correlation function

$$\Gamma(\mathbf{r}_1, \mathbf{r}_2) = \langle f(\mathbf{r}_1) f^*(\mathbf{r}_2) \rangle, \tag{1.1}$$

where $\langle \cdot \rangle$ stands for ensemble average and * for complex conjugated, contains all the information of the considered beams. In addition, our light model assumes ergodicity, which means that the ensemble average is equivalent to a time average.

All the spatial information of an optical beam is included in its MI. For instance, the intensity distribution is obtained as

$$I(\mathbf{r}) = \Gamma(\mathbf{r}, \mathbf{r}), \tag{1.2}$$

and the relative phase between the beam at the pair of points $\mathbf{r}_1$ and $\mathbf{r}_2$ as $\arg \Gamma(\mathbf{r}_1, \mathbf{r}_2)$, where arg is the argument of a complex number. In addition, the correlation between the light field at two points, known as complex coherence factor [Goo00] or equal-time complex degree of coherence, which for the sake of simplicity we further denote as *degree of coherence*, is obtained from the MI as:

$$\gamma(\mathbf{r}_1, \mathbf{r}_2) = \frac{\Gamma(\mathbf{r}_1, \mathbf{r}_2)}{\sqrt{I(\mathbf{r}_1) I(\mathbf{r}_2)}}. \tag{1.3}$$

The degree of coherence is a measure of the spatial coherence of the beam. A value of $|\gamma(\mathbf{r}_1, \mathbf{r}_2)| = 1$ indicates full coherence between the beam at points $\mathbf{r}_1$ and $\mathbf{r}_2$; a value of $|\gamma| = 0$ indicates complete incoherence; the rest of cases, $0 < |\gamma| < 1$, indicate partial coherence. In the particular situation of completely coherent light, the ensemble average is not required and the beam is perfectly described by its complex amplitude, $f(\mathbf{r})$. Spatial coherence is broadly regarded as the ability of the light

field coming from two points to interfere, thus its characterization is important for determining the outcome of experiments involving partially coherent light.

Partial coherent beams can be expressed as the incoherent sum of orthogonal coherent beams, usually referred as modes. This result is known as modal expansion [Man95]. The MI of any partially coherent beam can be expanded as

$$\Gamma\left(\mathbf{r}_1, \mathbf{r}_2\right) = \sum_n a_n \Psi_n\left(\mathbf{r}_1\right) \Psi_n^*\left(\mathbf{r}_2\right), \tag{1.4}$$

being a_n and Ψ_n the real coefficients and modes of the expansion, respectively, where n is the set element identifier which may consist in more than one label. From now on, sums without limits will span each summation label from 0 to ∞ unless otherwise stated. The local coherence properties of this kind of beams can significantly change between different pairs of points. Hence, the beam is often described by a global coherence parameter known as level of coherence or purity of a field [Alo11], which is defined as

$$\mu = \frac{\left(\sum_n a_n^2\right)^{1/2}}{\sum_n a_n}. \tag{1.5}$$

Recurrent examples of orthogonal sets are the HG and Laguerre-Gaussian (LG) beams because they are the natural modes emitted by lasers. In particular, HG beams are the resonating modes of laser cavities with rectangular symmetry. Their complex field amplitude is real and depends on two indices, m and n, via

$$\mathscr{H}_{m,n}\left(\mathbf{r}\right) = \sqrt{2}\frac{H_m\left(\sqrt{2\pi}\frac{x}{w}\right) H_n\left(\sqrt{2\pi}\frac{y}{w}\right)}{w\sqrt{2^m m!}\sqrt{2^n n!}} \exp\left(-\pi\frac{r^2}{w^2}\right), \tag{1.6}$$

where $r^2 = x^2 + y^2$, H_m is the Hermite polynomial of order m and w defines the beam waist. The intensity and phase of the $\mathscr{H}_{3,2}$ beam with $w = 0.73$ mm is presented in Fig. 1.1a. An interesting property of these modes is that they are separable in Cartesian coordinates. In other words, there are two functions $\mathscr{H}_m\left(x\right)$ and $\mathscr{H}_n\left(y\right)$ such that $\mathscr{H}_{m,n}\left(\mathbf{r}\right) = \mathscr{H}_m\left(x\right)\mathscr{H}_n\left(y\right)$.

On the other hand, LG beams are the resonating modes of laser cavities with cylindrical symmetry. Their complex field amplitude also depends on two indices, the radial p and the azimuthal l, and is given by

$$\begin{aligned}\mathscr{L}_p^l\left(\mathbf{r}\right) = w^{-1}\sqrt{\frac{p!}{\left(|l|-p\right)!}}\left\{\sqrt{2\pi}\left[\frac{x}{w} + \mathrm{isgn}\left(l\right)\frac{y}{w}\right]\right\}^{|l|} \\ \times L_p^{|l|}\left(2\pi\frac{r^2}{w^2}\right)\exp\left(-\pi\frac{r^2}{w^2}\right),\end{aligned} \tag{1.7}$$

where i is the imaginary unit, sgn is the sign function, L_p^l is the general Laguerre polynomial of indices p and l [Pou00], and, similarly to HG modes, w defines the

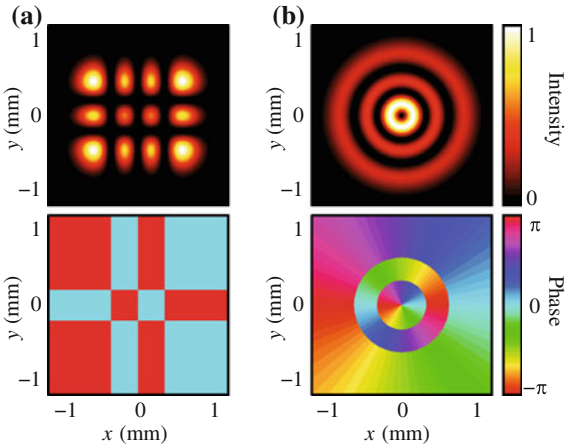

Fig. 1.1 Intensity and phase distribution of two example beams: **a** Hermite-Gaussian $\mathscr{H}_{3,2}$ and **b** Laguerre-Gaussian $\mathscr{L}_2^1$. In both cases $w = 0.73$ mm

beam waist. The beam intensity distribution presents $p + 1$ rings. On the other side, the azimuthal index determines the topological charge of the beam, i.e. the number of 2π-*jumps* experienced by its vortex phase distribution. The intensity and phase distributions of the $\mathscr{L}_2^1$ beam with $w = 0.73$ mm is presented in Fig. 1.1b. While HG beams are separable in Cartesian coordinates, LG beams are separable in cylindrical coordinates and have rotationally symmetric intensity distribution.

Both sets of modes can be used for the expansion of the widely-used class of partially coherent beams known as twisted Gaussian Schell-model beams (TGSMBs) [Sim93, Bas00], whose MI is defined as

$$\Gamma(\mathbf{r}_1, \mathbf{r}_2) = \exp\left[-\pi \frac{\mathbf{r}_1^2 + \mathbf{r}_2^2}{w^2} - 2\pi \frac{(\mathbf{r}_1 - \mathbf{r}_2)^2}{\sigma_c^2} - \mathrm{i}2\pi\tau\,(\mathbf{r}_1 - \mathbf{r}_2)\,\mathbf{J}\,(\mathbf{r}_1 + \mathbf{r}_2)\right]. \tag{1.8}$$

The first term in the exponential, the one associated with the product $\mathbf{r}_1^2 + \mathbf{r}_2^2$, defines the beam intensity profile, being w its Gaussian width. The second term, associated with $(\mathbf{r}_1 - \mathbf{r}_2)^2$, is related to the modulus of the degree of coherence, being σ_c its Gaussian width. The final term defines its twisted phase, which is related to the orbital angular momentum carried by the beam, being τ the *twist* factor and

$$\mathbf{J} = \begin{bmatrix} 0 & 1 \\ -1 & 0 \end{bmatrix}. \tag{1.9}$$

While in certain situations the LG modes are used for the expansion of TGSMBs according to Eq. (1.4), GSMBs, which are obtained for the particular case $\tau = 0$, can always be expanded in HG modes [Sun95].

In addition, since both HG and LG beams form an orthonormal basis for 2D square-integrable functions, they are suitable for the expansion of the beam complex amplitudes:

$$f(\mathbf{r}) = \sum_{m,n} b_{m,n} \mathscr{H}_{m,n}(\mathbf{r}) = \sum_{p,l} b_p^l \mathscr{L}_p^l(\mathbf{r}), \tag{1.10}$$

where $b_{m,n}$ and b_p^l can take complex values. Notice that the expansion coefficients are random variables in the case of partially coherent beams since the complex amplitude is stochastic. In such situation the beam is best described by its expanded MI:

$$\Gamma(\mathbf{r}_1, \mathbf{r}_2) = \sum_{m,n} \sum_{m',n'} \left\langle b_{m,n} b_{m',n'}^* \right\rangle \mathscr{H}_{m,n}(\mathbf{r}_1) \mathscr{H}_{m',n'}(\mathbf{r}_2) = \sum_{p,l} \sum_{p',l'} \left\langle b_p^l \left(b_{p'}^{l'}\right)^* \right\rangle \mathscr{L}_p^l(\mathbf{r}_1) \left[\mathscr{L}_{p'}^{l'}(\mathbf{r}_2)\right]^*. \tag{1.11}$$

As we will see in the experiments of the next Chapters, both types of beam modal decomposition, see Eqs. (1.4) and (1.11), present a simple scheme for generating coherent and partially coherent beams with complex spatial structure.

The characterization of an a priori unknown beam by the experimental retrieval of its MI, either via direct reconstruction or by the determination of its expansion coefficients, is a considerable challenge. In the last decades, significant effort has been made to find alternative functions to describe an optical beam which are easier to determine experimentally. In particular, the WD and the AF are the most promising alternatives to the MI so far.

The WD was introduced in 1932 by E. Wigner as an auxiliary function to aid in the estimation of the physical quantities of quantum systems in thermodynamic equilibrium [Wig32]. The same concept was latter imported to optics to analyze the statistical behaviour of optical beams and systems [Wal68, Bas78]. The WD is defined as the Fourier transform (FT) of the MI via

$$W(\mathbf{r}, \mathbf{p}) = \frac{1}{\sigma^2} \int \mathrm{d}\mathbf{r}' \, \Gamma\left(\mathbf{r} + \frac{\mathbf{r}'}{2}, \mathbf{r} - \frac{\mathbf{r}'}{2}\right) \exp\left(-\frac{\mathrm{i}2\pi}{\sigma^2} \mathbf{p} \cdot \mathbf{r}'\right), \tag{1.12}$$

where $\mathbf{p} = (u, v) = \sigma^2 \mathbf{k}_\perp$ is a vector proportional to the transverse projection of the spatial frequency vector, $\mathbf{k}_\perp$, and σ is a convenient constant with units of length that is commonly used in Fourier optics. The WD physically represents the quasi-distribution of the beam power in the four-dimensional phase space defined by vectors $\mathbf{r}$ and $\mathbf{p}$. Although the WD cannot be treated as a formal distribution because it can take negative values, posses many important properties useful for beam analysis. In particular, the marginal distributions,

$$I(\mathbf{r}) = \frac{1}{\sigma^2} \int \mathrm{d}\mathbf{p} \, W(\mathbf{r}, \mathbf{p}), \tag{1.13}$$

$$\widetilde{I}(\mathbf{p}) = \frac{1}{\sigma^2} \int \mathrm{d}\mathbf{r} \, W(\mathbf{r}, \mathbf{p}), \tag{1.14}$$

represent the intensity and power spectra of the beam, respectively, which are formal distributions of the beam power in space and spatial frequency. Furthermore, the expected value for the quantity $x^m y^n u^{m'} v^{n'}$ using the WD as distribution function is regarded as the *WD moment*, $\mu_{m,n,m',n'}$ of order $m+n+m'+n'$ [Ser91, Bas91]. The WD moments provide a global characterization of the beam. For example, the zero-order moment represents the beam total power in the transverse plane, while the four first-order moments represent the beam centroid in phase space. There are ten second-order moments which define the spatial width and angular spread of the beam, among other less intuitive characteristics such as the beam curvature or its quality parameters [Ana94, Epp98]. While twisted Gaussian Schell-model, HG, and LG beams are completely defined by its zero-, first-, and second-order WD moments, a general beam requires all its moments to be unequivocally defined.

Alternatively, the AF can be used for beam description. Originally, it was applied for object detection using radar systems [Woo53]. In 1974 it was introduced in Fourier optics to analyze the propagation of coherent beams in certain isotropic systems [Pap74]. Its utility for characterizing partially coherent beams was soon appreciated [Gui78]. Similarly to the WD, the AF is also defined as a FT of the MI:

$$A(\mathbf{r},\mathbf{p}) = \frac{1}{\sigma^2}\int \mathrm{d}\mathbf{r}'\,\Gamma\left(\mathbf{r}'+\frac{1}{2}\mathbf{r},\mathbf{r}'-\frac{1}{2}\mathbf{r}\right)\exp\left(-\frac{\mathrm{i}2\pi}{\sigma^2}\mathbf{r}'\cdot\mathbf{p}\right). \tag{1.15}$$

The AF is also obtained from the WD by a double FT:

$$A(\mathbf{r},\mathbf{p}) = \frac{1}{\sigma^4}\int \mathrm{d}\mathbf{r}'\mathrm{d}\mathbf{p}'\,W\left(\mathbf{r}',\mathbf{p}'\right)\exp\left[-\frac{\mathrm{i}2\pi}{\sigma^2}\left(\mathbf{r}\cdot\mathbf{p}'-\mathbf{p}\cdot\mathbf{r}'\right)\right]. \tag{1.16}$$

Since the MI is invertible from both the AF and the WD,

$$\Gamma(\mathbf{r}_1,\mathbf{r}_2) = \frac{1}{\sigma^2}\int \mathrm{d}\mathbf{p}\,W\left[\frac{1}{2}(\mathbf{r}_1+\mathbf{r}_2),\mathbf{p}\right]\exp\left[\frac{\mathrm{i}2\pi}{\sigma^2}\mathbf{p}\cdot(\mathbf{r}_1-\mathbf{r}_2)\right] \tag{1.17}$$

$$= \frac{1}{\sigma^2}\int \mathrm{d}\mathbf{p}\,A(\mathbf{r}_1-\mathbf{r}_2,\mathbf{p})\exp\left[\frac{\mathrm{i}\pi}{\sigma^2}\mathbf{p}\cdot(\mathbf{r}_1+\mathbf{r}_2)\right], \tag{1.18}$$

the three functions are related by a FT as illustrated in Fig. 1.2. Similarly to the modal expansion of the MI, see Eq. (1.4), the WD and AF can be represented as a linear superposition of WDs, W_{Ψ_n} and AFs, A_{Ψ_n} of expansion modes:

$$W(\mathbf{r},\mathbf{p}) = \sum_n a_n W_{\Psi_n}(\mathbf{r},\mathbf{p}), \tag{1.19}$$

$$A(\mathbf{r},\mathbf{p}) = \sum_n a_n A_{\Psi_n}(\mathbf{r},\mathbf{p}). \tag{1.20}$$

Although equivalent descriptions of a beam, each one presents the information differently. While the coherence information is readily available from the MI, the WD and the AF are more convenient for analyzing the beam propagation through optical systems.

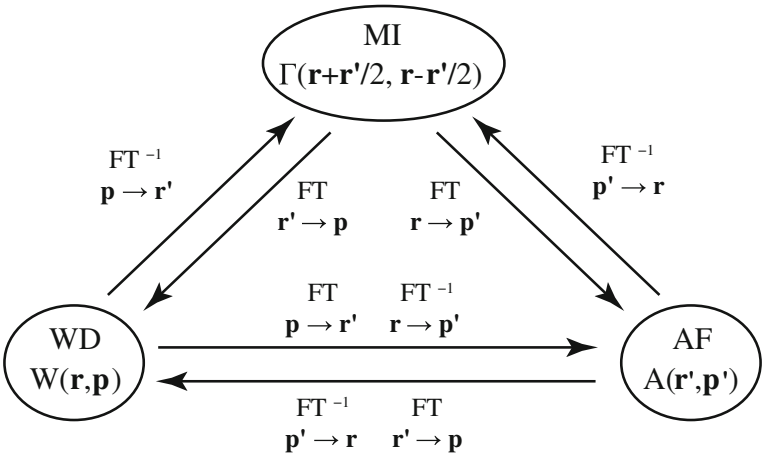

Fig. 1.2 Illustration of the relation between the MI, the WD, and the AF. All three beam descriptors are related by a FT of their coordinates

The WD is also interesting for analyzing the degree of coherence of a beams. For example consider four 1D lGSMBs [$\tau = 0$ and $y = 0$ in Eq. (1.8)] with the same intensity width, w, and different coherence widths, w_c. In spite of having the same intensity distribution, their coherent properties are distinct. This difference is readily observable as a broadening in the WD along the **p** axes, as it is displayed in Fig. 1.3, where the WD of 1D GSMBs with $w = 0.71$ mm and $w_c = 5.68, 2.84, 1.42,$

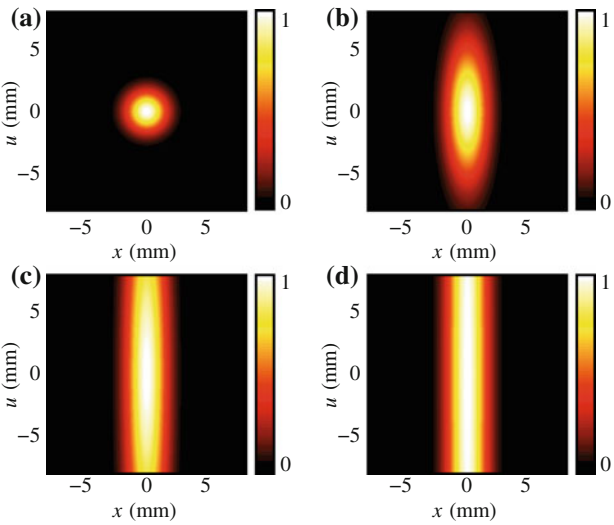

Fig. 1.3 WDs of 1D GSMBs with the same intensity width, $w = 1.8$ mm, and different coherence widths, **a** $w_c = 5.68$ mm, **b** $w_c = 2.84$ mm, **c** $w_c = 1.42$ mm, and **d** $w_c = 0.71$ mm. Notice how the WD broadens in the frequency axis as the width of the coherence degree decreases

and 0.71 mm are presented. In this particular case, the AF coincides with the WD. Nevertheless, in a general situation the AF is complex-valued which makes difficult the coherence analysis.

An important advantage of using the WD and AF instead of the MI to describe an optical beam is that both functions are more easily reconstructed from experimental measurements. In particular, the phase-space tomography method for WD [Ray94] and AF [Tu97] reconstruction, which will be introduced in Sect. 1.6, presents a convenient framework for beam characterization.

1.2 Beam Propagation

In order to characterize an optical beam, optical systems have to be used. If we are only interested in the intensity distribution all the information can be obtained using a camera. For a complete beam characterization, however, a more sophisticated optical setup could be necessary. In the case of the non-interferometric methods considered in this dissertation, the systems involve lenses and free-space propagations. In any case, these systems transform the (stochastic) complex amplitude of beams and, hence, its MI, WD, and AF. For a complete understanding of how the characterization methods work, we must focus on the transformations performed by optical systems.

Since we are mainly interested in thin lenses and free-space propagations we will introduce the *lossless first-order optical systems*. A lossless first-order optical systems (LFOS) is described by a 4×4 symplectic matrix, $\mathbf{T}$, referred to as ray-transformation matrix or simply ABCD matrix [Bas78, Naz82]. In terms of ray optics, $\mathbf{T}$ relates the initial position, $\mathbf{r}_\mathrm{i}$, and direction, proportional to $\mathbf{p}_\mathrm{i}$, of a light ray with the corresponding vectors in the output plane of the optical system ($\mathbf{r}_\mathrm{o}$, $\mathbf{p}_\mathrm{o}$) via

$$\begin{bmatrix} \mathbf{r}_\mathrm{o} \\ \mathbf{p}_\mathrm{o} \end{bmatrix} = \mathbf{T} \begin{bmatrix} \mathbf{r}_\mathrm{i} \\ \mathbf{p}_\mathrm{i} \end{bmatrix} = \begin{bmatrix} \mathbf{A} & \mathbf{B} \\ \mathbf{C} & \mathbf{D} \end{bmatrix} \begin{bmatrix} \mathbf{r}_\mathrm{i} \\ \mathbf{p}_\mathrm{i} \end{bmatrix}, \tag{1.21}$$

where $\mathbf{A}$, $\mathbf{B}$, $\mathbf{C}$, and $\mathbf{D}$ are 2×2 dimensionless matrices. The symplectic condition is a constrain in $\mathbf{T}$ that can be formulated in terms of the $\mathbf{J}$ matrix, see Eq. (1.9), as [Bas06]

$$\mathbf{T}^{-1} = -\mathbf{J}\mathbf{T}^T\mathbf{J} = \begin{bmatrix} \mathbf{D}^T & -\mathbf{B}^T \\ -\mathbf{C}^T & \mathbf{A}^T \end{bmatrix}, \tag{1.22}$$

being $\mathbf{0}$ and $\mathbf{I}$ are the zero and identity 2×2 matrices and the superscript ^{T} the transposition operation.

While the evolution of the beam can be modelled in terms of rays using the ABCD matrix, the evolution of the beam amplitude when it propagates through a LFOS is described by a linear canonical transform (LCT). The LCT relates the input complex field amplitude, $f(\mathbf{r}_\mathrm{i})$, with its output $f_\mathbf{T}(\mathbf{r}_\mathrm{o})$, via the integral

$$f_{\mathbf{T}}(\mathbf{r}_{\mathrm{o}}) = \frac{1}{\sigma^2}\int \mathrm{d}\mathbf{r}_{\mathrm{i}}\; f_{\mathrm{i}}(\mathbf{r}_{\mathrm{i}})\, K_{\mathbf{T}}(\mathbf{r}_{\mathrm{i}}, \mathbf{r}_{\mathrm{o}})\,, \tag{1.23}$$

where $K_{\mathbf{T}}$ is the transformation kernel corresponding to the LFOS. Except in the case in which the LFOS is described by a singular non-zero $\mathbf{B}$ matrix, $\mathbf{B} \neq \mathbf{0}$ and $\det \mathbf{B} = 0$ [Ali05], the kernel can be written in terms of $\mathbf{T}$ as,

$$K_{\mathbf{T}} = \begin{cases} \frac{1}{\sqrt{\det \mathrm{i}\mathbf{B}}} \exp\left[\frac{\mathrm{i}\pi}{\sigma^2}\left(\mathbf{r}_{\mathrm{i}}^T\mathbf{B}^{-1}\mathbf{A}\mathbf{r}_{\mathrm{i}} - 2\mathbf{r}_{\mathrm{i}}^T\mathbf{B}^{-1}\mathbf{r}_{\mathrm{o}} + \mathbf{r}_{\mathrm{o}}^T\mathbf{D}\mathbf{B}^{-1}\mathbf{r}_{\mathrm{o}}\right)\right] & [\mathbf{B} \neq \mathbf{0}]\,, \\ \frac{\sigma^2}{\sqrt{|\det \mathbf{A}|}} \exp\left(\frac{\mathrm{i}\pi}{\sigma^2}\mathbf{r}_{\mathrm{o}}^T\mathbf{C}\mathbf{A}^{-1}\mathbf{r}_{\mathrm{o}}\right)\delta\left(\mathbf{r}_{\mathrm{i}} - \mathbf{A}^{-1}\mathbf{r}_{\mathrm{o}}\right) & [\mathbf{B} = \mathbf{0}]\,. \end{cases} \tag{1.24}$$

Equivalently, the MI is transformed via

$$\Gamma_{\mathbf{T}}(\mathbf{r}_{1\mathrm{o}}, \mathbf{r}_{2\mathrm{o}}) = \frac{1}{\sigma^4}\int \mathrm{d}\mathbf{r}_{1\mathrm{i}}\mathrm{d}\mathbf{r}_{2\mathrm{i}}\; \Gamma(\mathbf{r}_{1\mathrm{i}}, \mathbf{r}_{2\mathrm{i}})\, K_{\mathbf{T}}(\mathbf{r}_{1\mathrm{i}}, \mathbf{r}_{1\mathrm{o}})\, K_{\mathbf{T}}^{*}(\mathbf{r}_{2\mathrm{i}}, \mathbf{r}_{2\mathrm{o}})\,. \tag{1.25}$$

It is complicated to numerically calculate this transformation due to the high dimensionality of the integral, which demonstrates the difficulty of describing partially coherent beams via their MIs.

On the contrary, the effect of the beam propagation through a LFOS is simply an affine change of coordinates in the beam WD and AF. Actually, the affine transformation is the same for both functions, see [Alo11] and references therein:

$$W(\mathbf{r}, \mathbf{p}) = W_{\mathbf{T}}(\mathbf{A}\mathbf{r} + \mathbf{B}\mathbf{p}, \mathbf{C}\mathbf{r} + \mathbf{D}\mathbf{p})\,, \tag{1.26}$$

$$A(\mathbf{r}, \mathbf{p}) = A_{\mathbf{T}}(\mathbf{A}\mathbf{r} + \mathbf{B}\mathbf{p}, \mathbf{C}\mathbf{r} + \mathbf{D}\mathbf{p})\,, \tag{1.27}$$

or correspondingly,

$$W_{\mathbf{T}}(\mathbf{r}, \mathbf{p}) = W\left(\mathbf{D}^T\mathbf{r} - \mathbf{B}^T\mathbf{p}, -\mathbf{C}^T\mathbf{r} + \mathbf{A}^T\mathbf{p}\right), \tag{1.28}$$

$$A_{\mathbf{T}}(\mathbf{r}, \mathbf{p}) = A\left(\mathbf{D}^T\mathbf{r} - \mathbf{B}^T\mathbf{p}, -\mathbf{C}^T\mathbf{r} + \mathbf{A}^T\mathbf{p}\right). \tag{1.29}$$

The simple transformation law for WD and AF plays the key role in beam characterization.

Examples of LFOS, where a beam with wavelength λ propagates through, include:

- The free-space propagation, associated with

$$\mathbf{F}_z = \begin{bmatrix} \mathbf{I} & \frac{z}{\lambda}\mathbf{I} \\ \mathbf{0} & \mathbf{I} \end{bmatrix}, \tag{1.30}$$

  and $\sigma = \lambda$, where z is the propagation distance.

- The thin lens operation, associated with

$$\mathbf{L}_{\mathrm{f}} = \begin{bmatrix} \mathbf{I} & \mathbf{0} \\ -\lambda\mathbf{G} & \mathbf{I} \end{bmatrix}, \tag{1.31}$$

  where $\mathbf{G}$ is the generalized lens-power matrix. In particular, a convergent spherical lens of focal length f corresponds to $\mathbf{G} = (1/\mathrm{f})\mathbf{I}$ with $\sigma = \lambda$.
- The FT, associated with

$$\mathbf{T} = \begin{bmatrix} \mathbf{0} & \mathbf{I} \\ -\mathbf{I} & \mathbf{0} \end{bmatrix}. \tag{1.32}$$

  In this case σ depends on the particular implementation of the Fourier transformer. For instance, the Fourier system formed by two free-space propagation intervals of distance f separated by a convergent spherical lens of focal f, is associated with the parameter $\sigma = \sqrt{\lambda \mathrm{f}}$.
- The rotation in the phase space, which corresponds to all ray transformation matrices satisfying $\mathbf{A} = \mathbf{D} = \mathbf{X}$ and $\mathbf{B} = -\mathbf{C} = \mathbf{Y}$, i.e.

$$\mathbf{T}_{\mathrm{U}} = \begin{bmatrix} \mathbf{X} & \mathbf{Y} \\ -\mathbf{Y} & \mathbf{X} \end{bmatrix}, \tag{1.33}$$

  where $\mathbf{U} = \mathbf{X} + \mathrm{i}\mathbf{Y}$ is often defined for simplified rotation matrix description. This transformation includes the particular cases of *Rotator*, *Gyrator*, and FRFT [Oza93, Sim00b, Ali08, Rod07b], which are summarized in the following Section.

The LFOSs provide a set of valuable tools for WD and AF manipulation. In particular, they allow easily rotating the beam WD and AF in phase-space. By analogy with conventional tomography, this inspired the phase-space tomography method. In order to establish it we first focus on the mathematical formalism of phase-space rotations.

1.3 Rotations in Phase Space

There are three basic rotations in phase space—rotator, gyrator, and FRFT [Sim00b, Ali08]. Each one performs a different kind of rotation which is associated with the LFOSs described by $\mathbf{T}_R^{\alpha}$, $\mathbf{T}_G^{\beta}$, and $\mathbf{T}_F^{\gamma_x,\gamma_y}$, respectively. For both the sake of compactness and simplicity, instead of defining these LFOSs by its ray transformation matrices, $\mathbf{T}_{R,G,F}$, we will recur to the unitary matrices $\mathbf{U}_{R,G,F}$ where

$$\mathbf{T}_{R,G,F} = \begin{bmatrix} \mathbf{X}_{R,G,F} & \mathbf{Y}_{R,G,F} \\ -\mathbf{Y}_{R,G,F} & \mathbf{X}_{R,G,F} \end{bmatrix}, \qquad \mathbf{U}_{R,G,F} = \mathbf{X}_{R,G,F} + \mathrm{i}\mathbf{Y}_{R,G,F}. \tag{1.34}$$

The concatenation of these rotations produce another system with unitary matrix resulting from the product of the corresponding unitary matrices:

$$\mathbf{T} = \mathbf{T}_2\mathbf{T}_1 \quad \Rightarrow \quad \mathbf{U} = \mathbf{U}_2\mathbf{U}_1. \tag{1.35}$$

Rotator is the rotation associated with the xy and uv planes. It depends on a single parameter that corresponds to the rotation angle in both planes of phase space. The corresponding unitary matrix is

$$\mathbf{U}_R^{\alpha} = \begin{bmatrix} \cos\alpha & \sin\alpha \\ -\sin\alpha & \cos\alpha \end{bmatrix}. \tag{1.36}$$

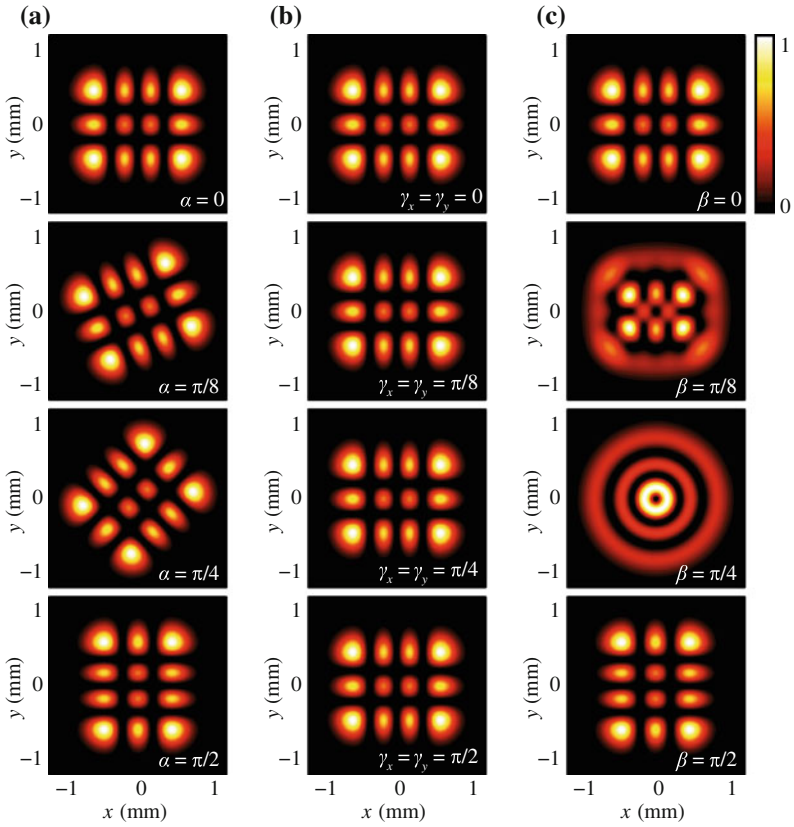

Fig. 1.4 Evolution of the intensity of the $\mathscr{H}_{3,2}(\mathbf{r})$ mode with $w = 0.73$ mm when the beam propagates through different phase-space rotation lfos. **a** Rotator for angles $\alpha = 0, \pi/8, \pi/4$, and $\pi/2$. **b** Symmetric FRFT for angles $\gamma_x = \gamma_y = 0, \pi/8, \pi/4$, and $\pi/2$. **c** Gyrator for angles $\beta = 0, \pi/8, \pi/4$, and $\pi/2$

The intensity after the propagation through a Rotator LFOS for angle $\alpha = 0, \pi/8,$ $\pi/4$, and $\pi/2$ of the HG mode $\mathscr{H}_{3,2}$ with $w = 0.73$ mm is presented in Fig. 1.4a. The same result for a rectangular signal is presented in Fig. 1.5a.

FRFT denotes the two independent rotations in the planes xu and yv described by the unitary matrix

$$\mathbf{U}_F^{\gamma_x,\gamma_y} = \begin{bmatrix} \exp(\mathrm{i}\gamma_x) & 0 \\ 0 & \exp(\mathrm{i}\gamma_y) \end{bmatrix}. \tag{1.37}$$

As in the rotator case, the intensity evolution of the $\mathscr{H}_{3,2}$ mode and the rectangular signal for angles $\gamma_x = \gamma_y = 0, \pi/8, \pi/4$, and $\pi/2$ is presented in Figs. 1.4b and 1.5b, respectively. Notice that the HG modes do not change its intensity when they propagate through systems performing the FRFT because they are eigenfunctions

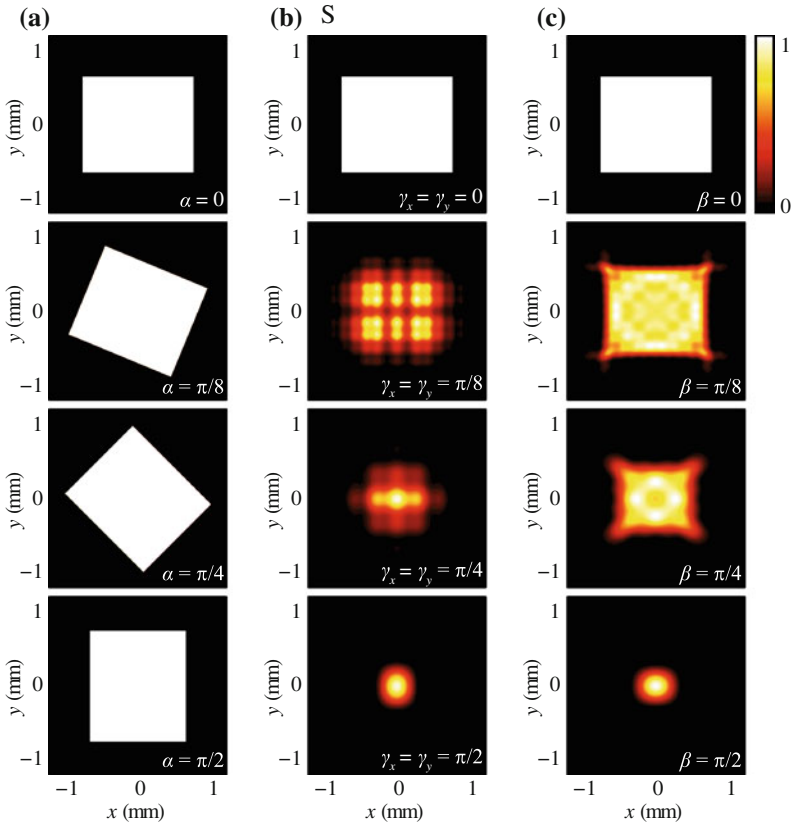

Fig. 1.5 Evolution of the intensity of a rectangular signal with 0.75 mm horizontal and 0.65 mm vertical sides when the beam propagates through different phase-space rotationlLFOSs. **a** Rotator for angles $\alpha = 0, \pi/8, \pi/4$, and $\pi/2$. **b** Symmetric FRFT for angles $\gamma_x = \gamma_y = 0, \pi/8, \pi/4$, and $\pi/2$. **c** Gyrator for angles $\beta = 0, \pi/8, \pi/4$, and $\pi/2$

of the transformation and its waists are equal to the FRFT scale parameter, $w = \sigma$. Also, the case $\gamma_x = \gamma_y = \pi/2$ corresponds to the FT.

Gyrator depends on a single parameter, β, which is associated with the rotation angle in the planes xv and yu and is described by the unitary matrix

$$\mathbf{U}_G^{\beta} = \begin{bmatrix} \cos\beta & \mathrm{i}\sin\beta \\ \mathrm{i}\sin\beta & \cos\beta \end{bmatrix}. \tag{1.38}$$

It is not an independent rotation from Rotator and FRFT since it can be written as

$$\mathbf{U}_G^{\beta} = \mathbf{U}_R^{-\pi/4}\mathbf{U}_F^{\beta,-\beta}\mathbf{U}_R^{\pi/4}. \tag{1.39}$$

As in the previous rotations, the intensity evolution of the $\mathscr{H}_{3,2}$ mode and the rectangular signal for angles $\beta = 0, \pi/8, \pi/4$, and $\pi/2$ is presented in Figs. 1.4c and 1.5c. Notice that this transformation provides the mode conversion between HG and LG beams [Rod07a].

While in a 2D space there is a single rotation angle, four independent parameters are required to define an arbitrary rotation in phase space. The most general rotation can be constructed as the following concatenation of transformations given by their ray-transformation matrices

$$\mathbf{T}_R^{\beta}\mathbf{T}_F^{\gamma_x,\gamma_y}\mathbf{T}_R^{\alpha}. \tag{1.40}$$

Equation (1.40) is fundamental for the definition the phase-space tomography method. In particular, the FRFT is the core transformation behind all the phase-space tomography techniques described in this dissertation. It is further discussed in the following Section.

1.4 Fractional Fourier Transform

There are many ways to define the FRFT [Nam80, Oza93, Men93, Oza01]. We have introduced it in the previous Section as the operation that rotates the functions, WD and AF, presenting the beam in phase space and in its FT conjugated space, correspondingly. Thus the FRFT rotates the WD for independent angles γ_x and γ_y in the planes xu and yv, which is associated to the unitary matrix $\mathbf{U}_F^{\gamma_x,\gamma_y}$ given by Eq. (1.37). Conversely, the kernel of the LCT associated with the FRFT has to be defined to study the evolution of the stochastic field amplitude of a beam propagating through a FRFT optical system. The kernel is separable in Cartesian coordinates

$$K_F^{\gamma_x,\gamma_y}(\mathbf{r}_\mathrm{i}, \mathbf{r}_\mathrm{o}) = K_F^{\gamma_x}(x_\mathrm{i}, x_\mathrm{o})\, K_F^{\gamma_y}(y_\mathrm{i}, y_\mathrm{o}), \tag{1.41}$$

and for $\gamma_q = m\pi$ with $m \in \mathbb{Z}$ it is proportional to a Dirac delta function,

$$K_F^{m\pi}(q_\mathrm{i}, q_\mathrm{o}) = \begin{cases} \delta(q_\mathrm{i} - q_\mathrm{o}), & m \text{ is even}, \\ \delta(q_\mathrm{i} + q_\mathrm{o}), & m \text{ is odd}, \end{cases} \tag{1.42}$$

being q a placeholder for x and y. On the other hand, for angles $\gamma_q \in (0, \pi)$ it corresponds to

$$K_F^{\gamma_q}(q_\mathrm{i}, q_\mathrm{o}) = \frac{\exp\left(\mathrm{i}\gamma_q/2\right)}{\sqrt{\mathrm{i}\sin\gamma_q}} \times \exp\left\{\frac{\mathrm{i}\pi}{\sigma^2 \sin\gamma_q}\left[\left(q_\mathrm{i}^2 + q_\mathrm{o}^2\right)\cos\gamma_q - 2q_\mathrm{i}q_\mathrm{o}\right]\right\}. \tag{1.43}$$

Notice that for the special case $\gamma_q = \pi/2$ the FRFT is reduced to the conventional Fourier transform. The stochastic complex amplitude and the MI are transformed by the FRFT kernel according to Eqs. (1.23) and (1.25). In order to simplify the notation, we introduce f^{γ_x,γ_y} and $\Gamma^{\gamma_x,\gamma_y}$ to refer to the complex amplitude and MI transformed by the FRFT for angles γ_x and γ_y.

The FRFT for the special case $\gamma_x = \gamma_y$ is referred to as *symmetric* FRFT. It corresponds to the propagation through isotropic and homogeneous media, except for a scale and quadratic phase factor, which includes the free-space propagation [Ali94, Oza01]. It also corresponds to the beam propagation through a quadratic radial gradient index (GRIN) fibre [Oza93]. Analogously, the special case $\gamma_x = -\gamma_y$ is referred to as *antisymmetric* FRFT. For its physical realisation, astigmatic optical elements, such as cylindrical lenses, are required. Notice that the scale parameter σ depends on the concrete optical implementation of the FRFT.

To simplify the enumeration of its properties, the FRFT can be thought of as an operator that transforms an input complex amplitude into the resulting output complex amplitude,

$$\mathfrak{F}^{\gamma_x,\gamma_y}\left[f(\mathbf{r}_\mathrm{i})\right](\mathbf{r}_\mathrm{o}) \equiv \mathfrak{F}^{\gamma_x,\gamma_y} f(\mathbf{r}_\mathrm{o}) \equiv F^{\gamma_x,\gamma_y}(\mathbf{r}_\mathrm{o}), \tag{1.44}$$

where $\mathfrak{F}^{\gamma_x,\gamma_y}$ represents the FRFT operator for angles $\gamma_{x,y}$. The FRFT satisfies the following properties [Oza01], some of which will be used further.

- Linearity:

$$\mathfrak{F}^{\gamma_x,\gamma_y}(a_1 f_1 + a_2 f_2)(\mathbf{r}) = a_1 \mathfrak{F}^{\gamma_x,\gamma_y} f_1(\mathbf{r}) + a_2 \mathfrak{F}^{\gamma_x,\gamma_y} f_2(\mathbf{r}). \tag{1.45}$$

- Inversion:

$$\left(\mathfrak{F}^{\gamma_x,\gamma_y}\right)^{-1} = \mathfrak{F}^{-\gamma_x,-\gamma_y}. \tag{1.46}$$

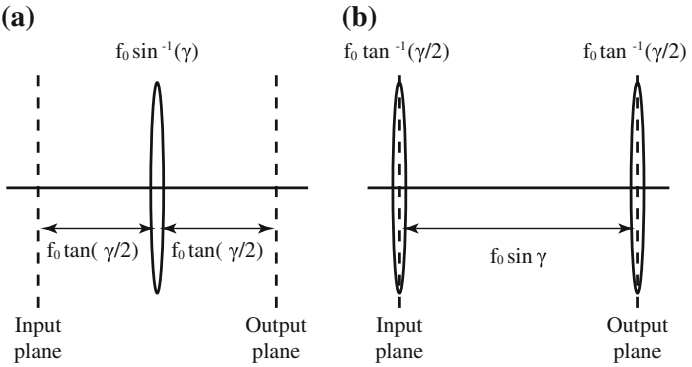

Fig. 1.6 Optical systems to perform the symmetric ($\gamma_x = \gamma_y = \gamma$) FRFT proposed in [Loh93]. **a** Type I system formed by two free-space propagation intervals and a spherical lens. **b** Type II system formed by two spherical lenses separated by a free-space propagation

- Index additivity:

$$\mathfrak{F}^{\gamma_x',\gamma_y'}\mathfrak{F}^{\gamma_x,\gamma_y} = \mathfrak{F}^{\gamma_x+\gamma_x',\gamma_y+\gamma_y'}. \tag{1.47}$$

- Associativity:

$$\mathfrak{F}^{\gamma_x'',\gamma_y''}\left(\mathfrak{F}^{\gamma_x',\gamma_y'}\mathfrak{F}^{\gamma_x,\gamma_y}\right) = \left(\mathfrak{F}^{\gamma_x'',\gamma_y''}\mathfrak{F}^{\gamma_x',\gamma_y'}\right)\mathfrak{F}^{\gamma_x,\gamma_y}. \tag{1.48}$$

- Commutativity:

$$\mathfrak{F}^{\gamma_x',\gamma_y'}\mathfrak{F}^{\gamma_x,\gamma_y} = \mathfrak{F}^{\gamma_x,\gamma_y}\mathfrak{F}^{\gamma_x',\gamma_y'}. \tag{1.49}$$

The FRFT can be implemented using a LFOS. In particular, A. Lohmann proposed two independent systems containing thin spherical lenses to perform the symmetric, $\gamma_x = \gamma_y = \gamma$, FRFT of a 2D beam [Loh93]. Their schemes are displayed in Fig. 1.6. The system of type I consists in two free-space intervals of the same distance, z, with a spherical lens of focal length f in between. The transformation angle γ depends on the distance for the free-space propagation, $z = \mathrm{f}_0 \tan(\gamma/2)$, and the focal length of the lens via: $\mathrm{f} = \mathrm{f}_0/\sin\gamma$. The system of type II consists in two spherical lenses of the same focal length, f′, separated by a free-space propagation of distance z'. As in the type I system, the lens and free-space propagation parameters are variable and depend on the FRFT angle, $\mathrm{f}' = \mathrm{f}_0/\tan(\gamma/2)$ and $z' = \mathrm{f}_0 \sin\gamma$. In both systems f_0 is a reference distance that determines the rest of parameters including the system length parameter $\sigma = \sqrt{\lambda \mathrm{f}_0}$. Using the ABCD matrices for the lens and free-space propagation introduced in Sect. 1.2, it is straightforward to check that both Lohmann systems perform the FRFT:

$$\begin{aligned}
&\begin{bmatrix} \mathbf{I} & \frac{z}{\mathrm{f}_0}\mathbf{I} \\ \mathbf{0} & \mathbf{I} \end{bmatrix} \begin{bmatrix} \mathbf{I} & \mathbf{0} \\ -\frac{\mathrm{f}_0}{\mathrm{f}}\mathbf{I} & \mathbf{I} \end{bmatrix} \begin{bmatrix} \mathbf{I} & \frac{z}{\mathrm{f}_0}\mathbf{I} \\ \mathbf{0} & \mathbf{I} \end{bmatrix} \\
&= \begin{bmatrix} \mathbf{I} & \mathbf{0} \\ -\frac{\mathrm{f}_0}{\mathrm{f}'}\mathbf{I} & \mathbf{I} \end{bmatrix} \begin{bmatrix} \mathbf{I} & \frac{z'}{\mathrm{f}_0}\mathbf{I} \\ \mathbf{0} & \mathbf{I} \end{bmatrix} \begin{bmatrix} \mathbf{I} & \mathbf{0} \\ -\frac{\mathrm{f}_0}{\mathrm{f}'}\mathbf{I} & \mathbf{I} \end{bmatrix} \\
&= \begin{bmatrix} \cos\gamma\mathbf{I} & \sin\gamma\mathbf{I} \\ -\sin\gamma\mathbf{I} & \cos\gamma\mathbf{I} \end{bmatrix}. \qquad (1.50)
\end{aligned}$$

In addition, the symmetric FRFT can also be performed by a GRIN media [Oza93]. Consider the GRIN fibre whose index of refraction is given in terms of the radial distance, $r = \sqrt{x^2 + y^2}$, by

$$n^2(r) = n_1^2 \left[1 - \left(\frac{n_2}{n_1} \right)^2 r^2 \right], \qquad (1.51)$$

where n_1 and n_2 are the central value of the refraction index and its gradient along the radial coordinate, respectively. Parallel rays entering the GRIN media are focused periodically at distances $L = j\pi n_1/(2n_2)$, where j is an integer. The propagation of a beam through this fibre for a distance z is equivalent to the propagation through a FRFT system of length parameter $\sigma = [\lambda/(n_1 n_2)]^{1/2}$ for angle $\gamma = \pi z/L$.

The evolution of the WD and AF of a beam that is propagating through a FRFT optical system is given by Eq. (1.29). It consists in the expected phase-space coordinate rotations:

$$\begin{aligned}
&W_{\mathbf{T}_F^{\gamma_x,\gamma_y}}(\mathbf{r},\mathbf{p}) \equiv W^{\gamma_x,\gamma_y}(\mathbf{r},\mathbf{p}) \\
&\quad = W\left(\begin{bmatrix} x\cos\gamma_x - u\sin\gamma_x \\ y\cos\gamma_y - v\sin\gamma_y \end{bmatrix}, \begin{bmatrix} x\sin\gamma_x + u\cos\gamma_x \\ y\sin\gamma_y + v\cos\gamma_y \end{bmatrix} \right). \qquad (1.52) \\
&A_{\mathbf{T}_F^{\gamma_x,\gamma_y}}(\mathbf{r},\mathbf{p}) \equiv A^{\gamma_x,\gamma_y}(\mathbf{r},\mathbf{p}) \\
&\quad = A\left(\begin{bmatrix} x\cos\gamma_x - u\sin\gamma_x \\ y\cos\gamma_y - v\sin\gamma_y \end{bmatrix}, \begin{bmatrix} x\sin\gamma_x + u\cos\gamma_x \\ y\sin\gamma_y + v\cos\gamma_y \end{bmatrix} \right). \qquad (1.53)
\end{aligned}$$

In the case of the WD, its projection along the $\mathbf{p}$ direction coincides with the intensity of the fractional Fourier transformed beam, i.e. its fractional power spectra,

$$S^{\gamma_x,\gamma_y}(\mathbf{r}) \equiv \Gamma^{\gamma_x,\gamma_y}(\mathbf{r},\mathbf{r}) = \frac{1}{\sigma^2}\int \mathrm{d}\mathbf{p}\, W^{\gamma_x,\gamma_y}(\mathbf{r},\mathbf{p}). \qquad (1.54)$$

From Parseval theorem [Oza01], it is evident than all the fractional power spectra of the same beam must have the equal power:

$$P = \int \mathrm{d}\mathbf{r}\, I(\mathbf{r}) = \int \mathrm{d}\mathbf{r}\, S^{\gamma_x,\gamma_y}(\mathbf{r}). \qquad (1.55)$$

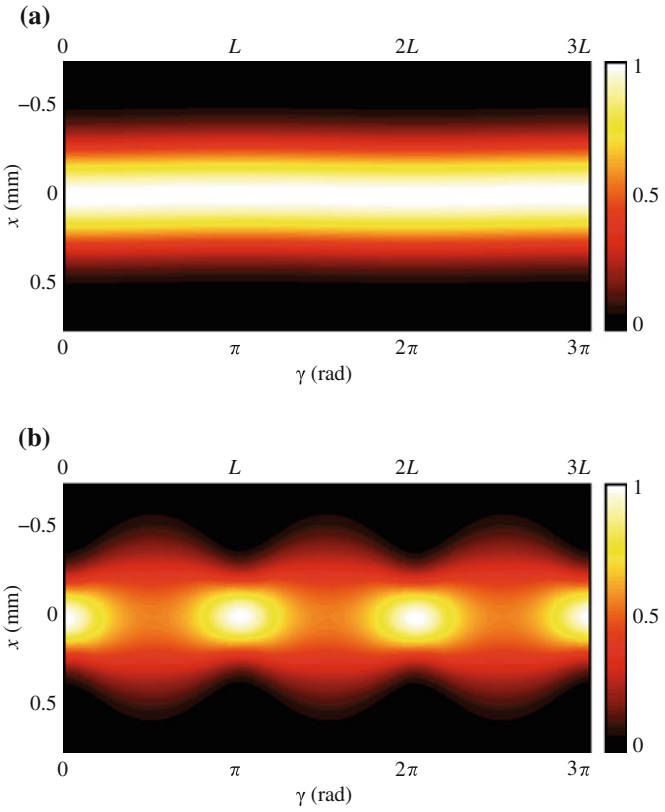

Fig. 1.7 RWT corresponding to the radial profile $y = 0$ of two fundamental Gaussian beams, $\mathscr{H}_{0,0}$, of $\lambda = 532\,\text{nm}$ with the beams waists **a** $w_1 = \sigma$ and **b** $w_2 = 3\sigma/4$ propagating in a GRIN fibre with $n_1 = 1.45$ and $n_2 = 7 \times 10^{-4}\,\text{mm}^{-1}$. The length parameter of the optical system is $\sigma = 0.73\,\text{mm}$

The equivalence of Eq. (1.54) is the starting point for the phase-space tomography method, which is suitable for the reconstruction of the WD of an arbitrary beam. The set of fractional power spectra for angles $\gamma_x \in \mathscr{A}_x$ and $\gamma_y \in \mathscr{A}_y$ is called the beam RWT [Woo94, Dea99] for the angular intervals $\mathscr{A}_x$ and $\mathscr{A}_y$, since it represents the Radon transform of the WD. Usually, both angular intervals are the same, $\mathscr{A}_x = \mathscr{A}_y = \mathscr{A}$. When in addition it spans a π-range interval, for example $\mathscr{A} = [\pi/2, 3\pi/2)$, we will refer to the RWT as the *full-range* RWT of the beam. As we will see in the following sections, from the full-range RWT, which is a measurable quantity, we can reconstruct the WD of the beam.

The full-range RWT of a beam contains all its relevant information. In particular, the RWT associated with the symmetric FRFT of a beam represents the evolution of its intensity at different propagation distances through a GRIN fibre [Oza93]. Additionally, the same RWT for the angular range $\mathscr{A} = [0, \pi/2]$ represents, except for a scale, the propagation of the beam in free-space for distance $z = \sigma^2/\lambda \tan\gamma$.

Consider, for example, the radial profile for $y = 0$ of two fundamental Gaussian beams, $\mathscr{H}_{0,0}(\mathbf{r})$, of different beam waists $w_1 = \sigma$ and $w_2 = 3\sigma/4$. Their RWTs are displayed in Fig. 1.7. Notice how the intensity of the Gaussian of waist w_1, associated with the fibre length parameter, is shape-invariant during its propagation through the fibre. Conversely, the intensity of the Gaussian beam of waist w_2, smaller than the length parameter, is rescaled during propagation. These examples remark the importance of the RWT as a tool for the analysis of beam propagation. In the following Sections we will see that since the WD of the beam can be recovered from a full-range RWT using a tomographic reconstruction algorithm, it provides a complete description of the beam, not only its propagation evolution.

1.5 Tomographic Reconstruction

Tomographic reconstruction is an ample term that usually refers to the technique that allows recovering a 2D object from its line integrals, or *projections*. It is based on the Radon transform and its inverse [Dea99], which relates the original object to its projections. Consider the object represented by the function $W(x, u)$. Its projections are the line integral of W along directions forming an angle θ with the u axis, i.e.

$$S^{\theta}(x) = \frac{1}{\sigma} \int \mathrm{d}u \; W(x\cos\theta + u\sin\theta, -x\sin\theta + u\cos\theta) \,. \tag{1.56}$$

The relation between the object and its projections is illustrated in Fig. 1.8 for two different angles, $\theta_1 = 25°$ and $\theta_2 = 65°$. According to the central slice theorem [Kak88], each projection corresponds to a "slice" of the 2D FT of the object:

$$\mathfrak{F}[W](\rho\cos\theta, \rho\sin\theta) = \widetilde{W}(\rho\cos\theta, \rho\sin\theta) = S^{\theta}(\rho) \,, \tag{1.57}$$

where $\widetilde{W}(x, y)$ represents the FT of the object. The original object can be reconstructed measuring a set of projections for angles θ covering a π-range interval, which is usually referred to as Radon map or *Radon transform* of the object. The function W can be obtained by assembling each projection into $\widetilde{W}$ and inverting the FT.

In practice, instead of assembling $\widetilde{W}$ and then inverting the FT, slices of the original object W are obtained directly from each projection. Consider the inverse FT relation between W and $\widetilde{W}$ in polar coordinates,

$$W(x, u) = \frac{1}{\sigma^2} \int_0^{\pi} \int \mathrm{d}\theta \mathrm{d}\rho \; |\rho| \, \widetilde{W}(\rho\cos\theta, \rho\sin\theta) \times \exp\left[-\frac{\mathrm{i}2\pi}{\sigma^2} \rho (x\cos\theta + u\sin\theta) \right], \tag{1.58}$$

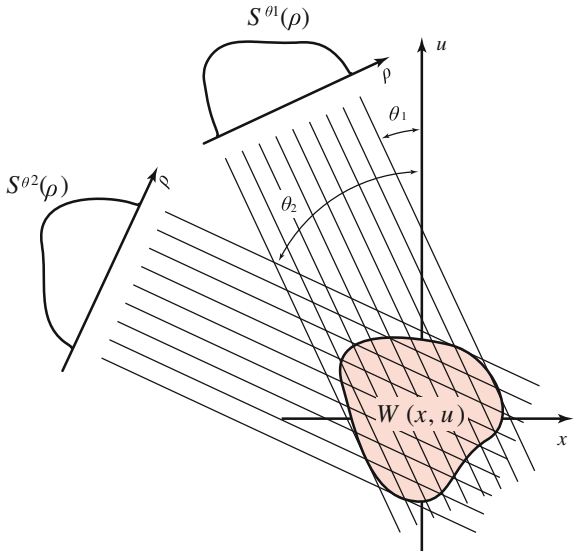

Fig. 1.8 Illustration of the line integrals that correspond to the projections for $\theta_1 = 25°$ and $\theta_2 = 65°$ of the object $W(x, u)$

where the properties $\cos(\theta + \pi) = -\cos\theta$ and $\sin(\theta + \pi) = -\sin\theta$ have been taken into account to reduce the angular integration interval from 2π to π. Identifying the FT of the object in polar coordinates with a projection, see Eq. (1.57), the following tomographic reconstruction formula is obtained:

$$W(x, u) = \frac{1}{\sigma^2} \int_0^{\pi} \int \mathrm{d}\theta \mathrm{d}\rho \ |\rho| \, S^{\theta}(\rho) \times \exp\left[-\frac{\mathrm{i}2\pi}{\sigma^2} \rho \left(x \cos\theta + u \sin\theta \right) \right]. \tag{1.59}$$

Equation (1.59) represents the *filtered back-projection* algorithm for tomographic reconstruction. The *filtered* part of its name comes from the fact that each projection is first filtered using a filter whose frequency response is $|\rho| / \sigma$:

$$\frac{1}{\sigma^2} \int \mathrm{d}\rho \ |\rho| \, S^{\theta}(\rho) \exp\left[-\frac{\mathrm{i}2\pi}{\sigma^2} \rho \left(x \cos\theta + u \sin\theta \right) \right]. \tag{1.60}$$

Although the ramp filter is the original one, different filters can be used for minimising the effects of the reconstruction artifacts. The *back-projection* part refers to the angular integral, which states that each filtered projection is then assembled, or *back-projected*, into the resulting object. The filtered back-projection algorithm with ramp filter will be extensively used throughout the dissertation due to its simplicity and readiness in most numerical simulation software.

In order to illustrate the tomographic reconstruction process consider the object represented in Fig. 1.9a. We can assemble its Radon transform measuring its projec-

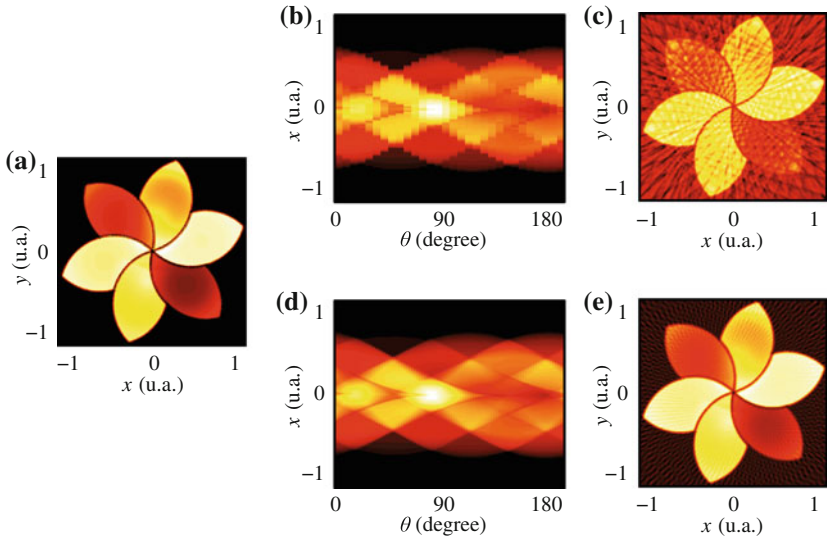

Fig. 1.9 Illustration of the tomographic reconstruction of an example object. **a** The original object is reconstructed from the Radon transform corresponding to **b** 30 and **d** 90 projections. Notice that the reconstructed object from **c** 30 projections has worst quality than the one reconstructed from **e** 90 projections

tions; for instance, Radon transforms for 30 and 90 equidistant projections are displayed in Fig. 1.9b, d. The reconstructed objects presented in Fig. 1.9c, e are obtained applying the filtered back-projection algorithm to their corresponding Radon transforms.

The crucial step in tomographic reconstruction is obtaining the projections of the object. In the case of soft X-ray tomographic reconstruction, these are obtained illuminating a 2D section of a 3D body and measuring the intensity once the object is traversed. The exponential absorption coefficient for different light paths produce a modulation in the measured intensity, which constitutes the projection. In other situations, as we will investigate next, the projections are obtained following more sophisticated ways.

1.6 Phase-Space Tomography

Phase-space tomography is a tomographic reconstruction technique specialized in reconstructing a 4D virtual object, the WD of a 2D beam. These two differences, the object being 4D and virtual, produce consequences that complicate its practical implementation.

On the first hand, while for 2D objects the most general rotation is unequivocally associated with a single angle, for an object embedded in phase space there are

four angles associated with the most general rotation, recall Eq. (1.40). This is not necessarily an inconvenience since it provides a richer selection of projections to choose from in order to recover the WD of the beam. The usual rotation scheme is associated with the FRFT for independent angles, which is interesting because it grants the most similar reconstruction algorithm to the conventional tomography of 2D objects [Ray94]. Nevertheless, this is not the only rotation scheme valid for phase-space tomography. In Chap. 5 we introduce a different set of projections that is optimized for the reconstruction of the MI of the beam.

On the other hand, since the object is virtual, the projections cannot be measured performing a mechanical rotation of the object (or the detectors around the object) as it is usually done in conventional tomography. Fortunately, there are optical systems whose effect in the beam is a rotation of its WD, like the FRFT [Loh93, Oza93, Men95, Rod09] and Gyrator [Rod07a] implementations. Measuring the intensity of the beam after its propagation through these optical systems is equivalent to measure the projections of the WD associated with the rotation implemented by the optical system. This provides a simple scheme for the measurement of the projections required for a tomographic reconstruction of the beam WD.

The original phase-space tomography method proposed in [Ray94] consists in two steps:

1. Measure a set of the beam fractional power spectra for independent and equidistant angles $\gamma_{x,y}$ covering a π-range interval: the full-range RWT $R\left(x, \gamma_x, y, \gamma_y\right) \equiv S^{\gamma_x,\gamma_y}(\mathbf{r})$. Notice that unlike for 2D objects, now each projection is 2D and hence the RWT is a 4D object.
2. Reconstruct the WD via the double tomographic inversion of $R\left(x, \gamma_x, y, \gamma_y\right)$; first of the pair of variables (y, γ_y), and then of (x, γ_x). This is conceptually equivalent to any other tomographic reconstruction algorithm, except that the data processing is more time consuming.

Although this technique is very powerful—it allows characterizing a beam regardless of its coherence degree—it has not been widely applied for several reasons.

The first problem is the lack of an automatized and accurate system for the acquisition of the fractional power spectra of the beam. The original systems proposed in [Loh93] require the displacement of optical elements, or the variation of the power of spherical lenses, in order to measure the fractional power spectra for different angles. This provided poor accuracy and relatively slow acquisition speed. In some simplified situations only the antisymmetric fractional power spectra are required to fully characterize the beam. In such cases, the projections can be measured using a modification of the optical system to perform the gyrator transform [Rod07a], which only requires an in-plane rotation of cylindrical lenses. This is not, unfortunately, valid for any a priori unknown beam. For the most general case, the optical system relaying on spatial light modulators proposed in [Rod09] is more suitable. This setup

allows measuring the fractional power spectra for any pair of angles without displacing any optical element. It relays in the implementation of digital lenses whose power can be tuned by a computer.

The second problem is the excessive amount of information that needs to be registered and processed in order to recover the WD of the beam. Consider the reconstruction of the WD sampled in a grid of $N \times N \times N \times N$ points with double precision (8 B per sampling point). In this situation, 32 GiB are required only to store the resulting WD with $N = 256$, which does not include the processing of the projection data into the WD. In addition, to obtain the correlation of the beam at two points from the WD the information must be further processed to recover the MI.

This computation problem can be avoided following two different paths. One possible solution is to check if the beam possesses certain symmetries that can be exploited to simplify the reconstruction method. This is the core philosophy of the methods proposed in Chaps. 2, 3 and 4 where the phase-space tomography is simplified for the case of 1D, separable, and rotationally symmetric beams, respectively. The other possible path to avoid the computation problem consists in modifying the original phase-space tomography method to better suit the characterization of the beam. For instance, in Chap. 5 an optimized method to obtain the MI of a beam is presented. The method is similar to the original phase-space tomography, but instead of using the fractional power spectra, it uses other rotations in phase space to obtain the projections required for the complete beam characterization.

References

[Aga00] G.S. Agarwal, R. Simon, Reconstruction of the Wigner transform of a rotationally symmetric two-dimensional beam from the Wigner transform of the beam's one-dimensional sample. Opt. Lett. **25**(18), 1379–1381 (2000)

[Ali05] T. Alieva, M.J. Bastiaans, Alternative representation of the linear canonical integral transform. Opt. Lett. **30**, 3302–3304 (2005)

[Ali08] T. Alieva, in *Advances in Information Optics and Photonics, ICO International Trends in Optics*, ed. by A.T. Friberg, R. Dändliker (SPIE Press, Bellingham, 2008). Chapter First-Order Optical Systems for Information Processing, pp. 1–26

[Ali94] T. Alieva, V. Lopez, F. Agullo-Lopez, L.B. Almeida, The fractional Fourier transform in optical propagation problems. J. Mod. Opt. **41**(5), 1037–1044 (1994)

[Alo11] M.A. Alonso, Wigner functions in optics: describing beams as ray bundles and pulses as particle ensembles. Adv. Opt. Photonics **3**(4), 272–365 (2011)

[Ana94] Y.A. Anan'ev, Y.A. Bekshaev, Theory of intensity moments for arbitrary light beams. Opt. Spectrosc. **76**, 558–568 (1994)

[Bas00] M.J. Bastiaans, Wigner distribution function applied to twisted Gaussian light propagating in first-order optical systems. J. Opt. Soc. Am. A **17**(12), 2475–2480 (2000)

[Bas06] M.J. Bastiaans, T. Alieva, First-order optical systems with unimodular eigenvalues. J. Opt. Soc. Am. A **23**(8), 1875–1883 (2006)

[Bas78] M.J. Bastiaans, The Wigner distribution function applied to optical signals and systems. Opt. Commun. **25**(1), 26–30 (1978)

[Bas91] M. Bastiaans, Second-order moments of the Wigner distribution function in first-order optical systems. Optik **88**(4), 163–168 (1991)

[Cho12] S. Cho, M.A. Alonso, T.G. Brown, Measurement of spatial coherence through diffraction from a transparent mask with a phase discontinuity. Opt. Lett. **37**(13), 2724–2726 (2012)
[Dea99] S.R. Deans, in *The Transforms and Applications Handbook*, ed. by A.D. Poularikas (CRC Press, IEEE Press, Boca Raton, 1999). Chapter Radon and Abel Transforms, pp. 8.1-8.95
[Dra00] D. Dragoman, Can the Wigner transform of a two-dimensional rotationally symmetric beam be fully recovered from the Wigner transform of its one-dimensional approximation? Opt. Lett. **25**(5), 281–283 (2000)
[Dub99] F. Dubois, L. Joannes, J.-C. Legros, Improved three-dimensional imaging with a digital holography microscope with a source of partial spatial coherence. Appl. Opt. **38**(34), 7085–7094 (1999)
[Epp98] B. Eppich, C. Gao, H. Weber, Determination of the ten second order intensity moments. Opt. Laser Tech. **30**(5), 337–340 (1998)
[Gon11] A.I. González, Y. Mejía, Nonredundant array of apertures to measure the spatial coherence in two dimensions with only one interferogram. J. Opt. Soc. Am. A **28**(6), 1107–1113 (2011)
[Goo00] J.W. Goodman, *Statistical Optics*, 1st edn. (Wiley, New York, 2000)
[Gui78] J.-P. Guigay, The ambiguity function in diffraction and isoplanatic imaging by partially coherent beams. Opt. Commun. **26**(2), 136–138 (1978)
[Iac96] C. Iaconis, I.A. Walmsley, Direct measurement of the two-point field correlation function. Opt. Lett. **21**(21), 1783–1785 (1996)
[Ito86] K. Itoh, Y. Ohtsuka, Fourier-transform spectral imaging: retrieval of source information from three-dimensional spatial coherence. J. Opt. Soc. Am. A **3**(1), 94–100 (1986)
[Kak88] A.C. Kak, M. Slaney, *Principles of Computerized Tomographic Imaging* (SIAM, New York, 1988)
[Loh93] A.W. Lohmann, Image rotation, Wigner rotation, and the fractional Fourier transform. J. Opt. Soc. Am. A **10**(10), 2181–2186 (1993)
[Man95] L. Mandel, E. Wolf, *Optical Coherence and Quantum Optics* (Cambridge University Press, New York, 1995)
[Mar99] D.L. Marks, R.A. Stack, D.J. Brady, D.C. Munson, R.B. Brady, Visible cone-beam tomography with a lensless interferometric camera. Science **284**(5423), 2164–2166 (1999)
[Men93] H.M. Ozaktas, D. Mendlovic, Fourier transforms of fractional order and their optical interpretation. J. Opt. Soc. Am. A **101**(34), 163–169 (1993)
[Men95] D. Mendlovic, Y. Bitran, R.G. Dorsch, C. Ferreira, J. Garcia, H.M. Ozaktaz, Anamorphic fractional Fourier transform: optical implementation and applications. Appl. Opt. **34**(32), 7451–7456 (1995)
[Men96] D. Mendlovic, R.G. Dorsch, A.W. Lohmann, Z. Zalevsky, C. Ferreira, Optical illustration of a varied fractional Fourier-transform order and the Radon-Wigner display. Appl. Opt. **35**(20), 3925–3929 (1996)
[Men98] D. Mendlovic, G. Shabtay, A.W. Lohmann∗, N. Konforti, Display of spatial coherence. Opt. Lett. **23**(14), 1084–1086 (1998)
[Nam80] V. Namias, The fractional order Fourier transform and its application to quantum mechanics. IMA J. Appl. Math. **25**(3), 241–265 (1980)
[Naz82] M. Nazarathy, J. Shamir, First-order optics–a canonical operator representation: lossless systems. J. Opt. Soc. **72**(3), 356–364 (1982)
[Oza01] H.M. Ozaktas, Z. Zalevsky, M.A. Kutay, *The Fractional Fourier Transform with Applications in Optics and Signal Processing* (Wiley, New York, 2001)
[Oza93] H.M. Ozaktas, D. Mendlovic, Fractional Fourier transforms and their optical implementation. Opt. Commun. **10**(9), 1875–1881 (1993)
[Pap74] A. Papoulis, Ambiguity function in Fourier optics. J. Opt. **64**(6), 779 (1974)
[Pou00] A.D. Poularikas (ed.), *The Transforms and Applications Handbook* (CRC Press, Boca Raton, 2000)

[Ray94] M.G. Raymer, M. Beck, D.F. McAlister, Complex wave-field reconstruction usign phase-space tomography. Phys. Rev. Lett. **72**(8), 1137–1140 (1994)
[Ric03] J.C. Ricklin, F.M. Davidson, Atmospheric optical communication with a Gaussian Schell beam. J. Opt. Soc. Am. A **20**(5), 856–866 (2003)
[Rod07a] J.A. Rodrigo, T. Alieva, M.L. Calvo, Experimental implementation ofthe gyrator transform. J. Opt. Soc. Am. A **24**(10), 3135–3139 (2007)
[Rod07b] J.A. Rodrigo, T. Alieva, M.L. Calvo, Gyrator transform: propertiesand applications. Opt. Express **15**(5), 2190 (2007)
[Rod09] J.A. Rodrigo, T. Alieva, M.L. Calvo, Programmable two-dimensional optical fractional Fourier processor. Opt. Express **17**(7), 4976–4983 (2009)
[San06] M. Santarsiero, R. Borghi, Measuring spatial coherence by using a reversed-wavefront Young interferometer. Opt. Lett. **31**(7), 861–863 (2006)
[Ser91] J. Serna, R. Martínez-Herrero, P.M. Mejías, Parametric characterization of general partially coherent beams propagating through ABCD optical systems. J. Opt. Soc. Am. A **8**(7), 1094–1098 (1991)
[Sim00b] R. Simon, K.B. Wolf, Structure of the set of paraxial optical systems. J. Opt. Soc. Am. A **17**(2), 342–355 (2000)
[Sim93] R. Simon, N. Mukunda, Twisted Gaussian Schell-model beams. J. Opt. Soc. Am. A **10**(1), 95–109 (1993)
[Sun95] K. Sundar, N. Mukunda, R. Simon, Coherent-mode decomposition of general anisotropic Gaussian Schell-model beams. J. Opt. Soc. Am. A **12**(3), 560–569 (1995)
[Tia12] L. Tian, J. Lee, S.B. Oh, G. Barbastathis, Experimental compressive phase space tomography. Opt. Express **20**(8), 8296–8308 (2012)
[Tu97] T. Jinhong, S. Tamura, Wave field determination using tomography of the ambiguity function. Phys. Rev. E **55**(2), 1946–1949 (1997)
[Wal12] L. Waller, G. Situ, J.W. Fleischer, Phase-space measurement and coherence synthesis of optical beams. Nat. Photonics **6**(7), 474–479 (2012)
[Wal68] A. Walther, Radiometry and coherence. J. Opt. Soc. Am. **58**(9), 1256–1259 (1968)
[Wan08] T. Wang, J. Pu, Z. Chen, Propagation of partially coherent vortex beams in a turbulent atmosphere. Opt. Eng. **47**, 036002 (2008)
[Wig32] E. Wigner, On the quantum correction for thermodynamic equilibrium. Phys. Rev. **40**(5), 749–759 (1932)
[Woo53] P.M. Woodward, *Probability and information theory with applications to radar* (Pergamon Press, New York, 1953)
[Woo94] J.C. Wood, D.T. Barry, Linear signal synthesis using the Radon-Wigner transform. IEEE Trans. Signal Process. **42**(8), 2105–2111 (1994)
[Zer38] F. Zernike, The concept of degree of coherence and its application to optical problems. Physica **5**(8), 785–795 (1938)

Chapter 2
Radon-Wigner Display

2.1 Introduction

In some situations it is not possible, or not desirable, to perform a full characterization of the spatial structure of 2D beams since under certain hypothesis the analysis of 1D beam profiles is more convenient. This is the case of, for example, the spatial coherence study of X-ray sources [She91, Dit96] and rotationally invariant 2D beams, whose WD can be reconstructed from the WD of one of its radial profiles [Aga00]. Therefore, the characterization of 1D beams, which is significantly easier than the characterization of 2D beams, is an important problem with relevant applications.

A 1D beam is described by its complex field amplitude, $f(x)$. Therefore, its MI, $\Gamma(x_1, x_2)$, and WD, $W(x, u)$, are 2D functions. This simplifies the acquisition, storage, and processing of the WD projections, which can be performed using standard computer technology. In fact, considering the information contained in a WD stored in a multiarray of $N = 256$ sampling points per dimension of double precision (8 B), the 32 GiB needed for the 2D case is reduced to 512 KiB in the 1D case. Furthermore, there exist several optical systems [Men96, Gra97, Zha98] suitable for the acquisition in a single measurement of the full-range RWT of the 1D beam. These systems are commonly referred to as RWD.

In this chapter we present a RWD that provides several advantages compared with other RWDs proposed in the literature. Our setup relays in SLMs, which are electronically addressable optical elements introduced in Sect. 2.2. The suggested RWD is presented in Sect. 2.3. It allows measuring the beam RWT for tunable angular range as the intensity distribution at the output plane of the system. In order to experimentally demonstrate the feasibility of our RWD, the WD of several signals are recovered from their measured RWTs in Sect. 2.4. In particular, the extraction of the defining parameters of a windowed chirp signal are studied using different methods. Finally, the WD of the 1D projection of a HG beam and a radial profile of a coherent rotationally invariant 2D beam are reconstructed using the RWD.

A. Cámara, *Optical Beam Characterization via Phase-Space Tomography*,
Springer Theses, DOI 10.1007/978-3-319-19980-1_2

2.2 Spatial Light Modulators for Lens Implementation and Beam Generation

A SLM is an optical device that modifies the beam intensity and phase distributions. The term was originally coined to describe static elements like phase retarders or amplitude filters. These devices convert an input beam described by $f_{\mathrm{i}}(\mathbf{r})$ into [Goo05]

$$f_{\mathrm{o}}(\mathbf{r}) = f_{\mathrm{i}}(\mathbf{r})\, t(\mathbf{r}), \tag{2.1}$$

where

$$t(\mathbf{r}) = t_{\mathrm{A}}(\mathbf{r}) \exp[\mathrm{i}\Psi(\mathbf{r})] \tag{2.2}$$

is the transmission function, t_A is the real function taking values in the range [0, 1] referred to as amplitude transmission, and Ψ is a real function defining the phase modulation. Nowadays, the SLMs based on the liquid crystal on silicon technology can be electronically addressed to dynamically control its modulation properties over time. With the aid of a computer, the transmission function of modern SLMs can be updated at rates around 60 Hz, which make them useful for many applications including adaptive optics in astronomy [Bon90], data storage [Oht99], microscopy [Nei00], or micro-object manipulation using optical tweezers [Wul06]. SLMs are of special importance in this dissertation for the realisation of two tasks: implementing digital lenses with controllable focal length and generating beams with arbitrary spatial structure using computer-generated holograms. For the sake of simplicity, and unless otherwise stated, we will refer with SLM to electronically addressable SLMs using liquid crystal on silicon technology.

The display of a SLM is its optical sensitive element, i.e. the element that actually modulates the beam. It is composed by a 2D array of independent cells or pixels. Each pixel behaves like a neutral density filter or phase retarder—depending on whether the SLM is working in amplitude or phase modulation—independently controllable from a computer. In the case of an amplitude-only SLM the pixel can take values in the range [0, 1], where the values 0 and 1 correspond to opaque and completely transparent filters, respectively. Conversely, in the case of a phase-only SLM the pixel can usually retard the beam in a full 2π-range interval, although in some situations a smaller or larger range can be addressed. Every pixel may only take concrete values contained in the SLM dynamic range, usually formed by 256 values. Commonly, SLMs are specialized in modifying the amplitude or phase of the beam, not both at the same time. In addition, depending on whether the modified beam is transmitted through or reflected from the device, the SLMs are further classified into transmission and reflection SLMs. Unless otherwise stated, we will assume reflection SLMs operating in phase-only modulation regime for a full 2π-range interval when referring to SLMs.

An interesting application of SLMs is the implementation of thin lenses of variable focal length. A thin lens can be considered a transmission phase mask with quadratic phase modulation function. For example, a spherical lens of focal length f is described in thin-lens and paraxial approximation by the phase mask [Goo05],

$$t(\mathbf{r}) = \exp\left[-\frac{\mathrm{i}\pi}{\lambda \mathrm{f}}\left(x^2 + y^2\right)\right], \tag{2.3}$$

where λ is the wavelength of the incident light. This kind of lenses can be digitally implemented by phase-only SLMs. Notice that since the SLM is formed by pixels with finite size that are separated by a certain distance, the phase transmission can only be correctly implemented in the areas where the phase oscillations are not very rapid in order to satisfy the Nyquist sampling theorem [Goo05]. Consider the phase modulation function for a thin-lens defined by Eq. (2.3), which is displayed in Fig. 2.1 for $\lambda = 532$ nm and focal lengths of 0.75 and 0.25 m. The phase difference between two consecutive horizontal pixels with positions k and $k+1$ is given by

$$\Delta\Psi_k = \Psi\left[(k+1)\,\Delta x\right] - \Psi\left(k\Delta x\right) = \pi\,(2k+1)\,\frac{(\Delta x)^2}{\lambda \mathrm{f}}, \tag{2.4}$$

where Δx is the separation between pixels, also known as pixel pitch. If the phase difference is bellow half a phase cycle, i.e. $\Delta\Psi_k < \pi$, there are more than two samples per phase cycle and the phase amplitude is well-sampled according to the Nyquist theorem. On the contrary, if the phase difference is above half cycle then the phase modulation is sampled with less than two samples per cycle and, therefore, the phase is undersampled. In order to assure the quality of the lenses we impose a more restrictive sampling condition. Instead of using two pixels per cycle, we require six pixels per cycle to consider the phase mask well sampled. Since we discard the

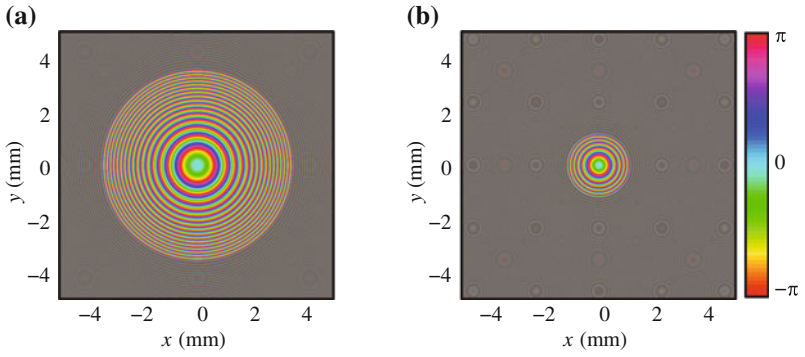

Fig. 2.1 Phase modulation corresponding to thin-lenses of focal lengths **a** 0.75 m and **b** 0.25 m. When using a SLM with pixel pitch 18 μm, the shaded areas are sampled with a rate below 6 pixels per cycle and are not used to avoid their associated optical aberrations. Notice that reducing the focal length of the digital lens reduces its effective aperture

light that falls into the areas where this condition is not satisfied, each digital lens has a virtual circular aperture of size $k_{\text{lim}}\Delta x$, where

$$\Delta\Psi_{k_{\text{lim}}} = \pi/3 \quad \Rightarrow \quad k_{\text{lim}} = \frac{1}{3}\left[\frac{\lambda \text{f}}{2\,(\Delta x)^2} - 1\right]. \tag{2.5}$$

This apertures are present in Fig. 2.1 for a SLM of pixel pitch 18 μm. Notice that this means that reducing the focal length of the digital lens reduces its virtual aperture. In all the experiments of the dissertation where digital lenses are involved we have checked that the generated signals fall into the sufficiently sampled zones.

Apart from the digital lenses, SLMs can implement phase-only CGHs for the high-fidelity generation of coherent beams with on-demand amplitude and phase distributions [Arr07]. The technique consists in illuminating a phase mask, the hologram, with a reference beam, usually an approximation of a plane wave. In our case the expanded, filtered, and collimated Gaussian beam of a laser source is used for this goal, see Fig. 2.2. When the waist of the Gaussian is significantly wider than the signal to be generated, its central region can be approximated to a plane wave. The hologram converts the reference beam into a beam whose Fourier expansion with respect to the phase distribution, $\phi\,(\mathbf{r})$, contains a term that is the desired beam. In order to obtain in the first term of the Fourier expansion the signal described by

$$f\,(\mathbf{r}) = a\,(\mathbf{r})\exp\left[\text{i}\phi\,(\mathbf{r})\right], \tag{2.6}$$

where a and ϕ are its amplitude and phase distributions, the phase modulation function, $h\,(\mathbf{r}) = \exp\left[\text{i}\Psi\,(\mathbf{r})\right]$, that satisfies the following relations has to be found [Arr07]

$$\Psi\,(\mathbf{r}) = g\left[a\,(\mathbf{r})\right]\phi\,(\mathbf{r}), \tag{2.7}$$

$$\text{sinc}\left\{1 - g\left[a\,(\mathbf{r})\right]\right\} = a\,(\mathbf{r}), \tag{2.8}$$

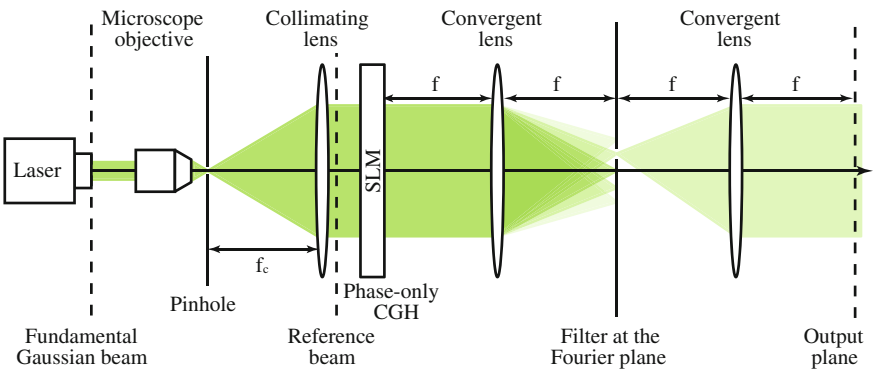

Fig. 2.2 Scheme of the optical system used for the signal generation using phase-only computer generated holography

where $\text{sinc}(\mathbf{r}) = \sin(\pi x)\sin(\pi y)/(\pi^2 xy)$ and g is an arbitrary function that depends on the amplitude distribution. The solution for g has no analytic expression; hence it has to be numerically inverted from Eq. (2.8).

The conditions given by Eqs. (2.7) and (2.8) define a special kind of CGH referred to as CGH of type I in [Arr07]. There are alternative ways to construct the hologram, see for instance the type II and III CGHs of [Arr07], that provide higher-fidelity on the generated beam. We will use type I CGHs throughout the dissertation, however, due to their greater energy efficiency and because they do not require additional masks on the SLM for its implementation.

The generated signal contains all the Fourier series terms, including the desired beam $f(\mathbf{r})$,

$$h(\mathbf{r}) = \sum_m C_m [a(\mathbf{r})] \exp[im\phi(\mathbf{r})], \tag{2.9}$$

where C_m are the expansion coefficients which depend on the amplitude $a(\mathbf{r})$. In order to isolate the desired signal, corresponding to the first term, we include a carrier in the phase distribution of f:

$$f(\mathbf{r}) \longrightarrow f(\mathbf{r}) \exp(i2\pi \mathbf{r} \cdot \mathbf{k}_c), \tag{2.10}$$

where $\mathbf{k}_c = (k_{x,c}, k_{y,c})$ is the carrier frequency. The qth order Fourier term is affected by a carrier of frequency $q\mathbf{k}_c$. Therefore, each expansion term is spatially separated at the Fourier plane of a 4-f telescopic system [Goo05], where all the terms except the $q = 1$ are filtered. In addition, due to the pixelated nature of the SLM, other diffraction orders appear at the Fourier plane, complicating the filtering of the desired term. An illustration of the different orders present at the Fourier plane is displayed in Fig. 2.3. Also consider that the suppression of most of the terms present at the Fourier plane makes CGH an energetically inefficient technique. Despite these inconveniences, CGHs excel at the generation of beams with arbitrary and dynamically-changeable phase and amplitude distributions. The scheme of this optical system is displayed in Fig. 2.2.

Although the higher the carrier frequency the easier it is to filter the undesired terms in the Fourier plane, it is not possible to choose carriers with arbitrary frequencies; they are limited by the Nyquist sampling theorem just like the focal length of digital lenses. For the case of a SLM with pixel pitch of 8 μm, the limiting carrier frequency according to Nyquist theorem is two pixels per cycle, $k_{x,0} \sim k_{y,0} \sim 60\ \text{mm}^{-1}$. In order to assure the quality of the carrier, however, we used in the experiments a lower frequency carrier of six pixels per cycle, $k_{x,0} \sim k_{y,0} \sim 20\ \text{mm}^{-1}$.

These two applications – the phase-mask implementation and beam generation – will be used throughout the dissertation. In particular, as we will see in the following Sections, the RWD proposed by us uses SLMs to augment its versatility, producing important advantages.

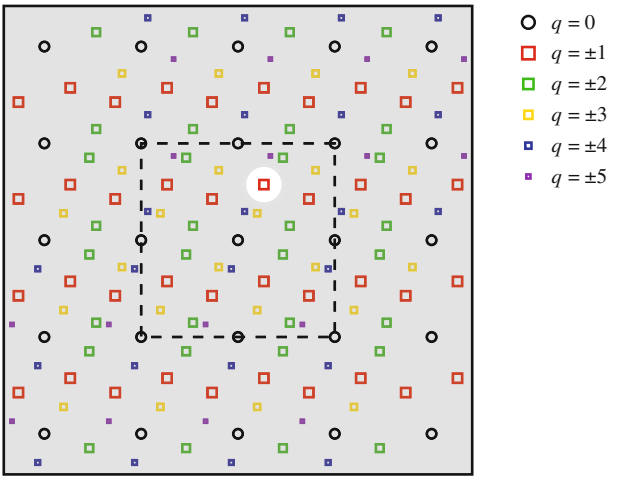

Fig. 2.3 Illustration of the different contributions obtained in the Fourier plane of the 4-f telescope for a typical CGH. *Black circles* represent the zero-order term of the Fourier expansion, while *coloured squares* represent the different expansion orders. *Squares* have different size depending on the order they represent, since higher orders carry fewer energy. An opaque mask, shaded in *grey*, is used to filter the desired first order

2.3 Programmable Radon-Wigner Display

In 1994 Wood and Barry proposed to use the RWT instead of the WD to analyze a multicomponent linear FM signal [Woo94]. While the signal components are entangled in the WD representation, they are easily identified in the RWT as local intensity maxima. This idea, originally developed for the analysis of the temporal behaviour of electrical signals, was promptly imported to the analysis of spatial behaviour of optical signals. The first optical RWD [Men96] consisted in two Fresnel zone plates, Z_1 and Z_2, and a charge-coupled device (CCD) camera separated by a fixed distance z, see Fig. 2.4a. Each Fresnel zone plate is divided in channels as illustrated in Fig. 2.4b, with each channel implementing a 1D lens of different power.

This RWD is based in the type II Lohmann FRFT optical system, recall Fig. 1.6b. The main difference is that the variable free-space propagation of the FRFT system is replaced in the RWD by an equivalent optical system whose elements do not require to be displaced in order to achieve different FRFT angles. It is easy to demonstrate by ABCD-matrix multiplication that the system formed by three lenses of focal length z, f, and z, respectively, separated by a distance z presented in Fig. 2.5 is equivalent to a free-space propagation for distance $z' = z\,(2 - \lambda/\mathrm{f})$ [Loh95, Men96]:

$$\begin{bmatrix} 1 & 0 \\ -\frac{\lambda}{z} & 1 \end{bmatrix} \begin{bmatrix} 1 & \frac{z}{\lambda} \\ 0 & 1 \end{bmatrix} \begin{bmatrix} 1 & 0 \\ -\frac{\lambda}{\mathrm{f}} & 1 \end{bmatrix} \times \begin{bmatrix} 1 & \frac{z}{\lambda} \\ 0 & 1 \end{bmatrix} \begin{bmatrix} 1 & 0 \\ -\frac{\lambda}{z} & 1 \end{bmatrix} = - \begin{bmatrix} 1 & \frac{z\left(2-\frac{\lambda}{\mathrm{f}}\right)}{\lambda} \\ 0 & 1 \end{bmatrix}. \tag{2.11}$$

This equivalence allows replacing the variable propagation distance for different FRFT angles into a fixed-distance system with variable focal lenses. Embedding this system into two thin lenses of equal focal length, $\mathrm{f} = \mathrm{f}_0 \cot(\gamma/2)$, and setting $z' = \mathrm{f}_0 \sin\gamma$, the FRFT of type II for angle γ is obtained. Since we are only interested in the intensity distribution at the output plane of the system, the third lens is not required. Each channel of the RWD performs the FRFT for certain angle using the same approach. If the angles are chosen to cover the range $[\pi/2, 3\pi/2]$, the intensity at the output of the optical system corresponds to the full-range RWT of the input signal. Unfortunately, the lenses generated by Fresnel zone plates produce distortions to the incident beam and multiple foci, which reduce the quality of the RWT.

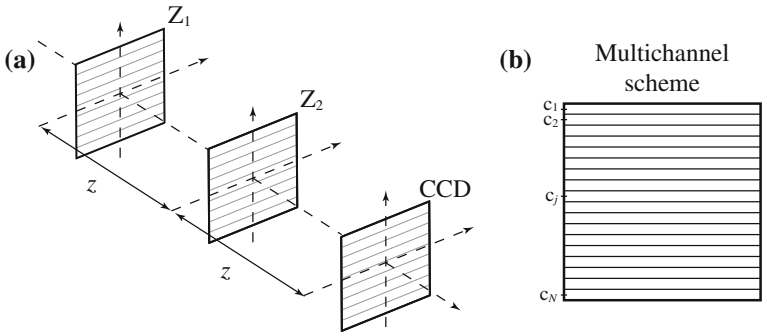

Fig. 2.4 **a** First optical RWD implementation consisting in two Fresnel zone plates, $Z_{1,2}$ separated by a fixed distance z. The beam full-range RWT can be measured at the output plane, which is placed at a distance z from the second Fresnel zone plate. **b** Detail of the multichannel optical system elements, where c_j represents the jth channel

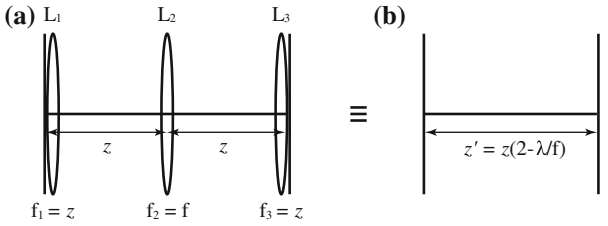

Fig. 2.5 Equivalent optical systems. **a** Optical system composed by three spherical convergent lenses, $\mathrm{L}_{1,2,3}$, with focal lengths z, f, and z, respectively, separated by the same distance z. **b** Free-space propagation for distance $z' = z\,(2 - \lambda/\mathrm{f})$

An alternative RWD avoiding the use of Fresnel zone plates was proposed in [Gra97]. It consists in a cylindrical and a varifocal lens and circumvents the zone plate distortions. The RWTs measured with the system present, however, a significant inconvenience: each WD projection has a different magnification. This means that a pre-process of the RWT to compensate the magnifications is required prior to the WD reconstruction. Moreover, the projections are measured with different resolution by a digital camera, which affects the WD recovery. Another RWD proposal, based on the use of varifocal lenses, prevented the different magnification [Zha98] but required the measurement of the RWT in a curved surface, unsuitable for the use of conventional cameras. Despite the successful analysis performed by these systems, they have not been widely applied.

In order to avoid most of the previous inconveniences, we propose [Cám11a] a RWD without significant projection distortions which provides RWTs with uniform magnification. It is based on the original optical system proposed by Mendlovic et al. [Men96] but with two important differences:

1. SLMs are used to implement the phase masks instead of Fresnel zone plates.
2. Additional cylindrical lenses are included to compensate the beam free-space propagation in the y direction.

The proposed RWD is versatile because it uses SLMs which can be programmed. This allows, for example, taking multiple RWTs for partial angular range and assemble them into a full angular range RWT with increased number of projections. Moreover, as we will see in Chap. 5, the same configuration of SLMs, without the cylindrical lenses, can be programmed to obtain the WD projections of 2D beams.

An illustration of the proposed system is displayed in Fig. 2.6a. It consists in two SLMs separated a fixed distance z, and two cylindrical lenses of focal length $z/4$ with phase modulation in the y direction also separated a fixed distance z. The SLMs implement the multichannel phase masks that were originally implemented by Fresnel zone plates in [Men96]. Each channel of the phase mask can be programmed to perform the FRFT operation for an arbitrary angle in the range $[\pi/2, 3\pi/2]$. In order to acquire the full-range RWT for N equidistant angles, the jth channel of the ith SLM implements the transmission function $t_i\,(x,\, j)$ given by:

$$t_1\,(x,\, j) = \exp\left[\mathrm{i}\Psi_1\,(\mathbf{r})\right] = \exp\left[-\mathrm{i}\pi\,\frac{x^2}{\sigma^2}\left(2 - \cot\frac{\gamma_j}{2}\right)\right], \tag{2.12}$$

$$t_2\,(x,\, j) = \exp\left[\mathrm{i}\Psi_2\,(\mathbf{r})\right] = \exp\left[-\mathrm{i}4\pi\,\frac{x^2}{\sigma^2}\left(1 - \sin\gamma_{N-j+1}\right)\right], \tag{2.13}$$

where $j = 1, \ldots, N$, $\gamma_j = \pi/2 + (j-1)/N\pi$ is the FRFT angle associated with the jth channel, and $\sigma = \sqrt{2\lambda z}$ is the scale parameter of the system. Phase masks corresponding to $z = 1$ m are displayed in Fig. 2.6b. The initial and final SLM rows are filled with phase masks corresponding to the first and last FRFT angles, respectively, in order to avoid edge effects, see Fig. 2.6b. Consequently, the meaningful area of the intensity distribution at the RWD output plane, which corresponds to the

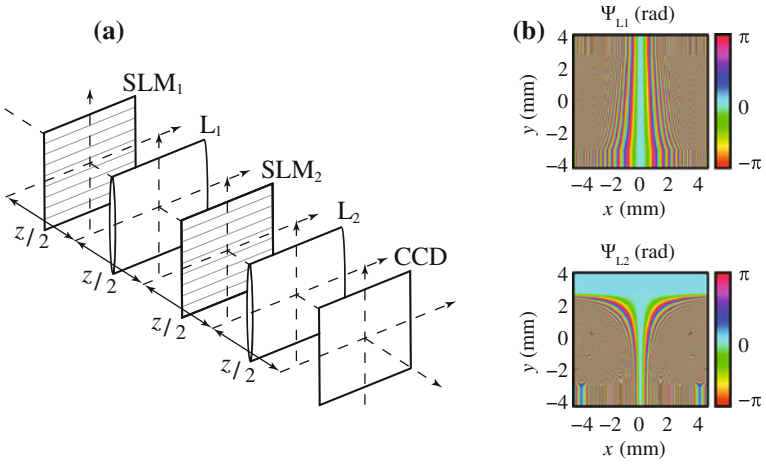

Fig. 2.6 **a** Implementation of the RWD consisting in two SLMs, SLM_1 and SLM_2, and two cylindrical lenses, L_1 and L_2. **b** Phase masks implemented by the SLMs. The FRFT angle changes in the vertical direction

RWT, has to be extracted. While the SLMs perform the FRFT in the x direction, the cylindrical lenses compensate the beam propagation in the y direction by imaging the first SLM into the second, and the second into the output plane. Notice since the first cylindrical lens inverts the channel position, the jth channel of the second SLM implements the angle labelled by $N - j + 1$ in Eq. (2.13). At the output plane, placed at a distance $z/2$ from the last cylindrical lens, a CCG camera registers the RWT of the input signal.

The use of SLMs, which compared with Fresnel zone plates or varifocal lenses are more expensive optical elements, is justified by the high versatility of the resulting RWD. In particular, a key advantage of the system is that we can increase the number of WD projections in the RWT by measuring multiple partial angular range RWTs. For example, instead of registering the full-range RWT for N equidistant angles, it is possible to measure two RWTs of N equidistant angles covering the ranges $[\pi/2, \pi)$ and $[\pi, 3\pi/2)$, which result in a full-range RWT with $2N$ projections. As we have seen before, c.f. Fig. 1.9, we will experimentally verify that increasing the number of projections is beneficial for the WD reconstruction. The effects of single-shot, only one RWT measurement, and double-shot, two measurements, are investigated in the experimental results.

Each channel of the RWD expects at its input plane a copy of the 1D signal to be analyzed. These multiple copies can be obtained from a 1D profile of a 2D beam using the setup proposed in [Aga00], which is reproduced in Fig. 2.7. It relays in a slit mask to filter the desired profile and its further expansion using cylindrical lenses. An inconvenience of this system is that the slit diffraction alters the results and drastically reduces the power carried by the signal that has to be processed by the RWD.

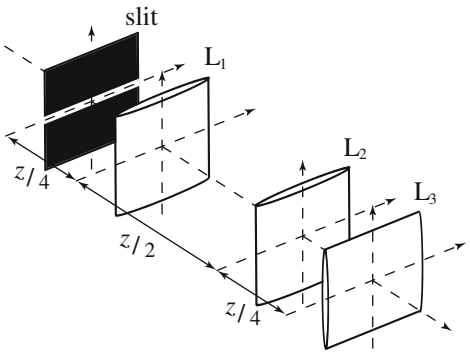

Fig. 2.7 Optical system proposed in [Aga00] for converting a 1D profile of a 2D beam into the signal expected by the RWD, which is a multiple copy of the profile along the y direction. It consists in a slit and three cylindrical lenses. The slit is responsible for selecting a profile of the 2D beam. Lenses L_1 and L_2 implement a 4-f telescope for the x direction. Lens L_3 expands the profile in the y direction. The cylindrical lenses L_1 and L_2 have the same focal length $f_1 = f_2 = z/4$ and are separated a distance $z/4$ and $3z/4$ from the slit plane. They have the phase modulation axis in the x direction. The final cylindrical lens, L_3, with focal length $f_3 = z$, is placed at a distance z from the slit and has the phase modulation axis in the y direction

2.4 Experimental Results

The proposed programmable RWD has been created using two Holoeye LC-R 2500 reflection SLMs with resolution 1024×768, pixel pitch 19 μm, and 8-bit dynamic range; a Ophir-Spiricon SP620U CCG camera of resolution 1600×1200, pixel pitch 4.4 μm, and 12-bit dynamic range; and two cylindrical thin lenses of focal length 0.25 m. The collimated beam from a Nd:YAG laser of $\lambda = 532$ nm illuminates the first SLM. A custom MATLAB package has been developed for the automatized setup manipulation and processing of the acquired data.

In order to test our RWD implementation we experimentally measured the full-range RWT of several 1D test signals: window, windowed chirp, 1D HG beam, and the radial profile of a 2D rotationally invariant beam. The WD of these signals are reconstructed from the full-range RWT for $\gamma \in [\pi/2, 3\pi/2)$ applying the filtered back-projection algorithm, see Sect. 1.5. For the experimental verification of the proposed scheme we skip the step of 1D signal expansion that, as it has been explained, can be performed using the additional setup displayed in Fig. 2.7. Instead, we generate the input signals in the first SLM of the RWD using a phase-only CGH as explained in Sect. 2.2. Notice that the tasks of lens multiplication and beam generation are performed by implementing a hologram encoding the product of the desired signal, f, and the RWD phase mask:

$$f_{\mathrm{SLM1}}(x, y) = f(x)\, t_1(x, j), \tag{2.14}$$

where j is the channel associated with the value of the vertical coordinate y.

The first test beam for the experimental demonstration of our RWD is a window signal rect (x/w) with $w = 2.47$ mm, where rect is the rectangle function defined by

$$\text{rect}\,(x) = \begin{cases} 1, & \text{if } |x| < 1, \\ 1/2, & \text{if } |x| = 1, \\ 0, & \text{otherwise.} \end{cases} \tag{2.15}$$

Its full-range RWT is obtained from a single-shot intensity measurement consisting in 293 WD projections for equidistant angles in the interval $[\pi/2, 3\pi/2)$. Since the pixel pitch of the SLM is larger than the pixel pitch of the CCG camera, four intensity rows of the acquired RWT correspond to a single channel in the SLM. Therefore, the rows are averaged to obtain the final RWT. To avoid a possible power inequality for different fractional power spectra in the RWT, each WD projection is normalised to unity power. This is justified by the Parseval theorem as introduced in Eq. (1.55). Finally, the acquired data has been processed using the filtered back-projection algorithm yielding the WD of the test beam.

The experimental RWT and WD are compared with the theoretical ones in Fig. 2.8. The good agreement between the theoretically predicted and the experimental results proves the feasibility of the RWD. In particular, several WD fringes are clearly observed above and bellow the main lobe of the WD. Notice that the method allows reconstructing the negative values of the WD observed as blue colours in Fig. 2.8b which is required for performing a quantitative characterization of the beam. Concretely, the beam MI can be obtained from the WD applying Eq. (1.17).

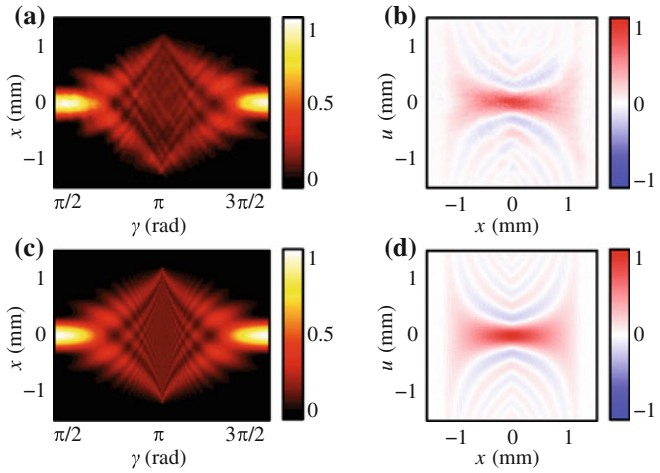

Fig. 2.8 **a** Experimental single-shot full-range RWT consisting in $N = 293$ WD projections of a window signal with $w = 2.47$ mm. **b** Experimental WD reconstructed from the RWT. **c** Simulated RWT consisting in the same projections for the window signal. **d** Simulated WD for the window signal. Notice that both WDs present the negative values characteristic of coherent beams

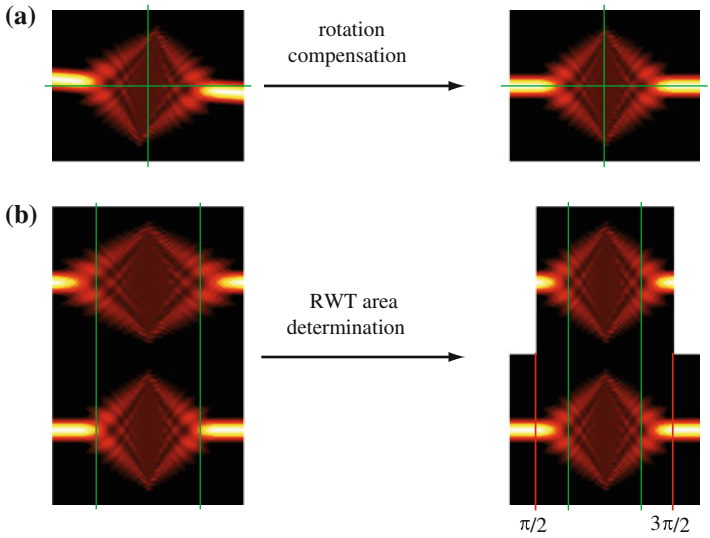

Fig. 2.9 Illustration of the RWD calibration process. The concrete area of the RWT is obtained comparing the measured RWT with the theoretical expected one. The WD projections associated with the angles $\pi/2$ and $3\pi/3$ are determined by resizing the theoretical RWT until some characteristic of both RWTs are aligned. *Green lines* going through the first and last projections of null intensity in their centre are used in this example (Color figure online)

The extraction of the full-range RWT from the measured intensity distribution requires a prior calibration of the RWD. In the case of the window signal it has been performed comparing the theoretically expected RWT with the measured intensity distribution as illustrated in Fig. 2.9. The WD projections associated with the angles $\pi/2$ and $3\pi/3$ are determined by resizing the angular axis of the theoretical RWT until some characteristic of both RWTs are aligned. In our case we use as characteristics the first and last projections with zero intensity in their centre, see green lines in Fig. 2.9. This calibration process allows defining the region of interest corresponding to the RWT for other signals. The procedure is also crucial for assembling full-range RWTs in double- or multiple-shot experiments.

In order to explore the benefits associated with the versatility of SLMs, we characterise a more complex beam: a windowed chirp. This signal is described by the complex amplitude $f(x) = \mathrm{rect}(x/w)\exp\left[\mathrm{i}\pi x^2/(\lambda \mathrm{f_c})\right]$. For the experiments we set the window width and the chirp parameter as $w = 2.47$ mm and $\mathrm{f_c} = 0.93$ m, respectively. In a first experiment we measure a full-range RWT with 293 projections by a single shot, see Fig. 2.10a, from which the WD is reconstructed, see Fig. 2.10b.

In a second experiment we measure a full-range RWT by two shots. This means that from two measurements of the RWT for ranges $[\pi/2, \pi)$ and $[\pi, 3\pi/2]$ with 293 WD projections each one, a full-range RWT with 586 WD projections is assembled, see Fig. 2.10c. As in the previous experiment, we reconstruct the WD, which is displayed in Fig. 2.10d. The critical step in the double-shot experiment is the assemblage

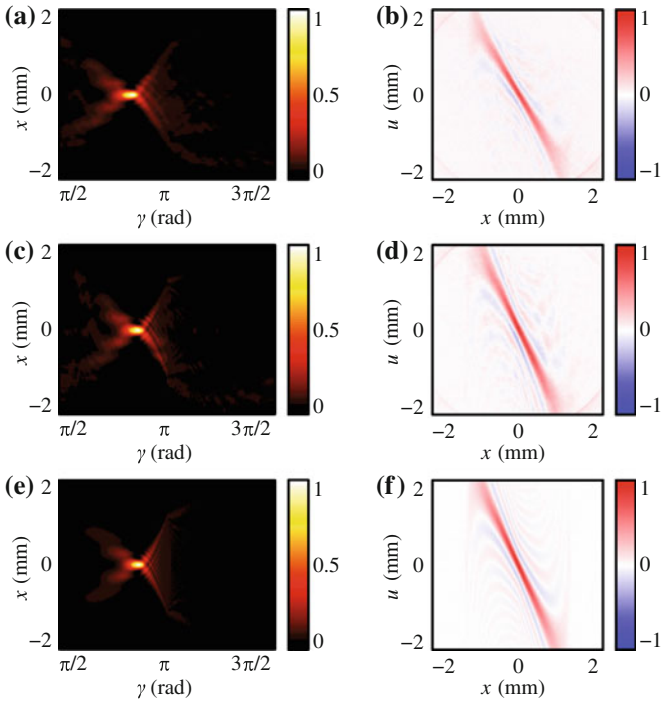

Fig. 2.10 **a** Experimental single-shot RWT consisting in 293 WD projections in the $[\pi/2, 3\pi/2)$ range of a windowed chirp signal with $w = 2.47$ mm and $f_c = 0.93$ mm. **b** Experimental WD reconstructed from the RWT. **c** Experimental RWT obtained by assembling two single-shot RWTs each consisting in 293 WD projections in the $[\pi/2, \pi)$ and $[\pi, 3\pi/2)$ ranges, respectively. **d** Experimental WD reconstructed from the double-shot RWT. **e** Simulated RWT containing the same projections as in the double-shot experiment. **f** Simulated WD for the windowed chirp signal. Notice that, as expected, all the WDs present negative values

of the WD projections obtained in both measurements into the full-range RWT. This is accomplished following the calibration process mentioned above.

In order to better compare the quality of the measured RWTs and reconstructed WDs for single- and double-shot experiments, the theoretically expected RWT and WD are presented in Fig. 2.10e, f, respectively. Since the double-shot RWT contains more information of the beam than the single-shot RWT, its reconstructed WD presents greater fidelity with the theory expectation. This can be appreciated comparing Fig. 2.10b, d, where the fine details around the main lobe are better resolved for the double-shot case. This quality improvement is reflected in a better accuracy of the beam characteristics extracted from the RWT and the WD, as we will see further.

Both the measured RWT and the reconstructed WD contain all the information of the beam spatial structure. Indeed, as it has been mentioned in [Woo94], the chirp parameter is easily obtained from the RWT by finding the FRFT angle associated with the narrower WD projection, γ_k, see Fig. 2.11. The relation between the chirp parameter and γ_k is given by

$$\mathrm{f_c}\left(\gamma_k\right) = -\frac{\sigma^2}{\lambda}\tan\gamma_k. \tag{2.16}$$

Neglecting all factors contributing to the measurement precision except the finite separation between angles, $\Delta\gamma_k$, the chirp parameter precision is calculated as:

$$\Delta\mathrm{f_c}\left(\gamma_k\right) = \left|\frac{\mathrm{df_c}\left(\gamma_k\right)}{\mathrm{d}\gamma_k}\right|\Delta\gamma_k = \frac{\sigma^2\Delta\gamma_k}{\lambda\cos^2\left(\gamma_k\right)}. \tag{2.17}$$

Notice that when the FRFT angles are equidistant, $\Delta\mathrm{f_c}$ depends indirectly on the total number of projections of the RWT, N, since $\Delta\gamma_k = \pi/N$. Hence, increasing the number of WD projections contained in the RWT, for example performing a double-shot experiment, is a convenient way to make the chirp parameter estimation more precise.

The chirp parameters obtained from the measured RWTs in single- and double-shot experiments are summarized in Table 2.1. Notice that the precision of the double-shot experiment is higher than the precision of the single-shot experiment. In both cases, however, the precision is overestimated since the contributions related to the calibration of the RWT and the errors associated with the chirp generation using a CGH are being ignored. That explains why none of the chirp parameter estimations is compatible with the expected value. Nevertheless, this analysis proves that increasing the number of shots to measure the RWT, and thus effectively increasing the number of WD projections in the RWT, beam characteristics with higher precision can be recovered.

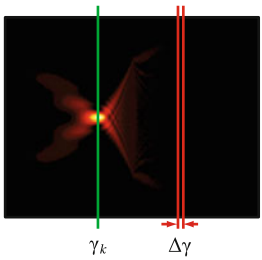

Fig. 2.11 Illustration of the quantities required to estimate the chirp parameter from the measured RWT. The *green line* is a visual aid to estimate the γ_k angle (Color figure online)

Table 2.1 Chirp parameter with its associated precision obtained from the single-shot and double-shot experiments and expected by theory

	Chirp parameter	
	$\mathrm{f_c}$ (mm)	$\Delta\mathrm{f_c}$ (mm)
Single-shot	1.09	0.03
Double-shot	0.905	0.014
Theory	0.93	

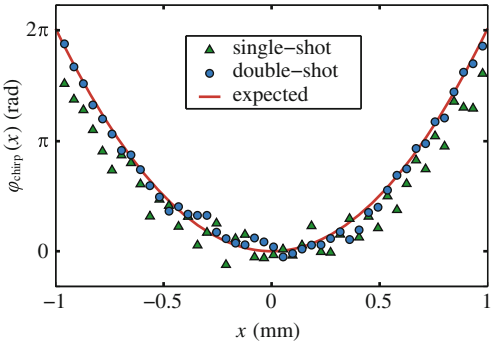

Fig. 2.12 Phase distributions of the chirp signal relative to the origin point, $x_0 = 0$. (*Triangle*, △) Experimental phase distribution for the single-shot RWT consisting in 293 WD projections. (*Circle*, ○) Experimental phase distribution for the double-shot RWT consisting in 586 WD projections. (*Line*) Theoretically expected phase distribution

In addition to beam characteristics, like the chirp parameter, local information of the spatial structure of the beam can be extracted from the reconstructed WD. In particular, from the MI obtained by applying Eq. (1.17), the beam phase distribution is directly recovered. The phase distribution relative to the point $x_0 = 0$, i.e. $\arg\Gamma(x, x_0)$, is compared between the single- and double-shot experiments with theoretical expectation in Fig. 2.12. As opposed to the global information included in the signal parameters, the phase distribution provides local information, which is important for numerous applications for example in microscopy.

The proposed method and system is not only working in simple signals like the window and windowed chirp examples. The same procedure can be applied to obtain the WD of other signals. For instance, in Figs. 2.13 and 2.14 there are displayed, respectively, the theoretical and experimental WDs of:

- the 1D HG mode $\mathscr{H}_4(x)$ for $w = \sigma = 0.72$ mm, and
- the radial profile ($y = 0$) of the combination of LG modes $f_{\mathrm{LG}}(\mathbf{r}) = \mathscr{L}_0^0(\mathbf{r}) + 2\mathscr{L}_2^0(\mathbf{r})$ with $w = \sigma = 0.72$ mm.

It is evident, when analyzing its RWT, that the HG beam is an eigenfunction of the FRFT operator since all its WD projections present the same form. This is reflected in the WD by its rotationally invariant structure. It also means that the beam preserves its shape during free-space propagation. This is not the case for the radial profile of the f_{LG} beam because its projections are not identical. Notice that since f_{LG} is rotationally invariant we can obtain its 4D WD from the WD of its radial projection following the procedure proposed in [Aga00].

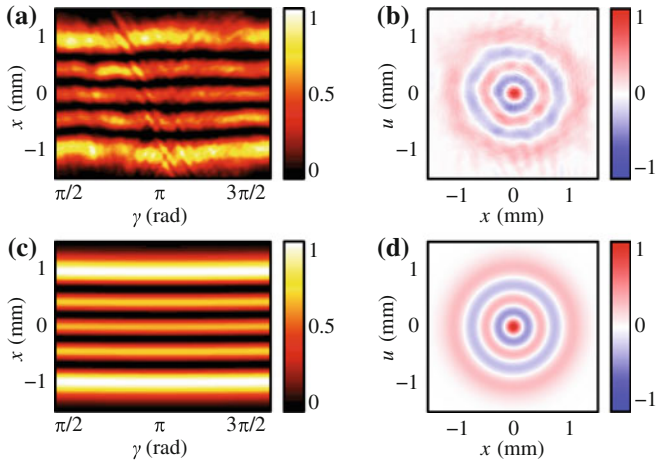

Fig. 2.13 Analysis of the $\mathscr{H}_4(x)$ beam with $w = 0.72$ mm. **a** Experimental single-shot full-range RWT consisting in 293 WD projections. **b** Experimental WD reconstructed from the RWT. **c** Simulated RWT. **d** Simulated WD

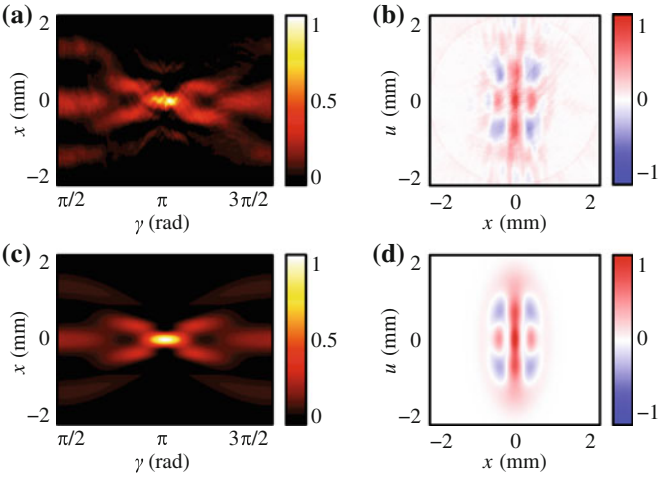

Fig. 2.14 Analysis of the radial profile of the combination $\mathscr{L}_{0,0} + 2\mathscr{L}_{2,2}$ with $w = 0.72$ mm. **a** Experimental double-shot full-range RWT consisting in 586 WD projections. **b** Experimental WD reconstructed from the RWT. **c** Simulated RWT. **d** Simulated WD

2.5 Conclusions

The good agreement between the experimental results and the theoretical expectations allows concluding that the proposed RWD is feasible for the analysis of 1D signals. In particular, this includes the characterization of pure 1D signals and 1D profiles of 2D beams. Furthermore, the WD of 2D rotationally invariant beams can

be recovered from the WD of its radial profile via [Aga00]. Although the experimental results were obtained for completely coherent beams, the method is coherence agnostic and should be equally feasible for partially coherent beams.

The exploration of double-shot experiments to determine the beam RWT has lead us to important results. Indeed, performing multiple shots assembled into the full-range RWT increases the number of its WD projections, which in turn improves the quality of the WD reconstruction and precision of the quantitative beam characterization. The single- and double-shot experiments have been studied for the case of a windowed chirp signal. Although it is reasonable to think that the WD quality will improve for more than two shots, this improvement is limited by the errors introduced in the calibration process. Moreover, since the information is not obtained from a single measurement, it cannot be used for processes that rapidly change in time.

Another advantage of using the suggested RWD is its ability to centre the beam analysis in certain RWT region of interest. For example, consider that we already knew that the chirp parameter of an unknown signal is around certain FRFT angle, γ. Then, instead of measuring a single-shot full-range RWT, we could measure the single-shot RWT for range $[\gamma - \epsilon, \gamma + \epsilon)$ where ϵ defines the region of interest. This procedure is trivial to perform using the proposed RWD and leads to more precise beam characterization.

Unfortunately, these advantages are only pertinent to the characterization of 1D beams. For the more general case of 2D signals, different simplified methods are proposed. For instance, in the following chapters, the method for the analysis of 2D signals that are separable in Cartesian coordinates is explored. As we will demonstrate, in a certain way 2D separable beams are similar to 1D beams.

Most of the results of this chapter are published in [Cám11b] and were presented at the congresses [Cám11a, Cám11c].

References

[Aga00] G.S. Agarwal, R. Simon, Reconstruction of the Wigner transform of a rotationally symmetric two-dimensional beam from the Wigner transform of the beam's one-dimensional sample. Opt. Lett. **25**(18), 1379–1381 (2000)

[Arr07] V. Arrizón, U. Ruiz, R. Carrada, L.A. González, Pixelated phase computer holograms for the accurate encoding of scalar complex fields. J. Opt. Soc. Am. A **24**(11), 3500–3507 (2007)

[Bon90] D. Bonaccini, G. Brusa-Zappellini, S. Esposito, P. Salinari, P. Stefanini, Adaptive optics wavefront corrector using addressable liquid crystal retarders. SPIE Proc. **1543**, 89–97 (1990)

[Cám11a] A. Cámara, T. Alieva, J.A. Rodrigo, M.L. Calvo, Optical systems and algorithms for phase-space tomography of one- and two-dimensional beams. in *22nd Congress of the ICO* (2011)

[Cám11b] A. Cámara, T. Alieva, J.A. Rodrigo, M.L. Calvo, Phasespace tomography with a programmable Radon-Wigner display. Opt. Lett. **36**(13), 2441–2443 (2011)

[Cám11c] A. Cámara, T. Alieva, J.A. Rodrigo, M.L. Calvo, Radon-Wigner display implemented by spatial light modulators. in *PIERS Proceedings* (2011)

[Dit96] T. Ditmire, E.T. Gumbrell, R.A. Smith, J.W.G. Tisch, D.D. Meyerhofer, M.H.R. Hutchinson, Spatial coherence measurement of soft X-ray radiation produced by high order harmonic generation. Phys. Rev. Lett. **77**, 4756–4759 (1996)

[Goo05] J.W. Goodman, *Introduction to Fourier Optics* (Roberts & Company, Colorado, 2005)

[Gra97] S. Granieri, W.D. Furlan, G. Saavedra, P. Andres, Radon-Wigner display: a compact optical implementation with a single varifocal lens. Appl. Opt. **36**(32), 8363–8369 (1997)

[Loh95] A.W. Lohmann, A fake zoom lens for fractional Fourier experiments. Opt. Commun. **115**(5–6), 437–443 (1995)

[Men96] D. Mendlovic, R.G. Dorsch, A.W. Lohmann, Z. Zalevsky, C. Ferreira, Optical illustration of a varied fractional Fourier-transform order and the Radon-Wigner display. Appl. Opt. **35**(20), 3925–3929 (1996)

[Nei00] M.A.A. Neil, R. Juškaitis, M.J. Booth, T. Wilson, T. Tanaka, S. Kawata, Adaptive aberration correction in a two-photon microscope. J. Microsc. **200**(2), 105–108 (2000)

[Oht99] S. Ohtaki, N. Murao, M. Ogasawara, M. Iwasaki, The applications of a liquid crystal panel for the 15 Gbyte optical disk systems. Jpn. J. Appl. Phys. **38**(Part 1, No. 3B), 1744–1749 (1999)

[She91] M.H. Sher, S.J. Benerofe, J.F. Young, S.E. Harris, 2-Hz 109-nm mirrorless laser. J. Opt. Soc. Am. B **8**(1), 114–116 (1991)

[Woo94] J.C. Wood, D.T. Barry, Linear signal synthesis using the Radon-Wigner transform. IEEE Trans. Signal Process. **42**(8), 2105–2111 (1994)

[Wul06] K.D. Wulff, D.G. Cole, R.L. Clark, R. DiLeonardo, J. Leach, J. Cooper, G. Gibson, M.J. Padgett, Aberration correction in holographic optical tweezers. Opt. Express **14**(9), 4169–4174 (2006)

[Zha98] G. Yan Zhang, B.-Z.D. Ben-Yuan, G.-Z. Yang, Optical implementations of the Radon-Wigner display for one-dimensional signals. Opt. Lett. **23**(14), 1126–1128 (1998)

Chapter 3
Characterization of Beams Separable in Cartesian Coordinates

3.1 Introduction

As we have discussed in Chap. 1, the characterization of 2D beams is a complex problem requiring the acquisition and processing of huge volume of data. Any hypothesis about the beam spatial structure, and specially those that can be experimentally checked, has to be used in order to simplify this task. In this Chapter we consider beams that are separable in Cartesian coordinates, referred as *separable beams*, which are described by a MI that can be factorised into two functions, Γ_x and Γ_y, that depend on the x and y variables, respectively:

$$\Gamma\left(\mathbf{r}_1, \mathbf{r}_2\right) = \Gamma_x\left(x_1, x_2\right) \Gamma_y\left(y_1, y_2\right). \tag{3.1}$$

Examples of separable beams are all the HG modes, which have been presented in Sect. 1.1, and the partially coherent beams composed as incoherent superposition of HG modes for fixed index, i.e.

$$\Gamma\left(\mathbf{r}_1, \mathbf{r}_2\right) = \sum_n a_n \mathscr{H}_{m,n}\left(\mathbf{r}_1\right) \mathscr{H}_{m,n}\left(\mathbf{r}_2\right), \tag{3.2}$$

$$\Gamma\left(\mathbf{r}_1, \mathbf{r}_2\right) = \sum_m a_m \mathscr{H}_{m,n}\left(\mathbf{r}_1\right) \mathscr{H}_{m,n}\left(\mathbf{r}_2\right). \tag{3.3}$$

Partially coherent separable beams are obtained from GSMBs by modulation with a separable transmission function describing an aperture or a CGH, for example the beam considered in [Qiu05]. The resulting MI is defined as

$$\Gamma\left(\mathbf{r}_1, \mathbf{r}_2\right) = h\left(\mathbf{r}_1\right) h^*\left(\mathbf{r}_2\right) \exp\left[-2\pi \frac{\left(\mathbf{r}_1 - \mathbf{r}_2\right)^2}{w_c^2}\right] \exp\left[-\pi \frac{\mathbf{r}_1^2 + \mathbf{r}_2^2}{w^2}\right], \tag{3.4}$$

where $h\left(\mathbf{r}\right) = h_x\left(x\right) h_y\left(y\right)$ is the transmission function. Such beams can be generated employing an optical scheme similar to the one proposed in Chap. 5 or in

A. Cámara, *Optical Beam Characterization via Phase-Space Tomography*,
Springer Theses, DOI 10.1007/978-3-319-19980-1_3

Fig. 2.a of [Cám13a]. In this Chapter we exploit the symmetry of separable beams to simplify their analysis. In particular, we propose and experimentally demonstrate a custom phase-space tomography method that facilitate the characterization of separable beams. The technique is presented together with a verification procedure of separability of an a priori unknown beam.

3.2 Characterization Method

In order to introduce the simplified phase-space tomography method let us consider how the separability symmetry affects the WD and the fractional power spectra of the beam. On the one hand, the MI and the WD are related by a FT. Since the FT kernel is a separable function,

$$\exp\left(-\mathrm{i}2\pi\frac{\mathbf{r}\cdot\mathbf{p}}{\sigma^2}\right)=\exp\left(-\mathrm{i}2\pi\frac{xu}{\sigma^2}\right)\exp\left(-\mathrm{i}2\pi\frac{yv}{\sigma^2}\right), \tag{3.5}$$

the WD of a separable beam is also separable:

$$\begin{aligned}W(\mathbf{r},\mathbf{p})&=\frac{1}{\sigma^2}\int\mathrm{d}\mathbf{r}'\,\Gamma\left(\mathbf{r}+\frac{\mathbf{r}'}{2},\mathbf{r}-\frac{\mathbf{r}'}{2}\right)\exp\left(-\frac{\mathrm{i}2\pi}{\sigma^2}\mathbf{p}\cdot\mathbf{r}'\right)\\&=\frac{1}{\sigma}\int\mathrm{d}x'\,\Gamma_x\left(x+\frac{x'}{2},x-\frac{x'}{2}\right)\exp\left(-\mathrm{i}2\pi\frac{ux'}{\sigma^2}\right)\\&\quad\times\frac{1}{\sigma}\int\mathrm{d}y'\,\Gamma_y\left(y+\frac{y'}{2},y-\frac{y'}{2}\right)\exp\left(-\mathrm{i}2\pi\frac{vy'}{\sigma^2}\right)\\&=W_x(x,u)\,W_y(y,v)\,.\end{aligned} \tag{3.6}$$

Similarly, since the FRFT kernel is a function separable in Cartesian coordinates, c.f. Eq. (1.41), the fractional power spectra of separable beams are also separable:

$$\begin{aligned}S^{\gamma_x,\gamma_y}(\mathbf{r})&=\int\mathrm{d}\mathbf{r}_1\mathrm{d}\mathbf{r}_2\,\Gamma(\mathbf{r}_1,\mathbf{r}_2)\,K^{\gamma_x,\gamma_y}(\mathbf{r}_1,\mathbf{r})\left[K^{\gamma_x,\gamma_y}(\mathbf{r}_2,\mathbf{r})\right]^*\\&=\int\mathrm{d}x_1\mathrm{d}x_2\,\Gamma_x(x_1,x_2)\,K_x^{\gamma_x}(x_1,x)\left[K_x^{\gamma_x}(x_2,x)\right]^*\\&\quad\times\int\mathrm{d}y_1\mathrm{d}y_2\,\Gamma_y(y_1,y_2)\,K_y^{\gamma_y}(y_1,y)\left[K_y^{\gamma_y}(y_2,y)\right]^*\\&=S_x^{\gamma_x}(x)\,S_y^{\gamma_y}(y)\,.\end{aligned} \tag{3.7}$$

Notice that, as a consequence of Eq. (3.7), integrating S^{γ_x,γ_y} in the y or x direction yields a function that is proportional to the 1D projections of W_x or W_y, respectively,

$$\int\mathrm{d}y\,S^{\gamma_x,\gamma_y}(\mathbf{r})=S_x^{\gamma_x}(x)\int\mathrm{d}y\,S_y^{\gamma_y}(y)=A_y\left(\gamma_y\right)S_x^{\gamma_x}(x)\,, \tag{3.8}$$

$$\int \mathrm{d}x\ S^{\gamma_x,\gamma_y}(\mathbf{r}) = S_y^{\gamma_y}(y) \int \mathrm{d}x\ S_x^{\gamma_x}(x) = A_x(\gamma_x)\, S_y^{\gamma_y}(y)\,. \tag{3.9}$$

Furthermore, according to Parseval theorem, see Eq. (1.55), the $A_{x,y}$ functions do not depend on the FRFT angle, i.e. they are constants, and are equivalent to the power associated with each factor of the complex amplitude:

$$A_x(\gamma_x) = A_x = \int \mathrm{d}x\ \Gamma_x(x,x)\,, \tag{3.10}$$

$$A_y(\gamma_y) = A_y = \int \mathrm{d}y\ \Gamma_y(y,y)\,. \tag{3.11}$$

Observe that the separability symmetry decouples the beam information in the x and y coordinates. For example, while in a general case the coherence degree of the beam at two horizontally separated points, $\gamma\,[(x_1, y), (x_2, y)]$, depends on the vertical variable y, for a separable beam it does not. Therefore, a complete characterization of a separable beam can be achieved by reconstructing its WDs associated with each Cartesian direction.

At this point we introduce a simplified phase-space tomography method, valid for separable beams, which consists in the following steps:

1. Measure the antisymmetric fractional power spectra for FRFT angle, $\gamma_x = -\gamma_y = \gamma$, varying in a π-range interval.
2. Integrate along the y and x direction to obtain the normalised WD projections for the W_x and W_y functions, respectively:

$$S_x^{\gamma}(x) = \int \mathrm{d}y\ S^{\gamma,-\gamma}(\mathbf{r})\,, \tag{3.12}$$

$$S_y^{-\gamma}(y) = \int \mathrm{d}x\ S^{\gamma,-\gamma}(\mathbf{r})\,. \tag{3.13}$$

3. Verification of beam separability hypothesis, see Sect. 3.3.
4. Assemble the WD projections associated with each coordinate into the full-range RWTs corresponding to W_x and W_y.
5. Recover the WDs for each coordinate by applying a tomographic reconstruction algorithm to the full-range RWTs obtained in the previous step.

We underline that the use of additional information about the beam separability allows reducing drastically the number of required WD projection from N^2 to N. In addition, the method is easily adaptable to other sets of fractional power spectra, as long as both their FRFT angles, γ_x and γ_y, vary uniformly in a π-range interval, for example the symmetric FRFT. We have selected the antisymmetric set of fractional power spectra because there is a convenient optical system to register them. The method is experimentally demonstrated in the following Section, where the optical systems for test beam generation and fractional power spectra measurement are explained.

3.3 Separability Test

In most real-world situations we do not have access to the symmetries of the beam phase or coherence degree prior to its characterization. Therefore, we cannot anticipate whether an a priori unknown beam is suitable for this simplified phase-space tomography method. In order to overcome this limitation, we propose a *separability test* that checks if a beam is separable in Cartesian coordinates. Beams that pass the test can be analyzed using the suggested characterization method. To the best of our knowledge this is the first original treatment for a test of beams separable in Cartesian coordinates.

The separability test consists in checking that all the 2D WD projections satisfy the following relation:

$$\left[\int \mathrm{d}x\; S^{\gamma,-\gamma}\left(\mathbf{r}\right)\right]\left[\int \mathrm{d}y\; S^{\gamma,-\gamma}\left(\mathbf{r}\right)\right] = S^{\gamma,-\gamma}\left(\mathbf{r}\right)\int \mathrm{d}\mathbf{r}'\; S^{\gamma,-\gamma}\left(\mathbf{r}'\right). \tag{3.14}$$

The procedure is to obtain the antisymmetric fractional power spectra, $S^{\gamma,-\gamma}$, calculate the 1D fractional power spectra, S_x^{γ} and $S_y^{-\gamma}$, and apply Eq. (3.14). This relation is only satisfied for all WD projections when the beam is separable in Cartesian coordinates, as it is demonstrated in Sect. 3.7.

Since the separability test requires the beam antisymmetric fractional power spectra, these measurements can be used for further characterization of the beam. In the case that the beam pass the test, it can be fully characterized using the method suggested in this Chapter. Otherwise, the WD projections associated with the antisymmetric fractional power spectra can be used in a general characterization method. Either way, the measured data is profitable for the analysis of the beam.

3.4 Experimental Setups

In order to prove the feasibility of the proposed technique for the characterization of beams that are separable in Cartesian coordinates, we analyze a test signal: a $\mathscr{H}_{4,3}$ mode multiplied by a spherical chirp. The beam is described by its complex field amplitude,

$$f\left(\mathbf{r}\right) = \mathscr{H}_{4,3}\left(\mathbf{r}\right)\exp\left(-\mathrm{i}\frac{\pi r^2}{\lambda \mathrm{f_c}}\right), \tag{3.15}$$

where $w = 0.75$ mm is the beam waist, $\mathrm{f_c} = 2$ m is the chirp parameter, and $\lambda = 532$ nm is the wavelength of the light emitted by a Nd:YAG laser source. The intensity and phase distributions of the test beam are displayed in Fig. 3.1.

The test signal is generated following the same procedure of [Rod07b], whose optical system is displayed in Fig. 3.2. An input plane wave, which is obtained by the

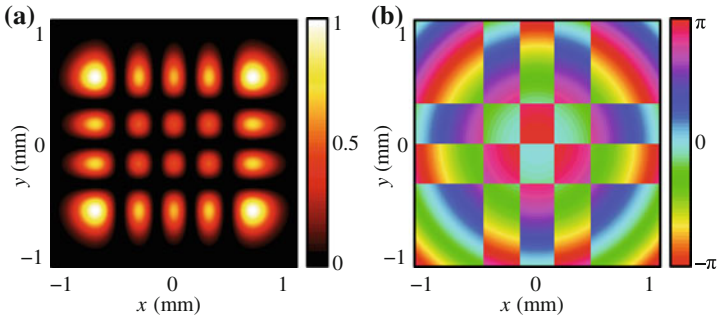

Fig. 3.1 **a** Intensity and **b** phase distributions of the test signal: a $\mathscr{H}_{4,3}$ beam with waist $w = 0.75\,\text{mm}$ and $\lambda = 532\,\text{nm}$ multiplied by a spherical chirp of parameter $f_c = 2\,\text{mm}$

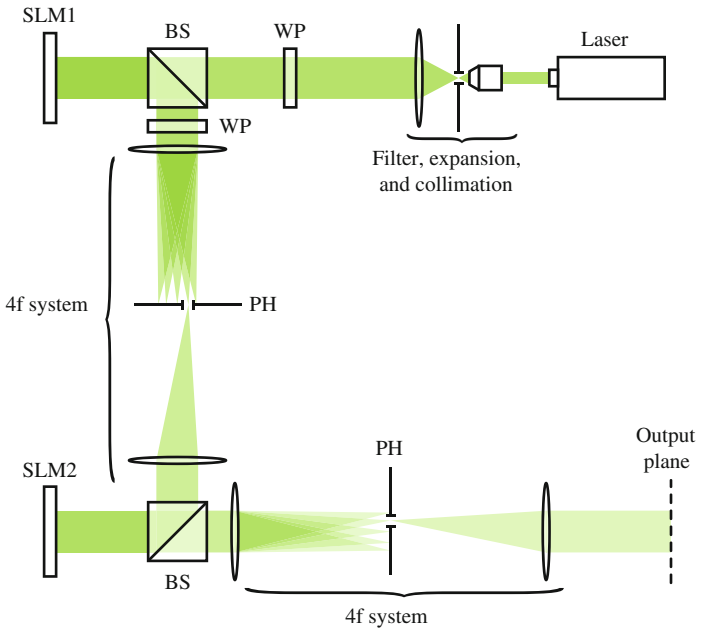

Fig. 3.2 Optical system used for the generation of the test signal. Two SLMs, one working in amplitude-only modulation and the other in phase-only modulation, implement the intensity and phase distributions of the beam, respectively. Two 4f telescopes image the first SLM into the second, and the second SLM into the output plane. A pinhole filters the spurious terms that appear in the Fourier plane of both telescopes due to the pixelated nature of the SLMs

expanded, filtered, and collimated Gaussian beam of a laser cavity, gets its intensity distribution modulated by the amplitude-only SLM, SLM1. The resulting beam is then imaged into the second SLM, SLM2, by a 4f telescope. The spurious copies of the beam that appear in the Fourier plane of the telescope due to the pixelated nature of the SLM are filtered using a pinhole, PH. SLM2 works in phase-only regime

and is responsible for the generation of the beam phase distribution. A second 4f telescope filters the new spurious terms due to the second SLM and images the resulting beam into the output plane of the system. Half-wave plates, WP, modify the beam polarisation to make the SLMs work in amplitude-only and phase-only regimes. In the end, the expected beam displayed in Fig. 3.2 is obtained using the same SLMs as in Chap. 2.

On the other hand, an optical system that performs the antisymmetric FRFT is required to measure the beam fractional power spectra. Since the antisymmetric FRFT is related to the Gyrator transform by a 45° rotation, see Eq. 1.39, the optical system suggested in [Rod07b] for Gyrator transform is easily modified for the experimental realisation of the antisymmetric FRFT. The setup, illustrated in Fig. 3.3a, consists in two generalized lenses, L_1 and L_2, separated by a fixed distance z. Each generalized lens is composed by a pair of cylindrical thin-lenses of the same focal length in contact. While the focal length of the cylindrical lenses of L_1 is z, the focal length of L_2 lenses is $z/2$. At the output plane, separated a distance z from L_2, a CCD camera is placed to register the antisymmetric fractional power spectra. The length parameter of the system is $\sigma = \sqrt{\lambda z}$.

In order to tune the FRFT angle γ the cylindrical lenses forming L_1 and L_2 have to be rotated in the xy plane, refer to Fig. 3.3b for a scheme of a generalized lens, where the phase modulation direction of the composing cylindrical lenses are represented. The angle between the x axis and the phase modulation direction of the ith cylindrical lens of the jth generalized lens is denoted by $\theta_{j,i}$. For the sake of simplicity, instead of defining the FRFT angle, γ, in terms of $\theta_{j,i}$, we used the auxiliary angles, φ_1 and φ_2,

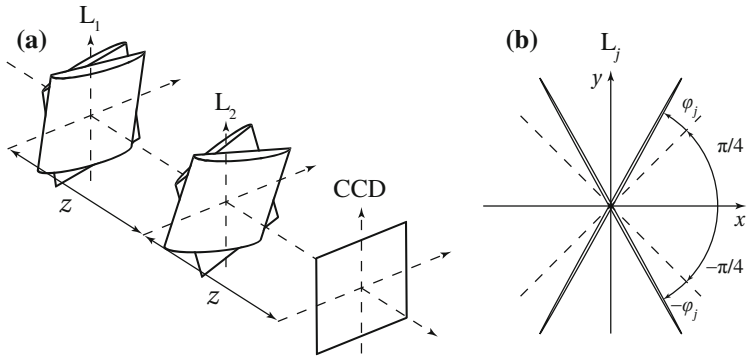

Fig. 3.3 **a** Optical system used for the measurement of the antisymmetric fractional power spectra. The system is composed by two generalized lenses, L_1 and L_2, each one consisting in a pair of cylindrical lenses in contact, that are separated by a fixed distance z. The focal length of the cylindrical lenses of L_1 is z, while for L_2 is $z/2$. The antisymmetrical fractional power spectra is measured at a distance z from L_2, where a CCD camera is placed. **b** Scheme illustrating the angle convention for the generalized lenses

$$\theta_{j,1} = \varphi_j + \pi/4, \tag{3.16}$$

$$\theta_{j,2} = -\varphi_j - \pi/4. \tag{3.17}$$

See Fig. 3.3b for an illustration of the relations between $\theta_{j,i}$ and φ_j angles. The FRFT angle γ is achieved by imposing the following constrains in φ_1 and φ_2:

$$\sin(2\varphi_1) = \frac{1}{2}\cot(\gamma/2), \tag{3.18}$$

$$\sin(2\varphi_2) = \sin\gamma. \tag{3.19}$$

These relations can be proved, similarly to the RWD case of Chap. 2, by multiplying the ray transformation matrices describing the corresponding elements. In the end, any antisymmetric fractional power spectra for FRFT angle γ contained in $[\pi/2, 3\pi/2]$ can be measured using the proposed optical system.

For the experiments we set $z = 0.5$ m and used light from a Nd:YAG laser source ($\lambda = 532$ nm), which produces an optical system with length parameter $\sigma = 0.52$ mm. At the output plane, a Imaging Source DMK-41BF02 CCD camera of resolution 1280×960 and pixel pitch $4.65\,\mu$m recorded the required antisymmetric fractional power spectra.

3.5 Experimental Results

As explained in the Sect. 3.2, each antisymmetric fractional power spectra is integrated in the x and y coordinates, obtaining two 1D WD projections associated, respectively, with the y or x component of the original signal. Full-range RWTs are assembled from 45 1D projections. The experimental and simulated RWTs are compared in Fig. 3.4. Notice that simulated RWTs are obtained applying the reconstruction process to numerically generated antisymmetric fractional power spectra. Finally, the WD for the x and y components of the beam are reconstructed applying the filtered back-projection algorithm to the RWT. The experimental and simulated WDs are displayed in Fig. 3.5.

The experimental RWTs displayed in Fig. 3.4 show that the test signal is not an eigenfunction of the optical system performing the antisymmetric FRFT. Despite of the similar form of the 1D WD projections associated with each coordinate, the distinct scale is a manifestation of the difference between the optical system length parameter, σ, and the signal size, w, and the spherical phase modulation associated with $\mathrm{f_c}$. Only in the case when $w = \sigma$ and $\mathrm{f_c} = 0$ all the WD projections have the same scale, since this HG mode is an eigenfunction of the optical system.

These two effects—the inequality between σ and w, and the spherical phase modulation associated with $\mathrm{f_c}$—are also noticeable in the WDs reconstructed from the RWTs. In particular, the eccentricity of the elliptical rings of Fig. 3.5 is related to the different scales of the optical system and the signal, and the chirp parameter.

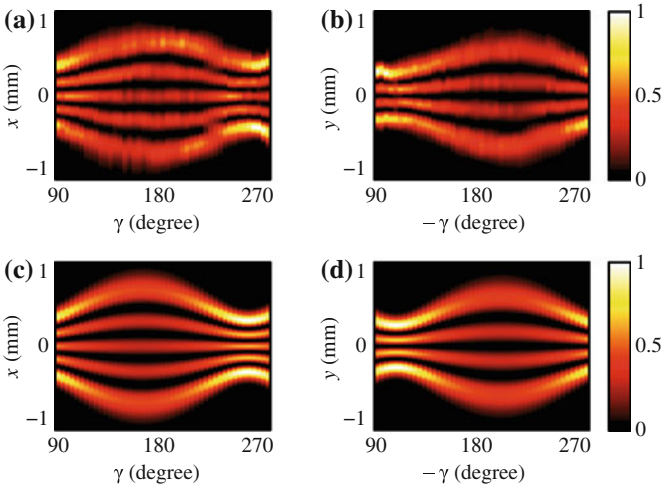

Fig. 3.4 Experimental full-range RWTs for **a** x and **b** y components of the $\mathscr{H}_{4,3}$ beam with $w = 0.75\,\text{mm}$ and $\text{f}_\text{c} = 2\,\text{m}$ assembled from 45 antisymmetrical fractional power spectra. Simulated RWTs for **c** x and **d** y components of the signal assembled from numerically obtained antisymmetrical fractional power spectra

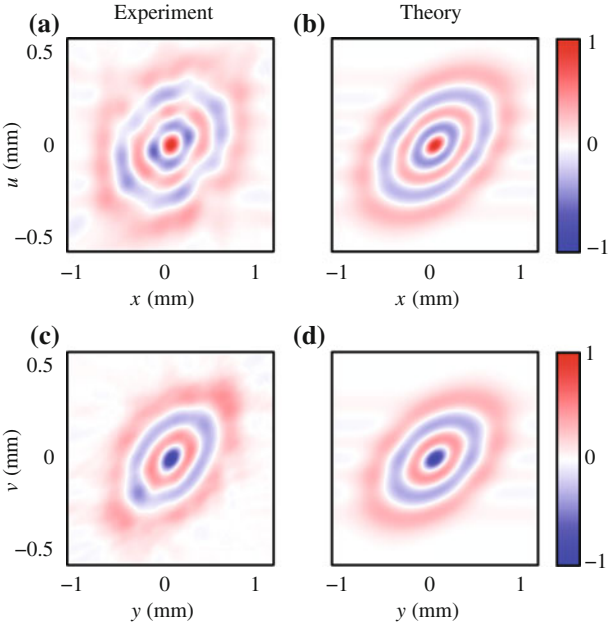

Fig. 3.5 Experimental WDs for **a** x and **c** y components of the $\mathscr{H}_{4,3}$ beam obtained from the full-range RWTs displayed in Fig. 3.4. Simulated WDs for **b** x and **d** y components of the signal recovered from the simulated RWTs

The WD negative values, represented by blue colours in Fig. 3.5, are associated with the high coherence of the generated beam. Finally, recall that, according to Eq. (3.6), from the WDs corresponding to each 1D component of the signal, the complete 4D WD can be obtained. As well as in the case of 1D signals, increasing the number of projections improves the quality of the WD reconstruction.

While the beam in the considered example is coherent, the method is equally suited for the recovery of the WD of partially coherent beams separable in Cartesian coordinates, as we have theoretically predicted in Sect. 3.2.

3.6 Conclusions

As it has been demonstrated in the experimental results of Sect. 3.5, the proposed technique allows recovering the full-range RWT and WD of a 2D beam separable in Cartesian coordinates. This method is convenient for several reasons:

1. The required measurements, the beam antisymmetric fractional power spectra, can be registered using an optical system with conventional elements—cylindrical lenses and a CCD camera. Moreover, as we will see in Chap. 4, the same projections, and therefore the same setup, can be used for the analysis of rotationally symmetric beams.
2. The volume of data is considerably smaller than for the general case, which increases the speed of the data processing step.
3. The separability of the WDs and the RWTs allow characterizing each signal component independently, which ease the analysis of the recovered information.

The method major drawback is that it only works for separable beams. The procedure proposed in Sect. 3.3 allows checking if an a priori unknown beam is separable in Cartesian coordinates. Beams that pass the separability test can be characterized using the method suggested in this Chapter.

Most of these results are published in the article of [Cám09a], and in the book chapter of [Ali11]. In addition, they were presented at the congresses [Cám08, Ali09, Cám09b, Cám10a, Ali12c].

Appendices

3.7 Demonstration of the Separability Test

The separability test affirms that a beam for which all its fractional power spectra satisfy

$$\left[\int \mathrm{d}x\; S^{\gamma,-\gamma}\left(\mathbf{r}\right)\right]\left[\int \mathrm{d}y\; S^{\gamma,-\gamma}\left(\mathbf{r}\right)\right] = S^{\gamma,-\gamma}\left(\mathbf{r}\right)\int \mathrm{d}\mathbf{r}'\; S^{\gamma,-\gamma}\left(\mathbf{r}'\right). \tag{3.20}$$

must be separable in Cartesian coordinates. Introducing the FRFT kernel in both left- and right-hand sides of Eq. (3.20) we obtain that:

$$\begin{aligned}\text{LHS}\,(\mathbf{r}) &\equiv \left[\int \mathrm{d}x\; S^{\gamma,-\gamma}\,(\mathbf{r})\right]\left[\int \mathrm{d}y\; S^{\gamma,-\gamma}\,(\mathbf{r})\right] \\ &= c_\gamma \int \mathrm{d}\mathbf{r}_1 \mathrm{d}\mathbf{r}_2\; \exp\left\{\frac{\mathrm{i}\pi}{\sigma^2 \sin\gamma}\left[\left(x_1^2 - x_2^2\right)\cos\gamma - 2\,(x_1 - x_2)\,x\right]\right\} \\ &\quad \times \exp\left\{-\frac{\mathrm{i}\pi}{\sigma^2 \sin\gamma}\left[\left(y_1^2 - y_2^2\right)\cos\gamma - 2\,(y_1 - y_2)\,y\right]\right\} \\ &\quad \times \int \mathrm{d}x' \Gamma\left(x', y_1, x', y_2\right) \int \mathrm{d}y'\; \Gamma\left(x_1, y', x_2, y'\right) \end{aligned} \tag{3.21}$$

and

$$\begin{aligned}\text{RHS}\,(\mathbf{r}) &\equiv S^{\gamma,-\gamma}\,(\mathbf{r}) \int \mathrm{d}\mathbf{r}'\; S^{\gamma,-\gamma}\left(\mathbf{r}'\right) \\ &= c_\gamma \int \mathrm{d}\mathbf{r}_1 \mathrm{d}\mathbf{r}_2\; \exp\left\{\frac{\mathrm{i}\pi}{\sigma^2 \sin\gamma}\left[\left(x_1^2 - x_2^2\right)\cos\gamma - 2\,(x_1 - x_2)\,x\right]\right\} \\ &\quad \times \exp\left\{-\frac{\mathrm{i}\pi}{\sigma^2 \sin\gamma}\left[\left(y_1^2 - y_2^2\right)\cos\gamma - 2\,(y_1 - y_2)\,y\right]\right\} \\ &\quad \times \Gamma\,(x_1, y_1, x_2, y_2) \int \mathrm{d}\mathbf{r}'\; \Gamma\left(\mathbf{r}', \mathbf{r}'\right), \end{aligned} \tag{3.22}$$

where c_γ is a transformation constant that depends on γ and the Parseval theorem has been applied to relate

$$\int \mathrm{d}\mathbf{r}'\; S^{\gamma,-\gamma}\,(\mathbf{r}) = \int \mathrm{d}\mathbf{r}'\; S^{0,0}\left(\mathbf{r}'\right) = \int \mathrm{d}\mathbf{r}'\; \Gamma\left(\mathbf{r}', \mathbf{r}'\right). \tag{3.23}$$

As this condition must be held for all angles γ, it is equivalent to

$$\begin{aligned}&\int \mathrm{d}x' \Gamma\left(x', y_1, x', y_2\right) \int \mathrm{d}y'\; \Gamma\left(x_1, y', x_2, y'\right) \\ &\qquad = \Gamma\,(x_1, y_1, x_2, y_2) \int \mathrm{d}\mathbf{r}'\; \Gamma\left(\mathbf{r}', \mathbf{r}'\right). \end{aligned} \tag{3.24}$$

The essence of the demonstration is to deduce that any beam that satisfies Eq. (3.24) must be separable.

Consider a beam described by the MI $\Gamma\,(\mathbf{r}_1, \mathbf{r}_2)$ which is **not** separable, but satisfies Eq. (3.24). Consider the following two functions obtained via

$$A\,(x_1, x_2) = \int \mathrm{d}y'\; \Gamma\left(x_1, y', x_2, y'\right), \tag{3.25}$$

$$B\left(y_1, y_2\right) = \int \mathrm{d}x' \, \Gamma\left(x', y_1, x', y_2\right). \tag{3.26}$$

Thus, Eq. (3.24) can be rewritten as

$$\begin{aligned} A\left(x_1, x_2\right) B\left(y_1, y_2\right) &= \Gamma\left(\mathbf{r}_1, \mathbf{r}_2\right) \int \mathrm{d}x' A\left(x', x'\right) \\ &= \Gamma\left(\mathbf{r}_1, \mathbf{r}_2\right) \int \mathrm{d}y' B\left(y', y'\right). \end{aligned} \tag{3.27}$$

Notice that the power of the beam can be expressed as

$$\begin{aligned} P &= \int \mathrm{d}\mathbf{r}' \, \Gamma\left(\mathbf{r}', \mathbf{r}'\right) = \int \mathrm{d}x' \, A\left(x', x'\right) = \int \mathrm{d}y' \, B\left(y', y'\right) \\ &= \sqrt{\int \mathrm{d}x' \, A\left(x', x'\right)} \sqrt{\int \mathrm{d}y' \, B\left(y', y'\right)}. \end{aligned} \tag{3.28}$$

Dividing both sides of Eq. (3.27) by the energy we obtain

$$\frac{A\left(x_1, x_2\right)}{\sqrt{\int \mathrm{d}x' \, A\left(x', x'\right)}} \frac{B\left(y_1, y_2\right)}{\sqrt{\int \mathrm{d}y' \, B\left(y', y'\right)}} = \Gamma\left(\mathbf{r}_1, \mathbf{r}_2\right). \tag{3.29}$$

This is the separability condition of our starting beam, which was considered not separable. Therefore, by *reductio ad absurdum*, a beam satisfying Eq. (3.24), or Eq. (3.20) for every γ, has to be separable.

References

[Ali09] T. Alieva, A. Cámara, J.A. Rodrigo, M.L. Calvo, Experimental reconstruction of Wigner distribution. In *OSA Annual Meeting Proceedings*, 2009

[Ali11] T. Alieva, A. Cámara, J.A. Rodrigo, M.L. Calvo, in *Optical and Digital Image Processing*, chapter Phase-space tomography of optical beams. (Wiley-VCH, New york, 2011)

[Ali12c] T. Alieva, A. Cámara, J.A. Rodrigo, M.L. Calvo, Projections of Wigner distribution for optical beam characterization. In *PIERS Proceedings of Progress in Electromagnetic Research Symposium* (2012)

[Cám08] A. Cámara, T. Alieva, Phase-space tomography for separable optical fields. In *ICO Proceedings* (2008)

[Cám09a] A. Cámara, T. Alieva, J.A. Rodrigo, M.L. Calvo, Phase space tomography reconstruction of the Wigner distribution for optical beams separable in cartesian coordinates. J. Opt. Soc. Am. A **26**(6), 1301–1306 (2009)

[Cám09b] A. Cámara, T. Alieva, J.A. Rodrigo, M.L. Calvo, Reconstrucción de la distribución de Wigner mediante tomografía en el espacio de fases. In *IX Reunión Nacional de Óptica*, (2009)

[Cám10a] A. Cámara, T. Alieva, J.A. Rodrigo, M.L. Calvo. Beam characterization via Wigner distribution projections. In *4th Tematic PRISMA Meeting*, (2010)

[Cám13a] A. Cámara, Jos A. Rodrigo, T. Alieva, Optical coherenscopy based on phase-space tomography. Opt. Express **21**(11), 13169–13183 (2013)
[Qiu05] Y. Qiu, H. Guo, Zhaoxi Chen, Paraxial propagation of partially coherent Hermite-Gauss beams. Opt. Commun. **245**(16), 21–26 (2005)
[Rod07b] J. Rodrigo, T. Alieva, María L. Calvo, Gyrator transform: properties and applications. Opt. Express **15**(5), 2190 (2007)

Chapter 4
Rotationally Symmetric Beams

4.1 Introduction

A RSB is characterized by a MI that is invariant respect any rotation at the plane transverse to the beam propagation. Its MI satisfies

$$\Gamma(\mathbf{r}_1, \mathbf{r}_2) = \Gamma[\mathbf{M}(\theta_0)\,\mathbf{r}_1, \mathbf{M}(\theta_0)\,\mathbf{r}_2] \tag{4.1}$$

for any angle θ_0 of the 2D rotation matrix

$$\mathbf{M}(\theta_0) = \begin{bmatrix} \cos\theta_0 & -\sin\theta_0 \\ \sin\theta_0 & \cos\theta_0 \end{bmatrix}. \tag{4.2}$$

Although it is not a property exclusive to RSBs, all RSBs present an intensity distribution that is rotationally invariant, i.e. $I(\mathbf{r}) = I(r)$. Optical vortices—a subclass of RSBs—additionally transfer orbital angular momentum (OAM) to the medium where they propagate through. This characteristic is specially attractive for optical trapping where it is used to exert torques to the micro-particles being manipulated [Gri03]. In addition, optical vortices are used in free-space communication schemes of improved stability [Ric03], security [Gib04], and transmission rate [Wan12].

Coherent optical vortices are arguably the widest class of RSB used in real-world applications. They are constituted by a rotationally invariant intensity profile and a phase distribution of the form $\exp(il\varphi)$ where φ is the azimuthal angle, $\varphi = \arctan(y/x)$, and l is an integer defining the amount of OAM transferred to the medium—usually known as topological charge.

Partially coherent RSBs, however, are less recurrent in the literature due to the more complicated processes involved in its synthesis and analysis. A method to generate them is the incoherent addition of LG beams as proposed in [Gor98, Pon01]:

$$\Gamma_{\mathrm{RSB}}(\mathbf{r}_1, \mathbf{r}_2) = \sum_p a_p \mathscr{L}_p^l(\mathbf{r}_1)\left[\mathscr{L}_p^l(\mathbf{r}_2)\right]^*. \tag{4.3}$$

A. Cámara, *Optical Beam Characterization via Phase-Space Tomography*,
Springer Theses, DOI 10.1007/978-3-319-19980-1_4

This allows generating a large variety of partially coherent beams at the expense of a complex experimental setup. An alternative approach is to modulate a GSMB with a hologram encoding a phase vortex. The partially coherent beam can be generated using a rotating ground glass diffuser and the hologram can be computer-generated into a SLM [Ali13]. This reduces the setup complexity considerably since the incoherent sum operation is not required. However, the variety of beams that can be generated is more limited. These procedures will be used to generate the experimental signals of Chap. 5 and are explained in detail in [Cám13a].

As in the case of the other symmetries studied in Chaps. 2 and 3, the coherence analysis of a RSBs can be significantly simplified. In this chapter we present a phase-space tomography method specially designed for RSBs. It allows reconstructing the beam AF and thus its MI, see Eq. (1.15), which provides a complete coherence picture of the beam. In order to validate the method we simulate its application to two RSBs with different coherence states and compare the results with the theoretical expectations. The chapter concludes proving the method feasibility by comparing the AF recovered from an experimental beam with the theoretical expectation.

4.2 Phase-Space Tomography for RSB

We have already mentioned that the MI of a RSB is invariant respect to a coordinate rotation, recall Eq. (4.1). This symmetry also affects the other representations of the beam. For instance, taking the definitions of WD and AF, see Eqs. (1.12) and (1.15), it is easy to find that:

$$W(\mathbf{r}, \mathbf{p}) = W(\mathbf{Mr}, \mathbf{Mp}), \tag{4.4}$$

$$A(\mathbf{r}, \mathbf{p}) = A(\mathbf{Mr}, \mathbf{Mp}). \tag{4.5}$$

Essentially, the symmetry is indicating a redundancy of information in the beam representation: we no longer need to vary all four coordinates of the beam representation to fully characterize it. This becomes more evident when we express the beam MI in polar coordinates, where the symmetry is naturally expressed. The polar coordinates are defined by $(r_{1,2}, \theta_{1,2})$ associated with the change of variables

$$x_{1,2} = r_{1,2} \cos\theta_{1,2}, \tag{4.6}$$

$$y_{1,2} = r_{1,2} \sin\theta_{1,2}. \tag{4.7}$$

The beam MI is written respect to this coordinate system as:

$$\widetilde{\Gamma}(r_1, \theta_1, r_2, \theta_2) = \widetilde{\Gamma}(r_1, \theta_1 + \theta_0, r_2, \theta_2 + \theta_0) = \widetilde{\Gamma}(r_1, \theta_1 - \theta_2, r_2, 0). \tag{4.8}$$

From Eq. (4.8) it is evident that, instead of the conventional four variables associated with the MI of a general beam, the MI of a RSB beam depends on only three variables:

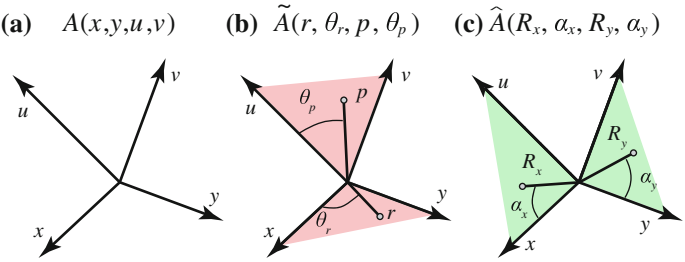

Fig. 4.1 Illustration of the different coordinate systems used for the AF characterization of RSBs. **a** Cartesian, **b** tilde polar, and **c** hat polar coordinate systems

the two radial lengths, r_1 and r_2, and the angular difference $\theta_1 - \theta_2$. Therefore, the data that needs to be acquired and processed to characterize the beam is also reduced when comparing with a general beam.

Since the FRFT is the basis of the PST method, we have to understand how the rotation symmetry affects this operation. Just as the rotation symmetry is better expressed in polar than in Cartesian coordinates, the FRFT operation is best described in another polar coordinate system associated with the variables $(R_{x,y}, \alpha_{x,y})$. While R_x and α_x represent polar coordinates in the plane xu, R_y and α_y represent polar coordinates in the plane yv. For the sake of future simplification we consider that $R_{x,y}$ can take negative values and, consequently, $\alpha_{x,y}$ are contained in a π-range interval.

The three coordinate systems introduced to better explain the method are illustrated in Fig. 4.1. The following equations allow relating one to each other:

$$x = r\cos\theta_r = R_x\cos\alpha_x, \qquad y = r\sin\theta_r = R_y\cos\alpha_y, \tag{4.9}$$

$$u = p\cos\theta_p = R_x\sin\alpha_x, \qquad v = p\sin\theta_p = R_y\sin\alpha_y. \tag{4.10}$$

In order to indicate which coordinate system each function is referred to, we introduce a new notation.

1. The original Cartesian coordinate system is associated with the normal notation of AF: A $(\mathbf{r}, \mathbf{p})$.
2. The polar coordinate system in the xy and uv planes is associated with the *tilde* notation: $\widetilde{A}\left(r, \theta_r, p, \theta_p\right)$.
3. The polar coordinate system in the xu and yv planes is associated with the *hat* notation: $\widehat{A}\left(R_x, \alpha_x, R_y, \alpha_y\right)$.

Each coordinate system will aid in a specific task. The Cartesian coordinates are preferred to transform the beam MI into its AF and vice-versa, since both representations are related by a 2D FT. The tilde coordinates, $\widetilde{A}$, are best used to express the condition of rotationally symmetry in the MI, WD, and AF, see Eq. (4.8). The hat

coordinates, $\widehat{A}$, are optimal for expressing the phase-space rotation associated with the FRFT:

$$\widehat{A}\left(R_x, \alpha_x, R_y, \alpha_y\right) \underset{\mathfrak{F}^{\gamma_x,\gamma_y}}{\longmapsto} \widehat{A}\left(R_x, \alpha_x - \gamma_x, R_y, \alpha_y - \gamma_y\right), \tag{4.11}$$

where the left- and right-hand side of Eq. (4.11) represent, respectively, the AF of the original beam and the one transformed by the FRFT with parameters γ_x and γ_y.

Our PST method for RSBs is based in the reconstruction of the beam AF from a reduced number of intensity measurements. First consider the following relation between the beam intensity distribution with its AF [Ali00]:

$$\begin{aligned}\widehat{A}\left(R_x, \pi/2, R_y, \pi/2\right) &= A\left(\mathbf{0}, \mathbf{p}\right) \\ &= \frac{1}{\sigma^2}\int \mathrm{d}\mathbf{r}'\, \Gamma\left(\mathbf{r}', \mathbf{r}'\right) \exp\left(-\mathrm{i}2\pi \frac{x' R_x + y' R_y}{\sigma^2}\right).\end{aligned} \tag{4.12}$$

Equivalent relations can be found for the rest of fractional power spectra applying Eq. (4.11). In fact, the fractional power spectrum for angles $\gamma_{x,y}$ is associated with the hat AF for fixed $\alpha_{x,y} = \pi/2 - \gamma_{x,y}$ via

$$\widehat{A}\left(R_x, \alpha_x, R_y, \alpha_y\right) = \frac{1}{\sigma^2}\int \mathrm{d}\mathbf{r}'\, S^{\gamma_x,\gamma_y}\left(\mathbf{r}'\right) \exp\left(-\mathrm{i}2\pi \frac{x' R_x + y' R_y}{\sigma^2}\right), \tag{4.13}$$

It indicates that the FT of the beam intensity distribution is associated with the AF *radial section* corresponding to fixing the angles α_x and α_y. Therefore, the beam AF can be obtained from a set of its fractional power spectra where the angles $\gamma_{x,y}$ vary in a π-range interval.

This scheme is not fundamentally different from the original PST method: a certain set of fractional power spectra is measured and processed to obtain a beam representation, in this case the beam AF. Although the method is valid for any beam in general, it still can be significantly simplified for the analysis of RSBs due to the AF symmetry (it only depends on three variables). As a consequence:

1. We only need to measure the antisymmetrical fractional power spectra.
2. The antisymmetric angle, $\gamma = \gamma_x = -\gamma_y$, only needs to vary in a $\pi/2$-range interval.

This allows reducing the number of required projections from N^2 for the general case to $N/2$ projections for RSBs without affecting the sampling rate in the phase space. The complete demonstration of this simplification is presented in Sect. 4.6.

As a matter of introduction to the demonstration consider obtaining the AF value at the phase space point expressed in tilde polar coordinates as $(r_0, \theta_{r0}, p_0, \theta_{p0})$. Leaving apart the discrete nature of any set of measurements, the AF value at that point can always be extracted from a complete set of antisymmetrical fractional power spectra. In particular, it is associated with the AF radial section extracted from the antisymmetric fractional power spectra for angle γ_0 such that $|\tan\gamma_0| = r_0/p_0$.

The coordinates of the AF radial section are:

$$R_x = \left(r_0^2 + p_0^2\right)^{1/2} \cos\left[\frac{1}{2}\left(\theta_{p0} - \theta_{r0}\right)\right], \tag{4.14}$$

$$R_y = \left(r_0^2 + p_0^2\right)^{1/2} \sin\left[\frac{1}{2}\left(\theta_{p0} - \theta_{r0}\right)\right]. \tag{4.15}$$

The calculation of the beam coherence relation via Eq. (1.18) through a FT, see Eq. (4.13), requires the AF to be expressed in Cartesian coordinates, i.e. as *plane sections* $A\left(\mathbf{r}_0, \mathbf{p}\right)$ with fixed $\mathbf{r}_0$. Hence, the radial sections of the AF have to be further processed into the AF plane sections in order to recover the beam MI. The relation between the radial and plane sections of the AF is given by

$$\begin{aligned}
&\widetilde{A}\left(r_0, \theta_{r0}, p, \theta_p\right) \\
&\quad = \widehat{A}\left\{\sqrt{r_0^2 + p^2}\cos\left[\frac{1}{2}\left(\theta_p - \theta_{r0}\right)\right], \pi/2 - \arctan\frac{r_0}{p},\right. \\
&\qquad \left.\sqrt{r_0^2 + p^2}\sin\left[\frac{1}{2}\left(\theta_p - \theta_{r0}\right)\right], \pi/2 + \arctan\frac{r_0}{p}\right\},
\end{aligned} \tag{4.16}$$

or inversely,

$$\begin{aligned}
&\widehat{A}\left(R\cos\theta_R, \pi/2 - \gamma, R\sin\theta_R, \pi/2 + \gamma\right) \\
&\qquad = \widetilde{A}\left(r_0, \theta_{r0}, R\left|\cos\gamma\right|, 2\theta_R + \theta_{r0}\right).
\end{aligned} \tag{4.17}$$

Equations (4.14) and (4.15) have been used to derive these results. Although the analytical relation between the planar and radial sections is not evident, they have a rather direct interpretation in geometric terms. In fact, Eq. (4.16) establishes an equivalence relation between:

- the values at the circle of radius p associated with azimuth θ_p corresponding to the plane section $\mathbf{r}_0$, and
- the values at the circle of radius $\sqrt{r_0^2 + p^2}$ associated with azimuth $(\theta_p - \theta_{r0})/2$ corresponding to the radial section $\gamma = \arctan r_0/p$.

Analogously, Eq. (4.17) establishes a reciprocal relation between:

- the values at the circle of radius $R = \sqrt{R_x^2 + R_y^2}$ associated with azimuth θ_R corresponding to the radial section γ, and
- the values at the circle of radius $R|\cos\gamma|$ associated with azimuth $2\theta_R + \theta_{r0}$ corresponding to the plane section $\mathbf{r}_0 = (r_0, \theta_{r0})$ with $r_0 = R|\sin\gamma|$ and θ_{r0}.

These *circle relations* are illustrated in Fig. 4.2 in terms of the plane section reference point, $\mathbf{r}_0$, and the antisymmetrical fractional power spectra angle, γ.

From an analytical point of view, the transformation from radial to plane sections is straightforward since there is a one-to-one relation between points. From a numerical

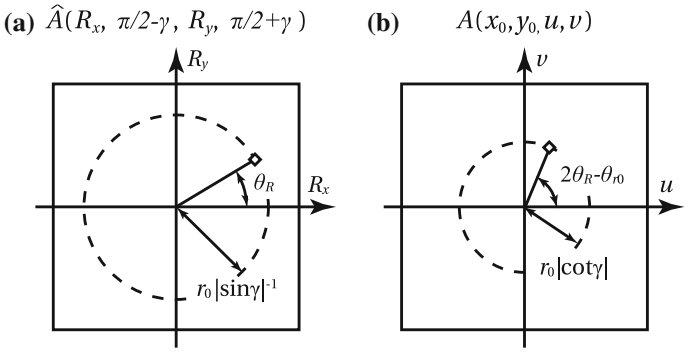

Fig. 4.2 Illustration of the circle relations between the radial and the plane sections of the AF of a RSB beam. They address the reconstruction of the plane section associated with the reference point $\mathbf{r}_0 = [x_0, y_0]^T$, which in polar coordinates is $r_0 = (x_0^2 + y_0^2)^{1/2}$ and $\theta_{r0} = \arctan y_0/x_0$. **a** The point in the circle of radius $r_0/|\sin\gamma|$ and azimuth θ_R corresponding to the radial section associated with the FRFT angle γ is mapped into, **b** the point in the circle of radius $r_0|\cot\gamma|$ and azimuth $2\theta_R - \theta_{r0}$ of the plane section

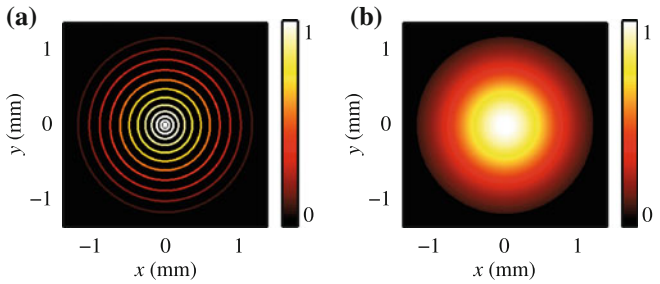

Fig. 4.3 **a** Example of a Gaussian AF plane section obtained using a finite number of antisymmetrical fractional power spectra. Black values are missing from the reconstruction. **b** Result after linear interpolation of the missing values

point of view, however, the transformation presents a challenge. We only have access to a finite number of antisymmetric power spectra and, hence, of AF radial sections. In addition, in order to assemble a plane section of the AF we need to extract the values in circles of the radial section. The radius of those circles do not change linearly with the FRFT angle, but as $|\cos\gamma|$. Following the procedure without paying attention to these considerations ends up with plane sections with missing values. This problem is illustrated in Fig. 4.3a where a plane section has been assembled using 25 antisymmetric fractional power spectra for equidistant angles γ. The values in black are missing from the reconstruction. As long as we are under the Nyquist limit [Goo05] we can interpolate the missing values, see Fig. 4.3b.

The following is a summary of the proposed procedure to obtain the MI of a RSB from the complete set of its antisymmetrical fractional power spectra:

1. Measure the beam antisymmetrical fractional power spectra for γ varying in a $\pi/2$-range interval, using for example the optical system described in Sect. 3.4.
2. Perform the FT to these antisymmetrical fractional power spectra to obtain the radial sections of the AF.
3. For every value of the antisymmetrical angle γ:
   (a) Extract the values associated the circle of radius R from the radial section.
   (b) Rescale the circle radius from R to $R|\cos\gamma|$.
   (c) Transform the circle azimuth from θ_R to $2\theta_R + \theta_{r0}$.
   (d) Assemble the resulting circle into the AF plane section.
4. Perform the FT to the plane section to obtain the MI, see Eq. (1.18).

In the next section we validate the method by simulating the characterization of two RSBs with different coherence states but the same intensity distribution.

4.3 Simulations

Consider the coherent LG mode $\mathscr{L}_2^2$ and the partially coherent RSB constructed as the incoherent sum of $\mathscr{L}_2^2$ and $\mathscr{L}_2^{-2}$. Their MIs are written as:

$$\begin{aligned}\Gamma_{\mathscr{L}_2^2}(\mathbf{r}_1,\mathbf{r}_2) &= \mathscr{L}_2^2(\mathbf{r}_1)\left[\mathscr{L}_2^2(\mathbf{r}_2)\right]^* \\ &= \left|\mathscr{L}_2^2(\mathbf{r}_1)\,\mathscr{L}_2^2(\mathbf{r}_2)\right| \exp\left[\mathrm{i}2\pi\,(\theta_1-\theta_2)\right], \qquad (4.18)\\ \Gamma_\Sigma(\mathbf{r}_1,\mathbf{r}_2) &= \frac{1}{2}\left\{\mathscr{L}_2^2(\mathbf{r}_1)\left[\mathscr{L}_2^2(\mathbf{r}_2)\right]^* + \mathscr{L}_2^{-2}(\mathbf{r}_1)\left[\mathscr{L}_2^{-2}(\mathbf{r}_2)\right]^*\right\} \\ &= \left|\mathscr{L}_2^2(\mathbf{r}_1)\,\mathscr{L}_2^2(\mathbf{r}_2)\right| \cos\left[2\,(\theta_1-\theta_2)\right], \qquad (4.19)\end{aligned}$$

where $\theta_{1,2}$ are the polar angles corresponding to writing $\mathbf{r}_{1,2}$ in polar coordinates. Although both beams present the same intensity distribution that does not change apart from a scale during free-space propagation, see Fig. 4.4, their coherence states are significantly different: $\Gamma_{\mathscr{L}_2^2}$ is completely coherent and Γ_Σ is partially coherent. The proposed method distinguishes between both beams and quantize their coherence state. In order to prove it we will simulate their characterization using the proposed simplified PST method and check that the recovered AFs are consistent with the theoretical expectations.

In order to apply the simplified PST we need as inputs the antisymmetric fractional power spectra of each beam. In the case of Γ_{LG} it can directly be numerically calculated transforming the complex amplitude of the LG beam by the FRFT kernel. For Γ_Σ, however, there is no complex amplitude defined since the beam is partially coherent. Taking into account that the beam is composed as the incoherent sum of

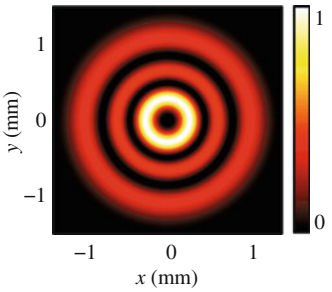

Fig. 4.4 Intensity distribution of the RSBs associated with the MIs $\Gamma_{\mathscr{L}_2^2}$ and Γ_Σ

two modes, its fractional power spectra is expressed as the sum of the fractional power spectra of each mode:

$$S_\Sigma^{\gamma,-\gamma}(\mathbf{r}) = \frac{1}{2}\left[S_{\mathscr{L}_2^2}^{\gamma,-\gamma}(\mathbf{r}) + S_{\mathscr{L}_2^{-2}}^{\gamma,-\gamma}(\mathbf{r})\right], \tag{4.20}$$

We have introduced $S_{\mathscr{L}_p^l}^{\gamma,-\gamma}$ to denote the fractional power spectra associated with the LG beam with azimuthal index l and radial index p.

Plane sections of the AFs of each beam can be recovered from the numerically simulated fractional power spectra. To verify the results, we calculate the theoretical plane sections using the following expression for the AF of a LG mode:

$$\begin{aligned} A_{\mathscr{L}_p^l}(\mathbf{r},\mathbf{p}) = 2L_m &\left\{\frac{\pi}{2w^2}\left[x^2+u^2+y^2+v^2-2(xv-yu)\right]\right\} \\ &\times L_n\left\{\frac{\pi}{2w^2}\left[x^2+u^2+y^2+v^2+2(xv-yu)\right]\right\} \\ &\times \exp\left[-\frac{\pi}{2w^2}\left(\mathbf{r}^2+\mathbf{p}^2\right)\right]. \end{aligned} \tag{4.21}$$

where $(m,n) = (p+l,p)$ for positive l and $(m,n) = (p,p-l)$ for negative l. Equation (4.21) is easily obtained from the expression for the WD of the LG beams derived in [Sim00a], see Sect. 4.7 for details. Notice that in this case the AF is real since it is obtained from the WD by a coordinate transformation. This allows displaying the plane sections in colormap figures with positive and negative colour axis. The linearity of the AF with respect to the MI (see Eq. (1.15)) allows calculating the AF of the beam associated with Γ_Σ as the sum of the AFs of the composing LG modes:

$$A_\Sigma(\mathbf{r},\mathbf{p}) = \frac{1}{2}\left[A_{\mathscr{L}_2^2}(\mathbf{r},\mathbf{p}) + A_{\mathscr{L}_2^{-2}}(\mathbf{r},\mathbf{p})\right]. \tag{4.22}$$

A total of 90 antisymmetrical fractional power spectra with angle γ covering the range $[\pi/2,\pi]$ were numerically calculated. From them, AF plane sections associated with a reference point $\mathbf{r}_0$ were obtained for each beam. The simulated and theoretical AF plane sections associated with two different reference points, $\mathbf{r}_0 = (0.25,0)$ mm and $\mathbf{r}_0 = (0.55,0)$ mm, are displayed in Fig. 4.5 for the case of

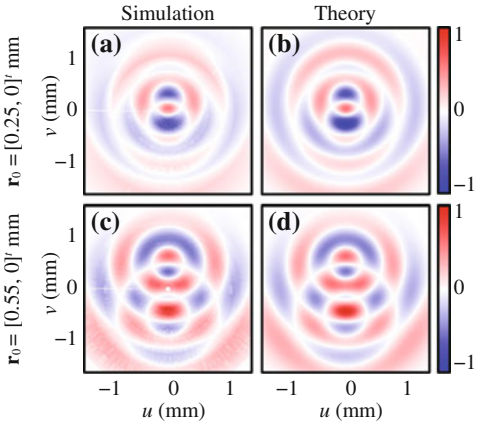

Fig. 4.5 **a**, **b** Simulated and theoretical AF plane sections of the beam Γ_{LG} for the reference point $\mathbf{r}_0 = (0.25, 0)$ mm. **c**, **d** Simulated and theoretical AF plane sections of the beam Γ_{LG} for the reference point $\mathbf{r}_0 = (0.55, 0)$ mm

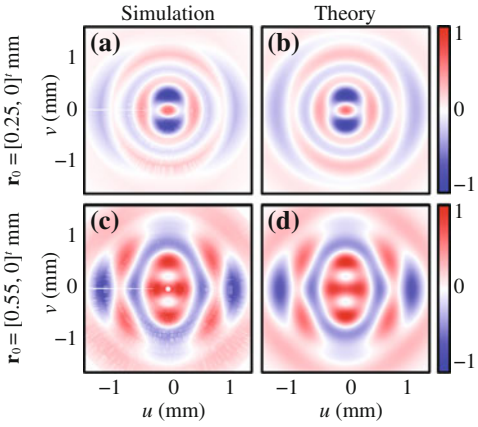

Fig. 4.6 **a**, **b** Simulated and theoretical AF plane sections of the beam Γ_{Σ} for the reference point $\mathbf{r}_0 = (0.25, 0)$ mm. **c**, **d** Simulated and theoretical AF plane sections of the beam Γ_{Σ} for the reference point $\mathbf{r}_0 = (0.55, 0)$ mm

$\Gamma_{\mathscr{L}_2^2}$. Analogous AF plane sections for A_{Σ} are presented in Fig. 4.6. The colormap of both figures is chosen so that positive and negative values are represented by colours in a linear scale of red and blue tones, respectively. The good agreement between the simulated and theoretical results confirms that the proposed method is valid to recover the beam AF plane sections. Notice that as a consequence of the distinct coherence state of both beams, their AF plane sections are considerably different.

The AFs can be further processed into the beam MIs by inverting the FT using Eq. (1.18). Figures 4.7 and 4.8 display the modulus and phase of the MIs, $\Gamma(\mathbf{r} + 1/2\mathbf{r}_0, \mathbf{r} - 1/2\mathbf{r}_0)$, with $\mathbf{r}_0 = (0.55, 0)$ mm, for the simulated and theoretical beams. In particular, the different patterns between Γ_{LG} and Γ_{Σ} due to the their unequal coherence pictures. Also notice that the phase of Γ_{Σ} only contains the values 0 and π as expected according to Eq. (4.19).

Finally, Fig. 4.9 presents the simulated and theoretical modulus of the degree of coherence for both beams. In order to avoid the areas where the degree of coherence

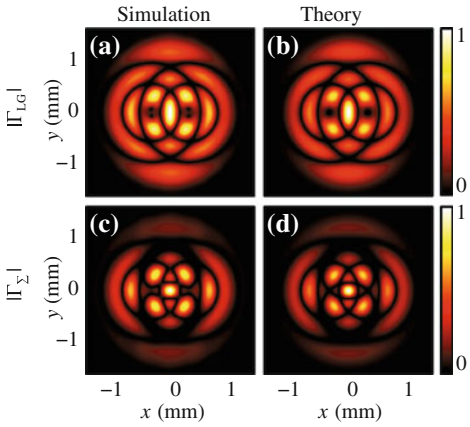

Fig. 4.7 **a** Simulated, and **b** theoretical MI modulus of the beam Γ_{LG} associated with $\Gamma(\mathbf{r}+1/2\mathbf{r}_0, \mathbf{r}-1/2\mathbf{r}_0)$ for the reference point $\mathbf{r}_0 = (0.55, 0)$ mm. **c** Simulated, and **d** theoretical MI modulus of the beam Γ_{Σ} associated with $\Gamma(\mathbf{r}+1/2\mathbf{r}_0, \mathbf{r}-1/2\mathbf{r}_0)$ for the reference point $\mathbf{r}_0 = (0.55, 0)$ mm

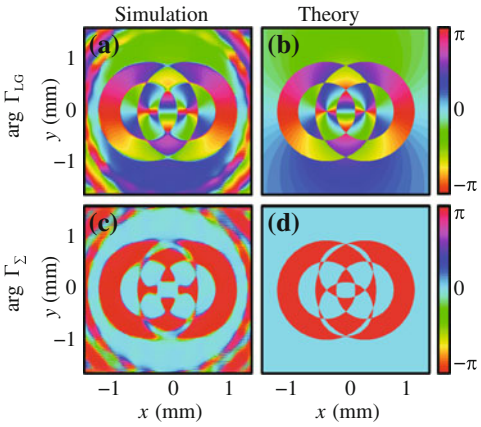

Fig. 4.8 **a** Simulated, and **b** theoretical MI phase of the beam Γ_{LG} associated with $\Gamma(\mathbf{r}+1/2\mathbf{r}_0, \mathbf{r}-1/2\mathbf{r}_0)$ for the reference point $\mathbf{r}_0 = (0.55, 0)$ mm. **c** Simulated, and **d** theoretical MI phase of the beam Γ_{LG} associated with $\Gamma(\mathbf{r}+1/2\mathbf{r}_0, \mathbf{r}-1/2\mathbf{r}_0)$ for the reference point $\mathbf{r}_0 = (0.55, 0)$ mm

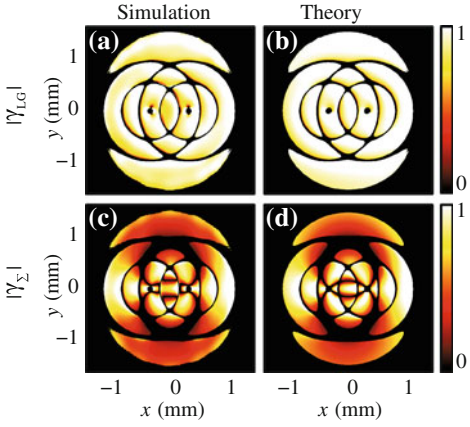

Fig. 4.9 **a** Simulated, and **b** theoretical degree of coherence modulus of the beam Γ_{LG} corresponding to $|\gamma(\mathbf{r}+1/2\mathbf{r}_0, \mathbf{r}-1/2\mathbf{r}_0)|$ for the reference point $\mathbf{r}_0 = (0.55, 0)$ mm. **c** Simulated, and **d** theoretical degree of coherence modulus of the beam Γ_{Σ} corresponding to $|\gamma(\mathbf{r}+1/2\mathbf{r}_0, \mathbf{r}-1/2\mathbf{r}_0)|$ for the reference point $\mathbf{r}_0 = (0.55, 0)$ mm

is not defined, we mask out the points for which $|f(\mathbf{r}+1/2\mathbf{r}_0)f^*(\mathbf{r}-1/2\mathbf{r}_0)|$ is smaller than 5 % of the maximum beam power. Observe that while Γ_{LG} is completely coherent, the degree of coherence associated with Γ_{Σ} is inhomogeneous. This is the definitive proof that the beams posses a coherence state different to each other.

4.4 Experimental Results

To conclude this chapter we demonstrate that the method is experimentally feasible by characterizing a beam generated in the laboratory. The beam antisymmetrical fractional power spectra were measured using the optical system composed by conventional cylindrical lenses presented in Sect. 3.4. The test beam is generated by the diffraction of an spherical wavefront of wavelength $\lambda = 632.8$ nm by an aperture of radius $a = 1.3$ mm. The analytical expression for the resulting complex amplitude is a circular aperture multiplied by a spatial chirp of parameter f:

$$f(\mathbf{r}) = \mathrm{circ}\left(\frac{\mathbf{r}}{a}\right)\exp\left(-\frac{\mathrm{i}\pi}{\lambda \mathrm{f}}r^2\right), \tag{4.23}$$

circ is the circle function defined as

$$\mathrm{circ}\left(\frac{\mathbf{r}}{a}\right) = \begin{cases} 1, \text{ if } |\mathbf{r}| < a \\ 0, \text{ if } |\mathbf{r}| \geq a \end{cases} \tag{4.24}$$

The chirp parameter of the beam was estimated as $\mathrm{f} = 0.71$ m by minimising the differences between a simulated set of antisymmetrical fractional power spectra and the fractional power spectra measured in the experiment. It is important to mention that the aperture was not perfectly circular but decagonal. However, simulation have shown that the beam differences caused by the non-circular aperture are insignificant. Therefore, for the purpose of verification of the method we assume the aperture is circular. The measured intensity distribution of the beam and its estimated phase distribution (corresponding to the chirp parameter) are presented in Fig. 4.10.

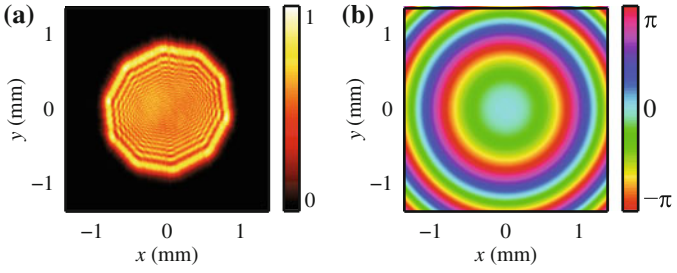

Fig. 4.10 **a** Measured intensity distribution of the generated beam, and **b** its estimated phase distribution, which corresponds to a chirp of parameter $\mathrm{f} = 0.71$ mm

The theoretical expression for the AF of the generated beam is required for the comparison with the experimental results. Since we approximate the aperture by a circular mask, the signal is rotationally invariant. Therefore, it is demonstrated in Sect. 4.7 that its AF can be written in terms of its WD via the following transformation:

$$A(\mathbf{r}, \mathbf{p}) = \frac{1}{2} W\left(-\frac{1}{2}\mathbf{r}, -\frac{1}{2}\mathbf{p}\right). \tag{4.25}$$

A reasonable approximation of the WD of a circular aperture of radius a was derived in [Bas96]. The expression for the WD plane section associated with $\mathbf{r}_0 = [x_0, 0]^T$ is

$$W_{\text{circ}}(\mathbf{r}_0, \mathbf{p}) = C(x_0) \frac{J_1\left[\frac{4\pi}{\sigma^2}\sqrt{(a - x_0)^2 u^2 + \left(a^2 - x_0^2\right) v^2}\right]}{\sqrt{(a - x_0)^2 u^2 + \left(a^2 - x_0^2\right) v^2}}, \tag{4.26}$$

where

$$C(x_0) = 4\pi a^2 \left[1 - \frac{2}{\pi}\arcsin\frac{x_0}{a} - \frac{2x_0}{\pi a}\sqrt{1 - \left(\frac{x_0}{a}\right)^2}\right] \tag{4.27}$$

is a constant that only depends on the ratio between $|\mathbf{r}_0|$ and the radius of the circular aperture, x_0/a.

The WD has to be further transformed to account for the chirp multiplication. The chirp multiplication corresponds to a change of coordinates of the WD given by Eq. (1.29) with

$$\mathbf{T} = \begin{bmatrix} \mathbf{A} & \mathbf{B} \\ \mathbf{C} & \mathbf{D} \end{bmatrix} = \begin{bmatrix} \mathbf{I} & \mathbf{0} \\ -\frac{1}{\lambda \mathrm{f}}\mathbf{I} & \mathbf{0} \end{bmatrix}. \tag{4.28}$$

In a nutshell, it consists in the change

$$\mathbf{r} \longmapsto \mathbf{r}, \tag{4.29}$$

$$\mathbf{p} \longmapsto \mathbf{p} + \frac{1}{\lambda \mathrm{f}}\mathbf{r}, \tag{4.30}$$

which is simply a translation on the spatial frequency coordinate proportional to the reference point. The resulting AF plane section associated with $\mathbf{r}_0 = [x_0, 0]^T$ is expressed as

$$\begin{aligned} A_f(\mathbf{r}_0, \mathbf{p}) &= 4C\left(\frac{x_0}{2}\right) \frac{J_1\left[\frac{\pi}{\sigma^2}\sqrt{(2a + x_0)^2\left(-u + \frac{x_0}{\lambda \mathrm{f}}\right)^2 + \left(4a^2 - x_0^2\right) v^2}\right]}{\sqrt{(2a + x_0)^2\left(-u + \frac{x_0}{\lambda \mathrm{f}}\right)^2 + \left(4a^2 - x_0^2\right) v^2}} \\ &= W_{\text{circ}}\left(-\frac{1}{2}\mathbf{r}_0, -\frac{1}{2}\mathbf{p} - \frac{1}{2\lambda \mathrm{f}}\mathbf{r}_0\right). \end{aligned} \tag{4.31}$$

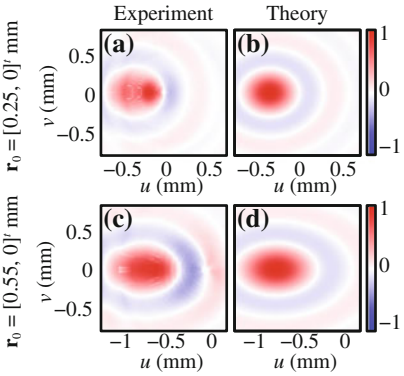

Fig. 4.11 **a**, **b** Experimental and theoretical AF plane sections for the reference point $\mathbf{r}_0 = [0.25, 0]^T$ mm of the chirped circular aperture. **c**, **d** Experimental and theoretical AF plane sections for the reference point $\mathbf{r}_0 = [0.55, 0]^T$ mm of the chirped circular aperture

A total of 40 antisymmetrical fractional power spectra with angle covering the range $\gamma \in [\pi/2, 3\pi/2)$ were measured in the experiment. Although all of them were used for the estimation of the chirp parameter, only the 20 of them associated with the angles in the range $[\pi/2, 0]$ were actually used for obtaining the AF plane sections. The experimental and theoretical plane sections associated with two different reference points, $\mathbf{r}_0 = [0.25, 0]^T$ and $\mathbf{r}_0 = [0.55, 0]^T$ mm, are presented in Fig. 4.11. Despite the reduced number of measured projections, the experimental AF plane sections still agree considerably with the theoretical predictions. This demonstrates the feasibility of the proposed method for characterizing experimentally-generated beams. Notice that the AF plane sections are presented in Cartesian coordinates. Hence, the beam MI can be recovered from the AF plane sections applying Eq. (1.18).

As the techniques proposed in previous sections, this method can be applied to an a priori unknown beam if we prove it is rotationally symmetric. Therefore, before the application of the method, the beam must pass a test that demonstrates it is rotationally symmetric. The test consists in checking that its fractional power spectra associated with both angles $\gamma = \pi$ and $\gamma = \pi/2$ are invariant respect to rotation. In other words, a beam $\Gamma(\mathbf{r}_1, \mathbf{r}_2)$ that satisfies

$$S^{\pi,-\pi}(\mathbf{r}) = S^{\pi,-\pi}(r), \tag{4.32}$$

$$S^{\pi/2,-\pi/2}(\mathbf{r}) = S^{\pi/2,-\pi/2}(r), \tag{4.33}$$

is rotationally symmetric. The validity of this test is derived in detail in Sect. 4.8.

4.5 Conclusions

In summary, this chapter proposes a simplified phase-space tomography method for the spatial characterization of monochromatic completely or partially coherent RSBs. The method has been verified by simulations and its feasibility for real-world applications has been demonstrated by an experimental example. Even though we

only measured 20 fractional power spectra, the good agreement between experiment and theory proves that the technique can be used for fast characterization of beams. The method can be applied to any a priori unknown beam that satisfies the rotationally symmetry test presented as the conditions of Eqs. (4.32) and (4.33). We underline that the method can be experimentally applied using the same setup as for the characterization of separable beams, see Chap. 3.

Most of these results are published in [Cám14] and were presented at the congresses [Ali12a, Cám12b, Ali12c]. In addition, the procedures to characterize RSBs together with the optical system, have been the object of a patent application [Ali12b].

Appendices

4.6 Simplification of RSB Characterization

Imagine that we measure N^2 fractional power spectra of a beam where both γ_x and γ_y equidistantly and independently range in a π-interval. Applying the conventional phase-space tomography method proposed in [Ray94] we can recover the beam WD with certain sampling rate in phase space. This section demonstrates that if the beam is a RSB, then only $N/2$ of the measured antisymmetrical fractional power spectra are required to obtain the same information.

First of all, the angles $\gamma_{x,y}$ of the fractional power spectra do not need to range independently: the antisymmetric set ($\gamma_x = -\gamma_y = \gamma$) suffices to sample the entire AF of the RSB. Let us prove this by considering the AF radial section in hat coordinates obtained from an arbitrary antisymmetrical fractional power spectra and its relation with the AF in tilde coordinates, c.f. Eqs. (4.9) and (4.10):

$$\widehat{A}\left(R_x, \pi/2-\gamma, R_y, \pi/2+\gamma\right) = \widetilde{A}\left(r_0, \theta_{r0}, p_0, \theta_{p0}\right). \tag{4.34}$$

The first impression is that there must be some $\widetilde{A}$ values that cannot be reached by Eq. (4.34) since there are four variables on the right-hand-side, $(r_0, \theta_{r0}, p_0, \theta_{p0})$, and only three on the left-hand-side, (R_x, R_y, γ). In other words, the equation system

$$r_0 = \sqrt{(R_x \sin\gamma)^2 + \left(-R_y \sin\gamma\right)^2} = |\sin\gamma|\sqrt{R_x^2 + R_y^2}, \tag{4.35}$$

$$\theta_{r0} = \arctan\left(\frac{-R_y \sin\gamma}{R_x \sin\gamma}\right) = -\arctan\left(\frac{R_y}{R_x}\right), \tag{4.36}$$

$$p_0 = \sqrt{(R_x \cos\gamma)^2 + \left(R_y \cos\gamma\right)^2} = |\cos\gamma|\sqrt{R_x^2 + R_y^2}, \tag{4.37}$$

$$\theta_{p0} = \arctan\left(\frac{R_y \cos\gamma}{R_x \cos\gamma}\right) = \arctan\left(\frac{R_y}{R_x}\right). \tag{4.38}$$

is not solvable for all values of θ_{r0}, and θ_{p0} because there is a dependence relation between Eqs. (4.36) and (4.38). However, taking into account that the beam is rotationally symmetric, i.e. the AF is invariant to the change

$$\theta_{r0} \mapsto \theta_{r0} + \theta_0, \tag{4.39}$$
$$\theta_{p0} \mapsto \theta_{p0} + \theta_0, \tag{4.40}$$

we can break the dependence and make the equation system solvable:

$$r_0 = |\sin\gamma| \sqrt{R_x^2 + R_y^2}, \tag{4.41}$$
$$\theta_{r0} = \theta_0 - \arctan\left(\frac{R_y}{R_x}\right), \tag{4.42}$$
$$p_0 = |\cos\gamma| \sqrt{R_x^2 + R_y^2}, \tag{4.43}$$
$$\theta_{p0} = \theta_0 + \arctan\left(\frac{R_y}{R_x}\right). \tag{4.44}$$

The presence of the terms $(R_x^2 + R_y^2)^{1/2}$ and $\arctan R_y/R_x$ in Eqs. (4.41)–(4.44) hints for converting (R_x, R_y) in polar coordinates (R, θ_R) via the change of variables

$$R = \sqrt{R_x^2 + R_y^2}, \tag{4.45}$$
$$\theta_R = \arctan\left(\frac{R_y}{R_x}\right). \tag{4.46}$$

Recall that R_x and R_y may take negative values since α_x and α_y only range in a π-range interval, and hence the change is valid. Doing so, the system of Eqs. (4.41)–(4.44) becomes

$$r_0 = R\,|\sin\gamma|\,, \tag{4.47}$$
$$\theta_{r0} = \theta_0 - \theta_R, \tag{4.48}$$
$$p_0 = R\,|\cos\gamma|\,, \tag{4.49}$$
$$\theta_{p0} = \theta_0 + \theta_R, \tag{4.50}$$

or equivalently

$$R = \sqrt{r_0^2 + p_0^2}, \tag{4.51}$$
$$\theta_R = \frac{1}{2}\left(\theta_{p0} - \theta_{r0}\right), \tag{4.52}$$
$$\theta_0 = \frac{1}{2}\left(\theta_{r0} + \theta_{p0}\right), \tag{4.53}$$
$$|\tan\gamma| = \frac{r_0}{p_0}. \tag{4.54}$$

Notice that Eq. (4.54) can be inverted since both r_0 and p_0 take only positive values:

$$\gamma = \arctan\left(\frac{r_0}{p_0}\right). \tag{4.55}$$

This concludes the demonstration that using the antisymmetrical fractional power spectra we can sample the entire AF of a RSB. This allows reducing from N^2 to N the number of required projections.

Finally, to further reduce the number of projections from N to $N/2$ we now show that only the angles contained in a $\pi/2$-range interval are required. This can be concluded from Eq. (4.54) in which the angle γ is confined in the first quadrant, $\gamma \in [0, \pi/2)$. Remember that both r_0 and p_0 are positive definite. Notice that the angles in the interval $[\pi/2, \pi)$ and $[-\pi/2, 0)$ are mapped to the first quadrant by the absolute value of the left-hand-side of Eq. (4.54). Therefore, the antisymmetrical fractional power spectra associated with γ outside the first quadrant are redundant.

These two facts allow reducing the number of projections needed for the AF reconstruction from N^2 in the general case—N for each angle, γ_x and γ_y, covering a π-range interval—to $N/2$ in the case of RSBs –N for the antisymmetric angle, γ, covering a $\pi/2$-range interval– without affecting the sampling rate of the phase space.

4.7 AF of a LG Mode

This section provides a detailed calculation of the AF of a LG mode from the WD of a HG mode. The procedure is the following:

1. Relate the WD and the AF of a centre-symmetric beam, i.e. a beam for which its (stochastic) complex field amplitude is an eigenfunction of the inversion operator.
2. Calculate the AF of a HG mode from its WD using the previous result, since the HG mode is centre-symmetric.
3. Transform the AF using Gyrator (recall Sect. 1.3) to convert the resulting AF for the HG mode into the AF for the LG mode.

WD and AF of Centre-Symmetric Beam

The WD and the AF of a beam are calculated in a similar way, so it is no surprise that under certain conditions both functions are equal to each other apart from a scaling. Firstly, consider the definition of the WD,

$$W(\mathbf{r}, \mathbf{p}) = \frac{1}{s^2}\int \mathrm{d}\mathbf{r}'\, \Gamma\left(\mathbf{r} + \frac{1}{2}\mathbf{r}', \mathbf{r} - \frac{1}{2}\mathbf{r}'\right) \exp\left(-\frac{\mathrm{i}2\pi}{s^2}\mathbf{p}^T\mathbf{r}'\right). \tag{4.56}$$

Applying the change of variables $\mathbf{r}' \mapsto 2\left(\mathbf{r} - \mathbf{r}'\right)$ the WD is rewritten as

$$W\left(\mathbf{r}, \mathbf{p}\right) = \frac{2}{s^2} \exp\left(-\frac{\mathrm{i}4\pi}{s^2}\mathbf{r}^T\mathbf{p}\right) \int \mathrm{d}\mathbf{r}'\, \Gamma\left(2\mathbf{r} - \mathbf{r}', \mathbf{r}'\right) \exp\left(\frac{\mathrm{i}4\pi}{s^2}\mathbf{p}^T\mathbf{r}'\right). \quad (4.57)$$

Similarly, from the change of variables $\mathbf{r}' \mapsto \mathbf{r}' + \mathbf{r}/2$ in the AF definition, see Eq. (1.15), it is obtained that

$$\begin{aligned} A\left(\mathbf{r}, \mathbf{p}\right) &= \frac{1}{s^2} \int \mathrm{d}\mathbf{r}'\, \Gamma\left(\mathbf{r}' + \frac{1}{2}\mathbf{r}, \mathbf{r}' - \frac{1}{2}\mathbf{r}\right) \exp\left(-\frac{\mathrm{i}2\pi}{s^2}\mathbf{p}^T\mathbf{r}'\right) \\ &= \frac{1}{s^2} \exp\left(\frac{\mathrm{i}\pi}{s^2}\mathbf{r}^T\mathbf{p}\right) \int \mathrm{d}\mathbf{r}'\, \Gamma\left(\mathbf{r}' + \mathbf{r}, \mathbf{r}'\right) \exp\left(-\frac{\mathrm{i}2\pi}{s^2}\mathbf{p}^T\mathbf{r}'\right). \end{aligned} \quad (4.58)$$

Secondly, a centre-symmetric beam is described by a complex field amplitude that is eigenfunction of the inversion operator:

$$f\left(\mathbf{r}\right) = \kappa f\left(-\mathbf{r}\right), \quad (4.59)$$

where κ is the eigenvalue. Therefore, its MI satisfies

$$\Gamma\left(\mathbf{r}_1, \mathbf{r}_2\right) = \kappa \Gamma\left(-\mathbf{r}_1, \mathbf{r}_2\right). \quad (4.60)$$

Inserting Eq. (4.60) in the expression for the WD of Eq. (4.57) we obtain

$$W\left(\mathbf{r}, \mathbf{p}\right) = \frac{2\kappa}{\sigma^2} \exp\left(\frac{\mathrm{i}\pi}{\sigma^2}\mathbf{r}^T\mathbf{p}\right) \int \mathrm{d}\mathbf{r}'\, \Gamma\left(\mathbf{r}' - 2\mathbf{r}, \mathbf{r}'\right) \exp\left(-\frac{\mathrm{i}2\pi}{\sigma^2}\mathbf{p}^T\mathbf{r}'\right). \quad (4.61)$$

Comparing Eqs. (4.58) and (4.61) it is concluded that the following relation

$$A\left(\mathbf{r}, \mathbf{p}\right) = \frac{1}{2\kappa} W\left(-\frac{1}{2}\mathbf{r}, -\frac{1}{2}\mathbf{p}\right), \quad (4.62)$$

is satisfied for any centre-symmetric beam.

AF of a HG Mode

The expression for the WD of a HG mode $\mathscr{H}_{m,n}$, see Eq. (1.6), is already present in the literature [Sim00a]:

$$\begin{aligned} W_{\mathscr{H}_{m,n}}\left(\mathbf{r}, \mathbf{p}\right) = (-1)^{m+n}\, 4 L_m\left[\frac{4\pi}{w^2}\left(x^2 + u^2\right)\right] L_n\left[\frac{4\pi}{w^2}\left(y^2 + v^2\right)\right] \\ \times \exp\left[-\frac{2\pi}{w^2}\left(\mathbf{r}^2 + \mathbf{p}^2\right)\right], \end{aligned} \quad (4.63)$$

where $L_m \equiv L_m^0$ is the Laguerre polynomial of index m. Since the HG modes are eigenfunctions of the inversion operator,

$$\mathscr{H}_{m,n}(\mathbf{r}) = (-1)^{m+n}\,\mathscr{H}_{m,n}(-\mathbf{r}), \tag{4.64}$$

its AF and WD are related via Eq. (4.62),

$$\begin{aligned} A_{\mathscr{H}_{m,n}}(\mathbf{r},\mathbf{p}) &= \frac{(-1)^{m+n}}{2} W_{\mathscr{H}_{m,n}}\left(-\frac{1}{2}\mathbf{r}, -\frac{1}{2}\mathbf{p}\right) \\ &= 2L_m\left[\frac{\pi}{w^2}\left(x^2+u^2\right)\right] L_n\left[\frac{\pi}{w^2}\left(y^2+v^2\right)\right] \\ &\quad \times \exp\left[-\frac{\pi}{2w^2}\left(\mathbf{r}^2+\mathbf{p}^2\right)\right]. \end{aligned} \tag{4.65}$$

AF of a LG Mode

The relation between the AF of a HG mode and a LG mode is given by a rotation in phase space. This is derived from the mode conversion performed by the Gyrator transform, see Sect. 1.13 and [Rod07a]. The change of coordinates associated with Gyrator is given by the phase-space rotation

$$\begin{bmatrix} x \\ y \\ u \\ v \end{bmatrix} \longmapsto \begin{bmatrix} \cos\beta & 0 & 0 & \sin\beta \\ 0 & \cos\beta & \sin\beta & 0 \\ 0 & -\sin\beta & \cos\beta & 0 \\ -\sin\beta & 0 & 0 & \cos\beta \end{bmatrix} \begin{bmatrix} x \\ y \\ u \\ v \end{bmatrix}, \tag{4.66}$$

which produces the following change in these quantities

$$\begin{aligned} x^2+u^2 \longmapsto & \left(x^2+u^2\right)\cos^2\beta + \left(y^2+v^2\right)\sin^2\beta \\ & - 2\cos\beta\sin\beta\,(xv-yu), \end{aligned} \tag{4.67}$$

$$\begin{aligned} y^2+v^2 \longmapsto & \left(x^2+u^2\right)\sin^2\beta + \left(y^2+v^2\right)\cos^2\beta \\ & + 2\cos\beta\sin\beta\,(xv-yu), \end{aligned} \tag{4.68}$$

$$x^2+y^2+u^2+v^2 \longmapsto x^2+y^2+u^2+v^2. \tag{4.69}$$

In particular, the change for $\beta = \pi/4$ converts the HG beam $\mathscr{H}_{m,n}$ into the LG beam $\mathscr{L}_p^l$ with $l = m-n$ and $p = \min(m,n)$. Applying the change of coordinates to the expression of the AF for a HG mode, Eq. (4.65), allows obtaining the expression of the AF for a LG mode:

$$\begin{aligned} A_{\mathscr{L}_p^l}(\mathbf{r},\mathbf{p}) &= 2L_m\left\{\frac{\pi}{2w^2}\left[x^2+u^2+y^2+v^2-2\,(xv-yu)\right]\right\} \\ &\quad \times\; L_n\left\{\frac{\pi}{2w^2}\left[x^2+u^2+y^2+v^2+2\,(xv-yu)\right]\right\} \\ &\quad \times \exp\left[-\frac{\pi}{2w^2}\left(\mathbf{r}^2+\mathbf{p}^2\right)\right]. \end{aligned} \tag{4.70}$$

4.8 Demonstration of the Rotationally Symmetry Test

This section demonstrates the validity of the method that checks if an a priori unknown beam is rotationally symmetric. The test states that if the two antisymmetric fractional power spectra associated with $\gamma = \pi$ and $\gamma = \pi/2$ of a beam are rotationally invariant then the beam must be rotationally symmetric, i.e. it must satisfy Eq. (4.8).

The antisymmetrical fractional power spectra associated with an abitrary angle γ in the range $[\pi/2, 0)$ is defined in terms of the MI as

$$\begin{aligned} S^{\gamma,-\gamma}(\mathbf{r}) = & \frac{1}{\sigma^2 |\sin\gamma|} \int \mathrm{d}\mathbf{r}_1 \mathrm{d}\mathbf{r}_2 \, \Gamma(\mathbf{r}_1, \mathbf{r}_2) \\ & \times \exp\left\{ -\frac{\mathrm{i}\pi}{\sigma^2 \sin\gamma} \left[\left(x_1^2 - x_2^2 - y_1^2 + y_2^2 \right) \cos\gamma \right.\right. \\ & \left.\left. - 2x(x_1 - x_2) + 2y(y_1 - y_2) \right] \right\}. \end{aligned} \tag{4.71}$$

Introducing polar coordinates, $(\mathbf{r}) \mapsto (r, \theta)$, which allows writing the rotation symmetry in an explicit way, the following quantities can be written as

$$\begin{aligned} x_1^2 - x_2^2 - y_1^2 + y_2^2 &= r_1^2 \left(\cos^2\theta_1 - \sin^2\theta_1 \right) - r_2^2 \left(\cos^2\theta_2 - \sin^2\theta_2 \right) \\ &= r_1^2 \cos(2\theta_1) - r_2^2 \cos(2\theta_2), \end{aligned} \tag{4.72}$$

$$x(x_1 - x_2) = r\cos\theta (r_1 \cos\theta_1 - r_2 \cos\theta_2), \tag{4.73}$$

$$y(y_1 - y_2) = r\sin\theta (r_1 \sin\theta_1 - r_2 \sin\theta_2), \tag{4.74}$$

$$\begin{aligned} x(x_1 - x_2) - y(y_1 - y_2) &= r [r_1 (\cos\theta_1 \cos\theta - \sin\theta_1 \sin\theta) \\ &\quad - r_2 (\cos\theta_2 \cos\theta - \sin\theta_2 \sin\theta)] \\ &= r [r_1 \sin(\theta_1 + \theta) - r_2 \sin(\theta_2 + \theta)]. \end{aligned} \tag{4.75}$$

Substituting them into Eq. (4.71), the fractional power spectra in polar coordinates is transformed into

$$\begin{aligned} S^{\gamma,-\gamma}(r, \theta) = & \frac{1}{\sigma^2 |\sin\gamma|} \int r_1 \mathrm{d}r_2 \mathrm{d}\theta_1 \, r_2 \mathrm{d}r_2 \mathrm{d}\theta_2 \, \widetilde{\Gamma}(r_1, \theta_1, r_2, \theta_2) \\ & \times \exp\left(-\frac{\mathrm{i}\pi}{\sigma^2 \sin\gamma} \left\{ \left[r_1^2 \cos(2\theta_1) - r_2^2 \cos(2\theta_2) \right] \cos\gamma \right.\right. \\ & \left.\left. - 2r [r_1 \sin(\theta_1 + \theta) - r_2 \sin(\theta_2 + \theta)] \right\} \right). \end{aligned} \tag{4.76}$$

Notice that the only contribution of the output polar angle, θ, is present in the third row of Eq. (4.76). Performing the following change of integration variables,

$$\theta_1 \longmapsto \theta_1 - \theta, \tag{4.77}$$

$$\theta_2 \longmapsto \theta_2 - \theta, \tag{4.78}$$

and recalling that the angular integrals for θ_1 and θ_2 are along a full cycle, 2π, Eq. (4.76) is rewritten as

$$S^{\gamma,-\gamma}(r,\theta) = \frac{1}{\sigma^2 |\sin\gamma|} \int r_1 \mathrm{d}r_2 \mathrm{d}\theta_1 \, r_2 \mathrm{d}r_2 \mathrm{d}\theta_2 \, \widetilde{\Gamma}(r_1, \theta_1 - \theta, r_2, \theta_2 - \theta)$$
$$\times \exp\left(-\frac{\mathrm{i}\pi}{\sigma^2 \sin\gamma}\left\{\left[r_1^2 \cos(2\theta_1 - 2\theta) - r_2^2 \cos(2\theta_2 - 2\theta)\right]\cos\gamma\right.\right.$$
$$\left.\left. -2r\,(r_1 \sin\theta_1 - r_2 \sin\theta_2)\right\}\right). \tag{4.79}$$

The only way that the fractional power spectra associated with $\gamma = \pi/2$,

$$S^{\pi/2,-\pi/2}(r,\theta) = \frac{1}{\sigma^2} \int r_1 \mathrm{d}r_2 \mathrm{d}\theta_1 \, r_2 \mathrm{d}r_2 \mathrm{d}\theta_2 \, \widetilde{\Gamma}(r_1, \theta_1 - \theta, r_2, \theta_2 - \theta)$$
$$\times \exp\left[\frac{\mathrm{i}2\pi}{\sigma^2} r\,(r_1 \sin\theta_1 - r_2 \sin\theta_2)\right]. \tag{4.80}$$

is rotationally invariant is by the beam satisfying

$$\widetilde{\Gamma}(r_1, \theta_1 - \theta, r_2, \theta_2 - \theta) = \widetilde{\Gamma}(r_1, \theta_1, r_2, \theta_2), \tag{4.81}$$

which is the condition for a beam to be rotationally symmetric. In conclusion, a RSB must satisfy that

$$S^{\pi,-\pi}(\mathbf{r}) = S^{\pi,-\pi}(r), \tag{4.82}$$

$$S^{\pi/2,-\pi/2}(\mathbf{r}) = S^{\pi/2,-\pi/2}(r). \tag{4.83}$$

References

[Ali00] T. Alieva, M.J. Bastiaans, Wigner distribution and fractional Fourier transform for two-dimensional symmetric optical beams. J. Opt. Soc. Am. A **17**(12), 2319–2323 (2000)

[Ali12a] T. Alieva, A. Cámara, *Beam symmetry considerations for Wigner distribution reconstruction*, Frontiers in Optics Proceedings (Optical Society of America, New York, 2012)

[Ali12b] T. Alieva, A. Cámara, J.A. Rodrigo. Analizador de la estructura y coherencia espacial de haces luminosos. Patent application P201200783, Aug 2012

[Ali12c] T. Alieva, A. Cámara, J.A. Rodrigo, M.L. Calvo, *Projections of Wigner distribution for optical beam characterization*. PIERS Proceedings. Progress in Electromagnetic Research Symposium (2012)

[Ali13] T. Alieva, J.A. Rodrigo, A. Cámara, E. Abramochkin, Partially coherent stable and spiral beams. J. Opt. Soc. Am. A **30**(11), 2237–2243 (2013)

[Bas96] M.J. Bastiaans, P.G.J. Van de Mortel, Wigner distribution function of a circular aperture. J. Opt. Soc. Am. A **13**(8), 1698–1703 (1996)

[Cám12b] A. Cámara, I. Castro, T. Alieva, in *Experimental reconstruction of the Wigner distribution of rotationally symmetric beams*, PIERS Proceedings Progress in Electromagnetic Research Symposium (2012)

[Cám13a] A. Cámara, J.A. Rodrigo, T. Alieva, Optical coherenscopy based on phase-space tomography. Opt. Express **21**(11), 13169–13183 (2013)

[Cám14] A. Cámara, T. Alieva, I. Castro, J.A. Rodrigo, Phase-space tomography for characterization of rotationally symmetric beams. J. Opt. **16**(1), 015705 (2014)

[Gib04] G. Gibson, J. Courtial, M. Padgett, M. Vasnetsov, V. Pas'ko, S. Barnett, S. Franke-Arnold, Free-space information transfer using light beams carrying orbital angular momentum. Opt. Express **12**(22), 5448–5456 (2004)

[Goo05] J.W. Goodman, *Introduction to Fourier Optics* (Roberts & Company, Colorado, 2005)

[Gor98] F. Gori, M. Santarsiero, R. Borghi, S. Vicalvi, Partially coherent sources with helicoidal modes. J. Mod. Opt. **45**(3), 539–554 (1998)

[Gri03] D.G. Grier, A revolution in optical manipulation. Nature **424**(6950), 810–816 (2003)

[Pon01] S.A. Ponomarenko, A class of partially coherent beams carrying optical vortices. J. Opt. Soc. Am. A **18**(1), 150–156 (2001)

[Ray94] M.G. Raymer, M. Beck, D.F. McAlister, Complex wave-field reconstruction using phase-space tomography. Phys. Rev. Lett. **72**(8), 1137–1140 (1994)

[Ric03] J.C. Ricklin, F.M. Davidson, Atmospheric optical communication with a Gaussian Schell beam. J. Opt. Soc. Am. A **20**(5), 856–866 (2003)

[Rod07a] J.A. Rodrigo, T. Alieva, M.L. Calvo, Experimental implementation of the Gyrator transform. J. Opt. Soc. Am. A **24**(10), 3135–3139 (2007)

[Sim00a] R. Simon, G.S. Agarwal, Wigner representation of Laguerre-Gaussian beams. Opt. Lett. **25**(18), 1313–1315 (2000)

[Wan12] J. Wang, J.-Y. Yang, I.M. Fazal, N. Ahmed, Y. Yan, H. Huang, Y. Ren, Y. Yue, S. Dolinar, M. Tur, A.E. Willner, Terabit free-space data transmission employing orbital angular momentum multiplexing. Nat. Photon **6**, 488–496 (2012)

Chapter 5
General Beams

5.1 Introduction

All coherence characterization techniques studied until this chapter assume certain symmetries of the beam to be analyzed. This allowed simplifying the process to a point in which it was suitable in real-world situations. Many applications, however, can benefit from obtaining coherence pictures of *arbitrary beams*, i.e. beams for which we cannot assume a concrete coherence model. Consider for example the characterization of atmospheric [Shi03] and plasma [Mic04] instabilities. Even if the original beam is symmetric, after its propagation through these random media it becomes asymmetric. In addition, coherence symmetries reduce the degrees of freedom of the beam, thus reducing the transmission capacity in free-space communications [Wan12] and deteriorating information encoding [Zal00].

In order to characterize the coherence of an arbitrary beam we cannot use the techniques presented in Chaps. 2–4. Instead, we have to fall back to a general method like conventional PST proposed in [Ray94]. However, PST still presents poor performance due to the problems introduced in Sect. 1.6:

1. Lack of a suitable optical system that allows acquiring the required measurements in a reduced end to end time.
2. Excessive computation effort to process the measured data into the requested result (beam WD, AF, or MI).

These inconveniences are unacceptable for any modern application. In order to overcome them we propose an alternative approach that is referred to as PSTC due to its focus on the recovery of beams coherence picture.

PSTC is a phase-space tomographic method that was developed with two goals in mind that fundamentally differentiate it from PST. Firstly, while conventional PST is optimized for the reconstruction of the beam WD, the aim of PSTC is the MI recovery. Secondly, all the tasks involved in PSTC are prepared to be performed concurrently. Data acquisition and processing can be executed in parallel, as well as

A. Cámara, *Optical Beam Characterization via Phase-Space Tomography*,
Springer Theses, DOI 10.1007/978-3-319-19980-1_5

the different steps in which the data processing task is divided into. These advantages make PSTC a suitable technique for efficient coherence characterization of arbitrary beams.

In Sect. 5.2 we describe the PSTC method and provide instructions of how to apply it. The optical system used for its application is presented in Sect. 5.3. In Sect. 5.4 we validate the technique for a experimentally-generated coherent beam by comparing the phase distributions obtained by our method and an alternative well-established phase retrieval algorithm. The experimental feasibility of PSTC for the characterization of partially coherent beams is demonstrated in two independent experiments presented in Sect. 5.5. One experiment targets partially coherent beams originated by illuminating a computer-generated hologram with a GSMB, while the other uses partially coherent beams obtained via incoherent sum of orthogonal coherent LG modes. Finally, in Sect. 5.6 we summarize the major advantages of PSTC.

5.2 Phase Space Tomographic Coherenscopy

A tomographic technique, as presented in Sect. 1.6, allows reconstructing an object from a set of its projections. For a 2D object such set is unequivocally formed by the projections obtained by relatively rotating the object in its plane with respect to the detector. For N-dimensional objects, however, there is certain freedom to choose the complete projection set. Not all of them are appropriate for the efficient reconstruction of the desired object information.

In order to illustrate the importance of the choice of projection sets, let us consider the reconstruction of a 3D object. We observe that the set of vertical projections obtained by rotating the object round its vertical axis allows easily reconstructing the 2D horizontal sections of the object. An illustration of the tomographic scheme is displayed in Fig. 5.1. The set of projections is a function, $P^{\phi}(\xi, z)$, that depends on the horizontal and vertical variables, ξ[1] and z, and the rotation angle, ϕ. The horizontal section for a fixed value of the vertical axis, z_0, depends on the horizontal variables: $S_{z_0}(x, y)$. This is the ideal scheme to apply the Radon transform [Rad86] since for the reconstruction of the horizontal section associated with z_0 only the projection set values with $z = z_0$ are required. However, the whole projection set is needed to obtain any *vertical section* of the object.

The reconstruction of a 4D object, like the WD, using a phase-space tomographic technique is a procedure similar to the previous 3D example. There is a variety of projection sets that can be chosen for the complete beam characterization. Remember that any rotation in phase space can be expressed in terms of the FRFT and rotator operators by Eq. (1.40):

$$\mathbf{T}_R^{\beta}\mathbf{T}_F^{\gamma_x,\gamma_y}\mathbf{T}_R^{\alpha}. \tag{5.1}$$

[1] ξ corresponds to x or y for $\phi = 0$ or $\phi = \pi/2$, correspondingly.

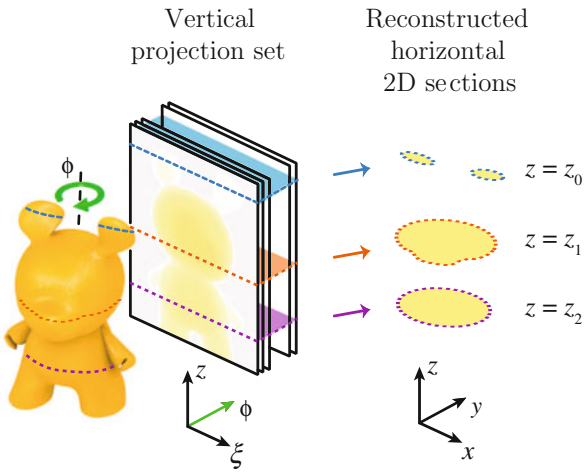

Fig. 5.1 Example illustrating a projection set choice for 3D object tomography appropriate for the reconstruction of horizontal 2D sections

Since we measure 2D intensity distributions (WD projections), only two independent angles need to be varied in order to obtain a complete projection set. Depending on the beam information that we aim to recover and on the available optical setup, different projection sets can be used. In particular, PST chooses the projections corresponding to the FRFT operation ($\alpha = \beta = 0$), which is associated with a rotation in the xu and yv planes in phase space. Although these projections are suitable for the reconstruction of the beam WD, the required processing is computationally expensive. In addition, the WD has to be further processed to extract the MI of the beam.

In PSTC we propose a different choice of projection set. Instead of rotating in the xu and yv phase-space planes, the rotations are performed in the xy and yv planes, which corresponds to $\beta = \gamma_x = 0$ in Eq. (5.1). Note that the rotation in the xy plane also affects to the uv plane. We denote the full set of projections as $P^{\alpha,\gamma}(\mathbf{r})$, where α and γ stand for the xy and yv rotation angles, correspondingly. This selection has important benefits that can be exploited to improve the characterization method.

In order to demonstrate the advantages of this choice let us consider initially the subset of projections associated with $\alpha = 0$. It is easy to show, refer to Sect. 5.7, that a projection of such set satisfies

$$P^{0,\gamma}(\mathbf{r}) = \int \mathrm{d}v \; W_x\left(y', v'\right), \tag{5.2}$$

where W_x is a real function related to the beam MI via

$$W_x(y, v) = \int \mathrm{d}y' \; \Gamma\left(x, y + \frac{1}{2}y', x, y - \frac{1}{2}y'\right) \exp\left(-\mathrm{i}2\pi y' v\right). \tag{5.3}$$

It corresponds to the WD of the 1D signal described by $\Gamma(x, y_1, x, y_2)$ for fixed x. Primed variables relate to non-primed variables by the following coordinate rotation:

$$\begin{bmatrix} y' \\ v' \end{bmatrix} = \begin{bmatrix} \cos\gamma & \sin\gamma \\ -\sin\gamma & \cos\gamma \end{bmatrix} \begin{bmatrix} y \\ v \end{bmatrix}. \tag{5.4}$$

Notice that Eqs. (5.2) and (5.4) correspond to the Radon transform of a 2D object like it was defined in Eq. (1.56). In this case the 2D object is W_x, which can be recovered from the projection subset by applying a tomographic reconstruction algorithm. The beam MI is related to W_x by a FT, see Eq. (5.3).

Evidently, not all the coherence information can be obtained from the projection subset associated with $\alpha = 0$. Only a portion of the complete MI is exposed through W_x. In fact, inverting Eq. (5.3) and performing the change of variables $y \to (y_1 + y_2)/2$ and $y' \to y_1 - y_2$ we find that the MI that can be accessed is:

$$\Gamma(x, y_1, x, y_2) = \int \mathrm{d}v \; W_x\left(\frac{y_1 + y_2}{2}, v\right) \exp\left[\mathrm{i}2\pi v\,(y_1 - y_2)\right]. \tag{5.5}$$

This means that the projection subset for $\alpha = 0$ contains the coherence information of any pair of points that are part of the same vertical line, i.e. they share the same x coordinate. Since the x coordinate can be freely changed for a given projection subset, the MI at any pair of points contained in a vertical line can be recovered with a single subset. In order to recover the remaining coherence information, the MI at two points that are not in the same vertical line, we need to acquire and process the rest of subsets associated with $\alpha \neq 0$.

In Sect. 1.3 we mentioned that the rotation in the xy, and hence uv, planes at angle α corresponds to the Rotator operation, which is associated with the ABCD matrix defined by Eq. (1.36),

$$\mathbf{R}^{\alpha} \equiv \mathbf{T}_{\mathbf{U}_{\mathrm{R}}^{\alpha}} = \begin{bmatrix} \cos\alpha & \sin\alpha & 0 & 0 \\ -\sin\alpha & \cos\alpha & 0 & 0 \\ 0 & 0 & \cos\alpha & \sin\alpha \\ 0 & 0 & -\sin\alpha & \cos\alpha \end{bmatrix}. \tag{5.6}$$

The beam MI is, therefore, transformed as:

$$\Gamma_{\mathbf{R}^{\alpha}}(\mathbf{r}_1, \mathbf{r}_2) = \Gamma\left(\begin{bmatrix} \cos\alpha & -\sin\alpha \\ \sin\alpha & \cos\alpha \end{bmatrix} \mathbf{r}_1, \begin{bmatrix} \cos\alpha & -\sin\alpha \\ \sin\alpha & \cos\alpha \end{bmatrix} \mathbf{r}_2\right), \tag{5.7}$$

i.e. it is rotated an angle α on the plane normal to its propagation direction. Then, the MI obtained from the subset $\alpha = \alpha_0$, Γ, is equivalent to the MI of the rotated beam, $\Gamma_{\mathbf{R}^{\alpha}}$. In other words, the MI between any two points contained in a line that spans an angle α_0 with the vertical direction can be obtained from the subset α_0 as:

$$\Gamma_{\mathbf{R}^{\alpha_0}}\left(\begin{bmatrix} x_0 \\ y_1 \end{bmatrix}, \begin{bmatrix} x_0 \\ y_2 \end{bmatrix}\right) = \Gamma\left(\begin{bmatrix} -y_1 \sin\alpha_0 + x_0 \cos\alpha_0 \\ y_1 \cos\alpha_0 + x_0 \sin\alpha_0 \end{bmatrix}, \begin{bmatrix} -y_2 \sin\alpha_0 + x_0 \cos\alpha_0 \\ y_2 \cos\alpha_0 + x_0 \sin\alpha_0 \end{bmatrix}\right), \tag{5.8}$$

It is better for visualising the results to express the MI between the light field at a fixed *reference point*, $\mathbf{r}_0 = (x_0, y_0)$, and the rest of points in the line. In this alternative coordinate frame the MI is defined as:

$$\Gamma_{\alpha_0}(\mathbf{r}_0, s) \equiv \Gamma_{\mathbf{R}^{\alpha_0}}(\mathbf{r}_0, \mathbf{r}_0 + s\mathbf{n}), \tag{5.9}$$

where s is the proper parameter of the line defined by the unitary direction $\mathbf{n} = (-\sin\alpha_0, \cos\alpha_0)$. Notice that for the special case $\alpha_0 = 0$ we recover the MI for any two points contained in the same vertical line. Therefore, although processing all subsets is required to obtain the entire coherence picture of the beam, every individual projection subset provides valuable information of the beam coherence.

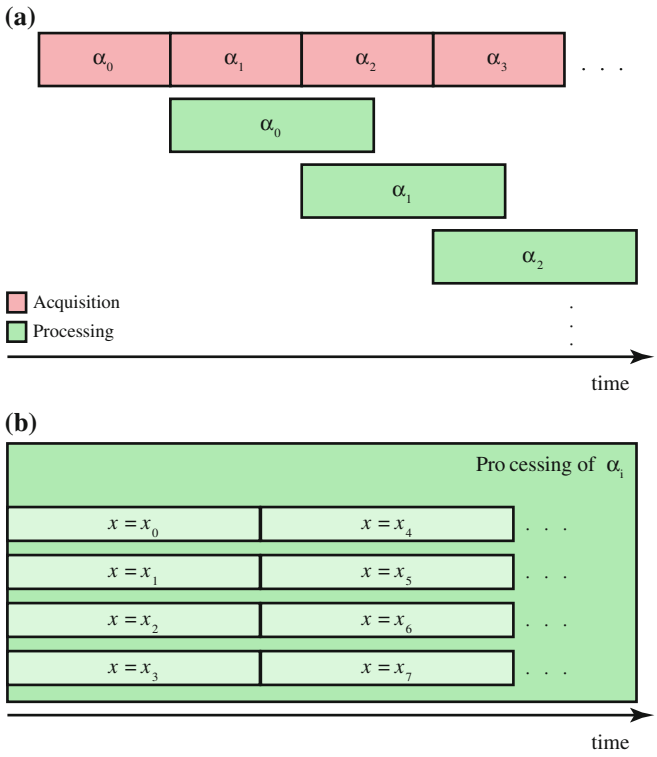

Fig. 5.2 **a** Illustration of the independence of the acquisition and processing tasks in PSTC. The processing of a projection subset is independent of the acquisition and processing of the rest of subsets. **b** Illustration of a possible parallel processing scheme to efficiently recover W_x for multiple values of x and the associated MI using a quad core computer system

The processing of a projection subset $P^{\alpha_0,\gamma}$ is independent of the acquisition and processing of the subsets for different angle α. As a consequence, all subsets can be treated in parallel, refer to Fig. 5.2a for an illustration of a possible computation scheme. In addition, the processing of a projection subset into W_x can be split into independent tasks, each one associated with a fixed value of x, see Fig. 5.2b. This permits a more efficient usage of computation systems with multiple processing units.

In the end, even though the calculation effort for the complete characterization of an arbitrary beam is similar for both PSTC and PST, our method is more appropriated to parallel processing schemes. This translates into a more efficient usage of the processing resources and a shorter end-to-end calculation time. More importantly, PSTC provides valuable information of the beam coherence after processing each subset. For these reasons we consider PSTC a significant improvement with respect to PST that paves the way to its practical application.

5.3 Experimental Setup for PSTC Realization

Both PST and PSTC can be implemented using an automatized opto-electronic setup based on the optical system proposed in [Rod09]. This *coherenscope* system permits video-rate acquisition of all the required projections for the characterization of an optical beam. A photograph and a scheme of the optical system are displayed in Figs. 5.3 and 5.4, respectively. The setup comprises two generalized lenses implemented by a twin Holoeye LC-R2500 reflective LCOS SLM device (256 grey levels, pixel pitch $d_\mathrm{p} = 19\,\mu\mathrm{m}$, and screen resolution 1024×768) and an Imaging Source DMK 41BF02 CCD camera (8-bit pixel depth, pixel pitch $4.65\,\mu\mathrm{m}$, and screen resolution 1600×1200). The distance z between any two consecutive elements is fixed. After SLM1, a half-wave plate ensures the beam polarisation is optimal for SLM2.

The projection subset $P^{0,\gamma}$ is acquired by implementing elliptical lenses in the SLMs. At the output plane of the system, where the camera is placed, the beam fractional power spectra associated with the FRFT for fixed $\gamma_x = 0$ and variable $\gamma_y = \gamma$ is measured. The transmission function implemented in the j-th SLM is described by

$$L_j^{0,\gamma}(\mathbf{r}) = \exp\left(-\frac{\mathrm{i}\pi}{\lambda \mathrm{g}_j} x^2\right) \exp\left(-\frac{\mathrm{i}\pi}{\lambda \mathrm{f}_j} y^2\right), \tag{5.10}$$

where

$$\begin{aligned} \mathrm{g}_1 &= z, & \mathrm{f}_1(\gamma) &= \frac{2z}{2 - \cot(\gamma/2)}, \\ \mathrm{g}_2 &= \frac{z}{2}, & \mathrm{f}_2(\gamma) &= \frac{z}{2 - 2\sin\gamma}. \end{aligned} \tag{5.11}$$

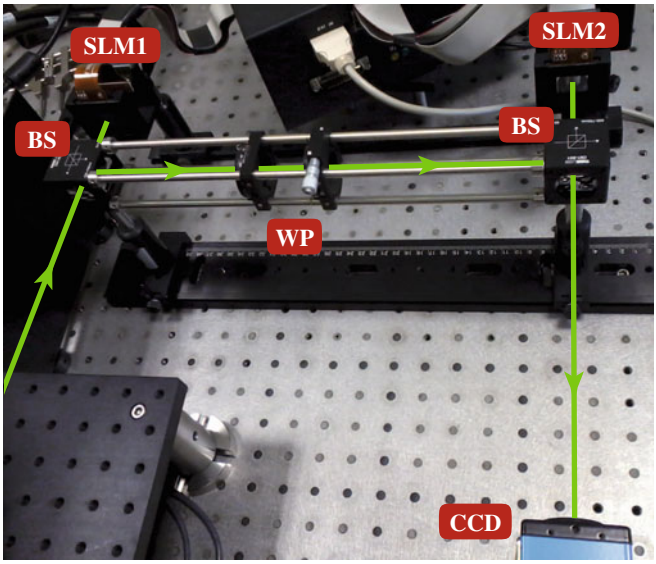

Fig. 5.3 Photo of the optical system performing the phase-space rotation of the beam

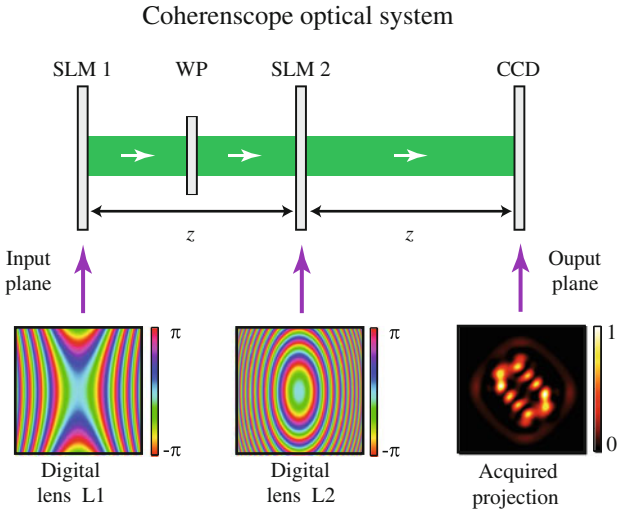

Fig. 5.4 Scheme of the optical system performing the phase-space rotation of the beam

This lens configuration is suitable for acquiring the PSTC projections for $\gamma \in [\pi/2, 3\pi/2]$ and $\alpha = 0$ or the input beam.

As we mentioned in the previous section, we need to rotate the input beam in order to obtain the projections for $\alpha \neq 0$. Fortunately, as the rotation is relative to the optical system, a rotation of the input beam for angle α is equivalent to a rotation

for opposite angle, $-\alpha$, of the SLMs and the CCD camera. Since both SLMs and the CCD camera implement or gather digital information, the transmission masks implemented in the SLM or the intensity distribution acquired by the camera, can be digitally rotated. As a result, the actual transmission function of j-th SLM is described by

$$L_j^{\alpha,\gamma}(\mathbf{r}) = \exp\left[-\frac{\mathrm{i}\pi}{\lambda \mathrm{g}_j}(x\cos\alpha - y\sin\alpha)^2\right] \times \exp\left[-\frac{\mathrm{i}\pi}{\lambda \mathrm{f}_j(\gamma)}(x\sin\alpha + y\cos\alpha)^2\right]. \tag{5.12}$$

In order to demonstrate the experimental feasibility of the proposed method we need to generate beams with controlled state of coherence. Due to its versatility we employ a technique similar to the CGH method explained in Sect. 2.2. The major difference is that the reference beam is now a Schell-model beam (SMB) with uniform intensity. The SMB is generated from a fundamental Gaussian beam emitted by a laser source ($\lambda = 532$ nm, 50 mW power) using a rotating ground-glass (RGG) diffuser.

The beam-generation optical system is presented in Fig. 5.5. A Gaussian beam traverses a RGG diffuser placed near the front and back focal planes of the focusing (FL, NBK-7 glass convergent lens of focal length 0.05 m) and collimating lenses (CL,

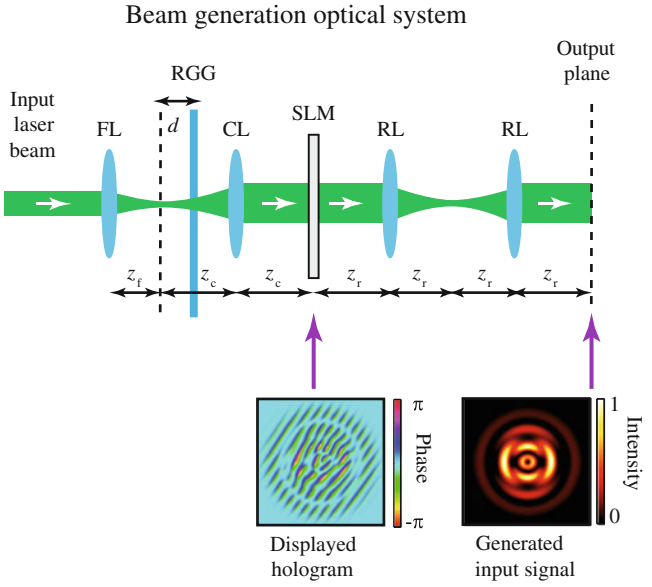

Fig. 5.5 Scheme of the optical system that transforms a Gaussian beam into a partially coherent beam with Gaussian degree of coherence

NBK-7 glass convergent lens of focal length 0.25 m), correspondingly. The RGG is a diffuser (Thorlabs DG20-120-MD, 120 grit polished) embedded in a custom-made mount that rotates at 60 rpm. The beam emerging from the diffuser maintains its Gaussian intensity profile, but it is completely incoherent. According to the Van Cittert-Zernike theorem [Goo00, Bor06], during its propagation from the RGG plane to the SLM plane, the beam acquires a certain degree of coherence that is proportional to the FT of its intensity distribution at the diffuser plane. The resulting beam is described by the MI

$$\Gamma_d\left(\mathbf{r}_1,\mathbf{r}_2\right)=I_0\exp\left[-\frac{\pi w^2}{2\left(\lambda \mathrm{f_c}\right)^2}\left(\mathbf{r}_1-\mathbf{r}_2\right)^2+\frac{\mathrm{i}\pi d}{\lambda \mathrm{f_c}^2}\left(\mathbf{r}_1^2-\mathbf{r}_2^2\right)\right], \tag{5.13}$$

where w and λ are the waist and wavelength of the Gaussian beam just after the RGG diffuser, I_0 a energy normalising constant, $\mathrm{f_c}$ is the focal length of CL, and d is the displacement of the diffuser with respect to the Fourier plane of FL. Refer to Sect. 5.8 for a full derivation of Eq. (5.13). At the SLM plane the beam has uniform intensity distribution:

$$I\left(\mathbf{r}\right)=I_0, \tag{5.14}$$

and Gaussian degree of coherence modulus:

$$\left|\gamma\left(\mathbf{r}_1,\mathbf{r}_2\right)\right|=\exp\left[-\frac{\pi w}{2\lambda^2 \mathrm{f}^2}\left(\mathbf{r}_1-\mathbf{r}_2\right)^2\right]. \tag{5.15}$$

The beam waist w increases with the distance d between the diffuser and the back focal plane of FL. Therefore, the beam coherence degree decreases as the distance d increases.

Finally, the partially coherent beam incident to the Holoeye PLUTO SLM (255 gray-levels, pixel pitch 8 μm, and screen resolution 1920 × 1080) is further transformed by a CGH as it is explained in Sect. 2.2:

$$\Gamma\left(\mathbf{r}_1,\mathbf{r}_2\right)=\Gamma_{\mathrm{c}}\left(\mathbf{r}_1,\mathbf{r}_2\right)\Gamma_d\left(\mathbf{r}_1,\mathbf{r}_2\right), \tag{5.16}$$

with $\Gamma_{\mathrm{c}}(\mathbf{r}_1,\mathbf{r}_2)=f(\mathbf{r}_1)f^*(\mathbf{r}_2)$, being f the complex amplitude encoded by the CGH. The resulting beam is imaged into the input plane of the phase-space rotation optical system of Fig. 5.4 by the relay lenses RL (NBK-7 glass convergent lenses of focal length 0.25 m).

This optical system allows generating beams with Gaussian degree of coherence. In addition, removing the RGG diffuser from the system results in a setup suitable for coherent computer-generated holography, as explained in Sect. 2.2. It permits generating:

- completely coherent beams with arbitrary spatial structure, or
- partially coherent beams with non-Gaussian degree of coherence composed as incoherent superposition of orthogonal modes by time multiplexing, refer to [Ali13] and Eq. (1.4).

Coherent beams generated with this optical system are used in the following Sect. 5.4 to validate the results obtained with PSTC. The two kinds of partially coherent beams—with Gaussian and non-Gaussian degree of coherence—are used in Sect. 5.5 to assert the experimental feasibility of PSTC as a coherence characterization technique.

5.4 Characterization of Coherent Beams

The aim of this section is to experimentally validate PSTC as a characterization technique by comparing the results obtained by PSTC and by an alternative method. Since the two experiments use the same input optical beam, we avoid discrepancies caused by errors on the beam generation process. Additionally, for this initial validation we use completely coherent beams because it allows us selecting an alternative characterization method that is well-established and trusted.

The alternative characterization method is an iterative phase retrieval (IPR) approach based on the well-known Gerchberg-Saxton iterative algorithm [Ger72]. This IPR technique, proposed in [Rod11], allows recovering the phase distribution of a coherent beam from several of its fractional power spectra, $S_m \equiv S^{\gamma_{x,m},\gamma_{y,m}}$ with $m = 1, 2, \ldots, M$. The measured S_m plays the role of a constraint image. A diagram of the algorithm is displayed in Fig. 5.6. There are two iteration loops indicated by indices k and m ($k = 1, \ldots, K$ and $m = 1, \ldots, M$) one inside of the other. The total number of iterations is $M \times K$. The complex field amplitude at iteration k and m is denoted by $f_{k,m}$.

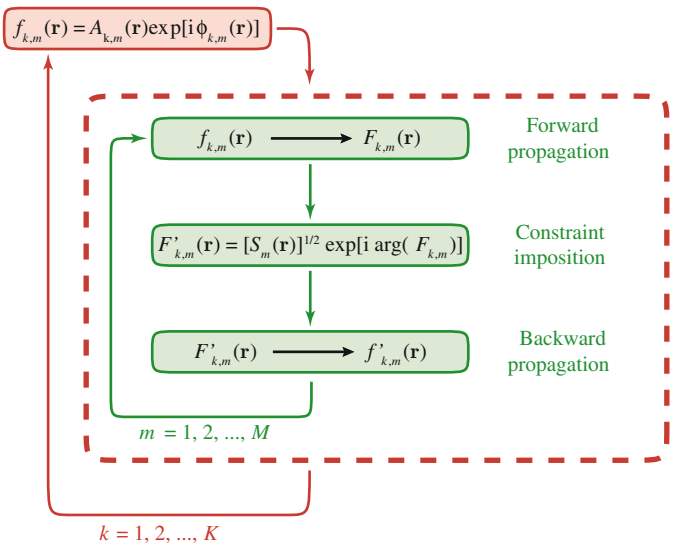

Fig. 5.6 Diagram of the IPR algorithm used as alternative method for coherent beam characterization

The process starts with an initial guess of complex amplitude $f_{1,1}$. During the k-th iteration it converts an input complex amplitude, $f_{k,1}(\mathbf{r}) = A_0(\mathbf{r})\exp[\mathrm{i}\phi_k(\mathbf{r})]$,[2] into an output amplitude, $f_{k+1,1}$. To obtain the output amplitude it performs the following steps on $f_{k,m}$ for each measured constrain S_m:

1. Transform the current amplitude, $f_{k,m}$, using the FRFT kernel associated with the matrix, $\mathbf{T}_{\mathrm{F},m} \equiv \mathbf{T}_{\mathrm{F}}^{\gamma_{x,m},\gamma_{y,m}}$:

$$f_{k,m}(\mathbf{r}) \xrightarrow{\mathbf{T}_{\mathrm{F},m}} F_{k,m}(\mathbf{r}) = A_{k,m}(\mathbf{r})\exp\left[\mathrm{i}\phi_{m,k}(\mathbf{r})\right]. \tag{5.17}$$

   For the first constraint use the iteration guess amplitude, $f_{k,1} = f_k$.
2. Impose the measured intensity distribution to the result:

$$F_{k,m}(\mathbf{r}) \to F'_{k,m}(\mathbf{r}) = [S_m(\mathbf{r})]^{1/2}\exp\left[\mathrm{i}\phi_{m,k}(\mathbf{r})\right]. \tag{5.18}$$

3. Transform the result using the inverse FRFT transform associated with the constraint:

$$F'_{k,m}(\mathbf{r}) \xrightarrow{(\mathbf{T}_{\mathrm{F},m})^{-1}} f'_{k,m}(\mathbf{r}). \tag{5.19}$$

4. Replace the resulting phase distribution in the amplitude for the next m iteration:

$$f_{k,m+1}(\mathbf{r}) = A_0(\mathbf{r})\exp\left\{\mathrm{i}\arg\left[f'_{k,m}(\mathbf{r})\right]\right\}. \tag{5.20}$$

The result from M iterations over m is used as guess for the next iteration over k: $f_{k+1,1} = f_{k,M}$. A complex amplitude formed by the beam intensity distribution and a random phase distribution is usually chosen as initial guess, $f_{1,1}$. If the constraints provide sufficient information of the beam, the resulting complex amplitude from each passing iteration converges to the complex amplitude of the experimental beam. Convergence is usually achieved by measuring several symmetrical and one antisymmetrical fractional power spectra.

The generated coherent beam is described by a complex amplitude composed by the superposition of two LG beams, refer to Eq. (1.7):

$$f(\mathbf{r}) = \frac{1}{\sqrt{2}}\left[\mathscr{L}_0^3(\mathbf{r}) + \mathscr{L}_4^1(\mathbf{r})\right], \tag{5.21}$$

with waist $w = 0.73$ mm. It is generated using the optical system illustrated in Fig. 5.5 by removing the RGG diffuser and implementing the CGH displayed in Fig. 5.7. Notice that the high-frequency oscillations in the CGH are due to the carrier that separates the signal in the Fourier plane of the relay lenses. See Sect. 2.2, in particular Eq. (2.10).

The theoretical intensity and phase distributions of the resulting beam are presented in Fig. 5.8a, c, respectively. Correspondingly, the acquired intensity

[2] Notice that A_0 is the amplitude of the beam, i.e. the squared root of its intensity distribution.

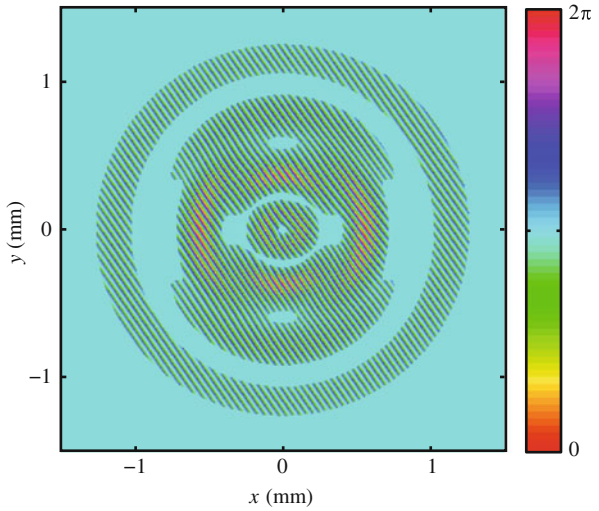

Fig. 5.7 Phase mask of the CGH used to generate the coherent beam for PSTC validation

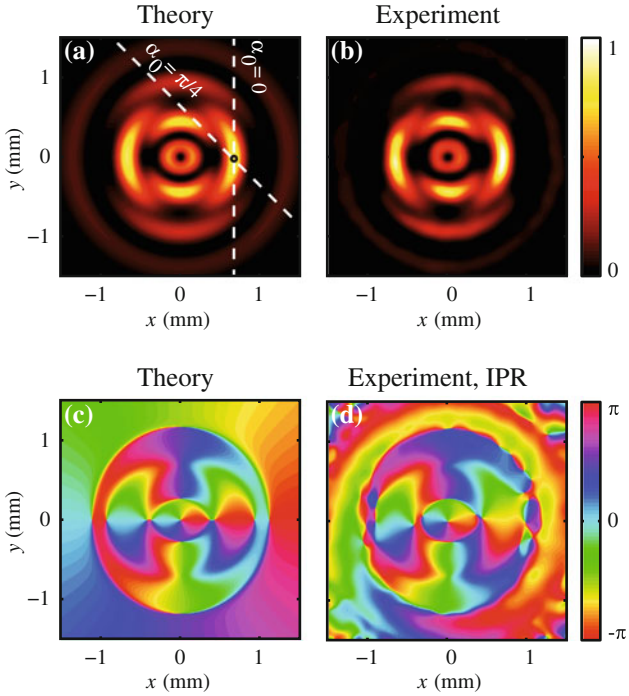

Fig. 5.8 **a** Theoretical and **b** experimental intensity distributions of the generated beam. **c** Theoretical and **d** experimentally retrieved phase distributions of the generated beam

distribution and experimentally retrieved phase distributions of the generated beam are presented in Fig. 5.8b, d. Comparing the theoretical expectations with the experimental results we can perceive significant differences in the intensity distribution, specially at the outer region of the beam. This discrepancy is due to the non-uniformity of the CGH reference beam, which translates in an uneven power distribution. Similar differences are also observed for the phase distribution. These differences are the main reason for validating the experimental results of PSTC against an alternative characterization technique: uncontrollable noise produced in the beam generation process affects equally to both experimental methods, while theoretical predictions do not have into account these factors.

In order to apply PSTC to the same test beam, we acquire two projection subsets $P^{\alpha_0,\gamma}$ associated with $\alpha_0 = 0$ and $\alpha_0 = \pi/4$, each one formed by 180 intensity distributions for equidistant γ in the range $[\pi/2, 3\pi/2)$. The modulus and phase of the MI $\Gamma_{\alpha_0}(\mathbf{r}_0, s)$ obtained from the subset $\alpha_0 = 0$ at the region of interest $s \in [-1.1, 1.1]$ mm for multiple reference points $\mathbf{r}_0 = (x_0, 0)$ with $x_0 \in (0.4, 0.7)$ mm are presented in Fig. 5.9a, c, respectively. To compare these results with IPR, we convert the recovered IPR complex amplitudes into their corresponding MI via $\Gamma(\mathbf{r}_1, \mathbf{r}_2) = f(\mathbf{r}_1) f^*(\mathbf{r}_2)$. The modulus and phase of the resulting MI are presented in Fig. 5.9b, d, respectively.

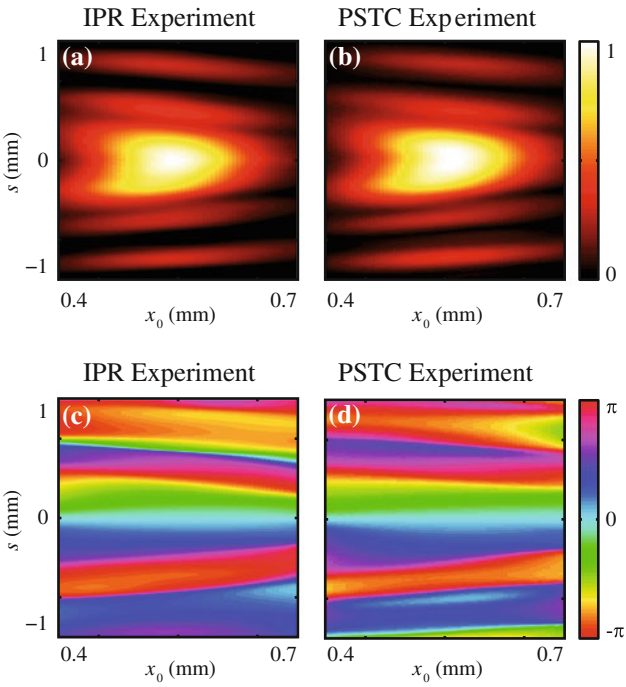

Fig. 5.9 Modulus of the MI $\Gamma_{\alpha_0}(\mathbf{r}_0, s)$ for $\alpha_0 = 0$ and $\mathbf{r}_0 = (0.6, 0)$ mm obtained from **a** IPR and **b** PSTC. Phase of the MI $\Gamma_{\alpha_0}(\mathbf{r}_0, s)$ for $\alpha_0 = 0$ and $\mathbf{r}_0 = (0.6, 0)$ mm obtained from **a** IPR and **b** PSTC

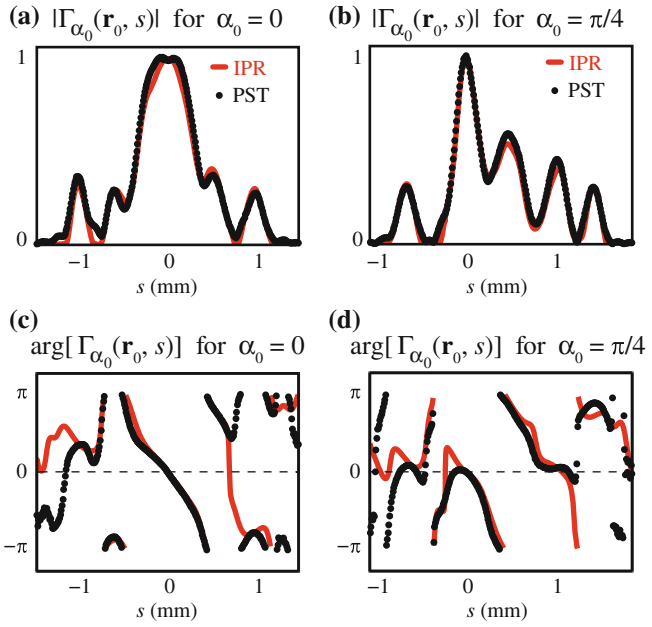

Fig. 5.10 **a** Modulus and **c** phase of $\Gamma_{\alpha_0}(\mathbf{r}_0, s)$ for $\alpha_0 = 0$ and $\mathbf{r}_0 = (0.6, 0)$ mm obtained from (*red line*) IPR and (*black dots*) PSTC methods. **b** Modulus and **d** phase of $\Gamma_{\alpha_0}(\mathbf{r}_0, s)$ for $\alpha_0 = \pi/4$ and $\mathbf{r}_0 = (0.6, 0)$ mm obtained from (*red line*) IPR and (*black point*) PSTC methods

Figure 5.9 gives us a qualitative idea of how similar are the results obtained from both independent experimental methods. Notice that the MI phase recovered from PSTC agrees with the one recovered from IPR. That is especially true at the points close to the central lobe, where most of the power is concentrated. In contrast, at the regions with less power, for example around $s \sim \pm 0.85$ mm, the discrepancies are bigger. This is expected since the measurement and calculation errors are more significant in the areas with low power.

To have a more precise notion of how similar are the MI recovered by both methods, we compare in Fig. 5.10 the 1D MI $\Gamma_{\alpha_0}(\mathbf{r}_0, s)$ with fixed reference point $\mathbf{r}_0 = (0.6, 0)$ mm for $\alpha_0 = 0$ and $\alpha_0 = \pi/4$. These 1D *profiles* correspond to the MI between the reference point marked with a black circle in Fig. 5.8a and the rest of points of the white dashed lines. The modulus of both MI are considerably similar, with some minor discrepancies around $s = -1$ mm on the $\alpha_0 = 0$ case. There are more differences on the MI phase. For instance, we observe significant disagreement in the region around $|s| \sim 1$ mm for both $\alpha_0 = 0$ and $\alpha_0 = \pi/4$. Nevertheless, both methods coincide for the regions with relatively large MI amplitude, around $s = 0$ for both α.

Although the MIs resulting from both methods diverge at certain points where the signal to noise ratio is low, they generally coincide outside of these regions. The comparison between both methods validates the results obtained with PSTC,

demonstrating that the recovered MI corresponds to what is expected. These experiments, however, do not justify the application of PSTC for characterization of coherent beams, which have less degrees of freedom compared to partially coherent beams, since the IPR method is faster and requires less experimental measurements. The strength of PSTC becomes evident in the following section, where partially coherent beams are successfully characterized.

5.5 Characterization of Partially Coherent Beams

PSTC is a coherence-agnostic technique: it can be applied to beams with arbitrary degree of coherence. In this section we experimentally demonstrate that PSTC is an efficient method to characterize the spatial structure of a partially coherent beam. Partially coherent beams are generated using two different techniques: CGH with partially coherent reference beam, and incoherent sum of orthogonal modes. Due to the difficulty of experimentally obtaining the coherence picture of the beams with an alternative method, we will compare the results with the theoretical predictions. Notice that, as explained in the previous section, we expect some differences between theoretical and experimental results produced by uncontrollable noise in the beam generation optical system.

Partially Coherent Beams Generated with CGH

Partially coherent beams with Gaussian degree of coherence are generated using the optical system displayed in Fig. 5.5. At the output plane of the beam-generating system, on the forward focal plane of the second relay lens, we obtain the MI of the beam encoded in the CGH, Γ_c, multiplied by the MI of the GSMB, c.f. Eq. (5.16),

$$\Gamma\left(\mathbf{r}_1, \mathbf{r}_2\right) = \Gamma_c\left(\mathbf{r}_1, \mathbf{r}_2\right) \Gamma_d\left(\mathbf{r}_1, \mathbf{r}_2\right). \tag{5.22}$$

For these experiments we use the same CGH as for the experiments of the previous section in order to analyze the differences appearing by the partially coherent beam illumination. As a consequence, according to Eq. (5.21),

$$\Gamma_c\left(\mathbf{r}_1, \mathbf{r}_2\right) = \frac{1}{2}\left[\mathscr{L}_0^3\left(\mathbf{r}_1\right) + \mathscr{L}_4^1\left(\mathbf{r}_1\right)\right]\left[\mathscr{L}_0^3\left(\mathbf{r}_2\right) + \mathscr{L}_4^1\left(\mathbf{r}_2\right)\right]^*. \tag{5.23}$$

The width of the Gaussian degree of coherence is controlled by the width of the beam incident to the RGG diffuser, which in turn is controlled by the distance d between the RGG diffuser and the back-focal plane of the collimating lens of the optical system, refer to Fig. 5.5. Therefore, the parameter d defines the degree of coherence of the generated beam. Several values of this parameter, $d = 0$, 14, 28, 52 mm, have been considered in the experiment. Fig. 5.11a shows the intensity distributions measured at the diffuser plane in each case. The Gaussian widths are estimated by fitting a Gaussian function to the x and y projections of the intensity

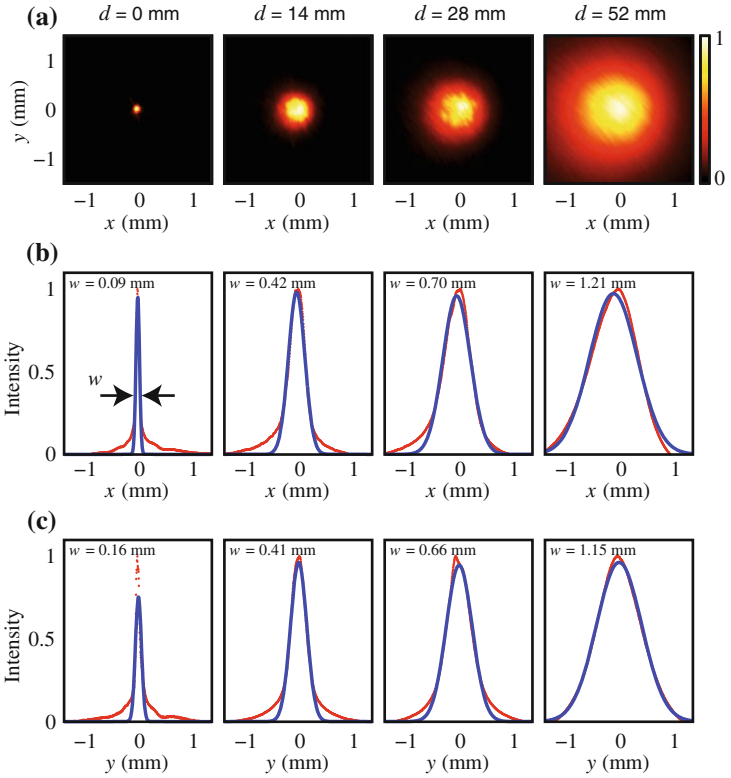

Fig. 5.11 **a** Intensity distribution of the beam at different distances d from the *back-focal plane* of the collimating lens CL of Fig. 5.5. **b** y and **c** x projection of (*red line*) the intensity distribution and (*blue line*) the best fitting Gaussian function found by least squares method

Table 5.1 Summary of Gaussian widths—x/y profiles and mean—of the beam measured at different distances d from the back-focal plane of the collimating lens CL of Fig. 5.5

d (mm)	w_x (mm)	w_y (mm)	w (mm)
0	0.09	0.16	0.125
14	0.42	0.41	0.415
28	0.70	0.66	0.68
52	1.21	1.15	1.18

using least squares method. The projections and their corresponding fitting function are displayed in Fig. 5.11b, c. The final Gaussian widths, used for calculating the theoretical predictions of the resulting degree of coherence, are calculated as the mean width from x and y projections. They are summarized in Table 5.1.

The intensity distribution of the coherent beam used in the previous section and the generated beams at the output plane of the beam-generation optical system for

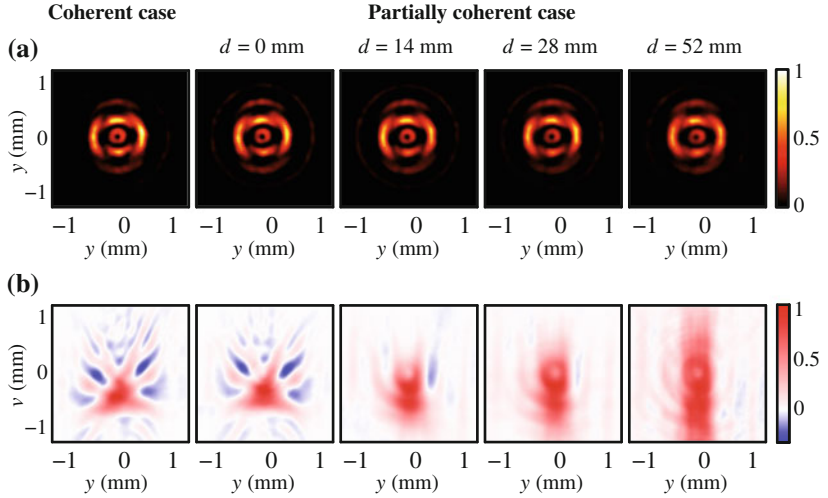

Fig. 5.12 **a** Intensity distribution of the beam measured at the output plane of the beam-generation optical system for different degrees of coherence controlled by the distance d. **b** $W_{x_0}(y, v)$ with $x_0 = 0.6$ mm for each one of the generated beams

each value of the distance d are presented in Fig. 5.12a. Notice that regarding its intensity distribution, one can think that all of them correspond to the same beam. Applying PSTC we can demonstrate that the beams are profoundly different as their degrees of coherence diverge.

A total of 180 projections $S^{\alpha_0,\gamma}$ for $\alpha_0 = 0$ and γ ranging in $[\pi/2, 3\pi/2)$ were measured using the setup discussed in Sect. 5.3 and the WD distributions W_{x_0} were reconstructed following the PSTC method. Figure 5.12b shows the WD of the 1D signal, $W_{x_0}(y, v)$ with $x_0 = 0.6$ mm, reconstructed for each beam from their corresponding projection subsets. The most coherent beams—the coherent case and the partially coherent case for $d = 0$ mm—present a similar WD. This is expected since the Gaussian function describing the modulus of the degree of coherence for $d = 0$ is quite broad. As the degree of coherence decreases, i.e. d increases, the WD structure, with clearly distinguishable blue regions where the WD is negative, is gradually washed out. The W_{x_0} associated with the most incoherent case, $d = 52$ mm, is almost independent of the frequency coordinate, v. This behaviour is typical for incoherent beams as it has been illustrated in Fig. 1.3.

So far we can conclude that, although all beams posses the same intensity distribution, by reconstructing their WD W_{x_0} we have revealed that their coherence picture is different. In order to quantize their state of coherence we further reconstruct the MIs corresponding to the recovered W_{x_0}, i.e. the MI $\Gamma_{\alpha_0}(\mathbf{r}_0, s)$ for $\alpha_0 = 0$ between the reference point $\mathbf{r}_0 = (0.6, 0)$ mm and the rest of points in the same vertical line. These results are displayed in Fig. 5.13.

We observe that, analogously to the WD details, the side lobes of the MI amplitude profiles disappear when the coherence decreases, see Fig. 5.13a. The phase of the MI

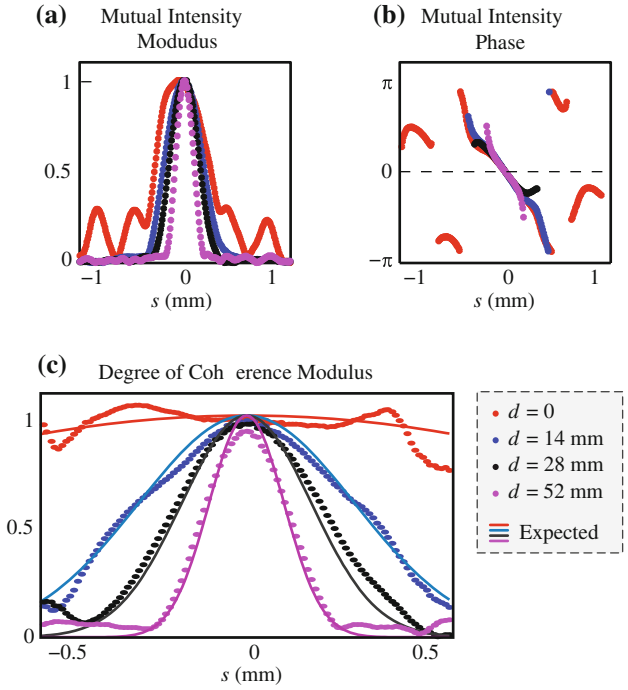

Fig. 5.13 **a** Modulus and **b** phase corresponding to $\Gamma_{\alpha_0}(\mathbf{r}_0, s)$ with $\alpha_0 = 0$ and $\mathbf{r}_0 = (0.6, 0)$ mm for the generated partially coherent beams associated with distances $d = 0$, 14, 28, and 52 mm. **c** Degree of coherence modulus of each (*circle*) experimental beam compared with their corresponding (*solid line*) theoretical expectation

profiles are displayed in Fig. 5.13b. Notice that only the phase values corresponding to points where the intensity is greater than 5 % of the total beam power are presented to avoid confusion due to noise. All four phase curves overlap in the area around $s = 0$ mm. We can also recover the modulus of the degree of coherence and compare it to the theoretical expectation according to Eq. (5.15) and the experimentally defined values of w (remember Fig. 5.11 and Table 5.1.) A good agreement between the experimentally-obtained and theoretical degrees of coherence that are presented in Fig. 5.13c is observed.

As a final control experiment we recover the degree of coherence modulus corresponding to $\Gamma_{\alpha_0}(\mathbf{r}_0, s)$, that is $|\gamma_{\alpha_0}(\mathbf{r}_0, s)|$, for the same reference point but different angles. Since all our generated beams posses a Gaussian degree of coherence modulus that only depends on the distance between the reference point and the observation point, $|s|$, we must observe that the degree of coherence is independent of the angle α_0. In Fig. 5.14a, b we show the MI profiles and modulus of the degrees of coherence, respectively, for $\mathbf{r}_0 = (0.6, 0)$ mm and angles $\alpha_0 = 0$ and $\pi/4$. While the MI profiles are significantly different, the degrees of coherence share the common Gaussian shape of the theoretical expectation, represented by a solid black line.

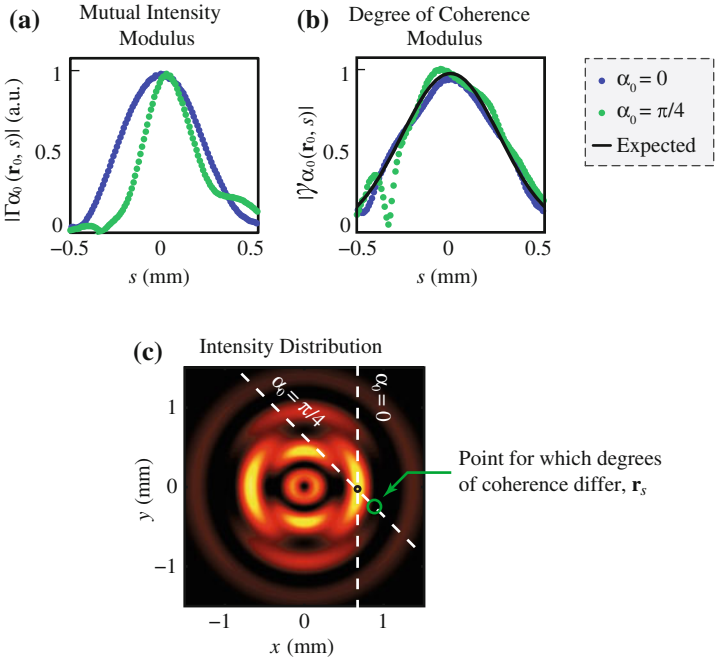

Fig. 5.14 **a** MI profile $\Gamma_{\alpha_0}(\mathbf{r}_0, s)$ and **b** its associated degree of coherence, $|\gamma_{\alpha_0}(\mathbf{r}_0, s)|$, obtained for the $d = 14$ mm experimental beam where $\mathbf{r}_0 = (0.6, 0)$ mm and $\alpha_0 = 0, \pi/4$. **c** Intensity distribution of the generated beam

There is a clear discrepancy in the degree of coherence around the point $s = -0.4$ mm, where $|\gamma_{\pi/4}|$ reaches zero. This happens because the beam at that particular point $\mathbf{r}_s$ associated with $s \sim -0.4$ mm has zero intensity, and, hence, the degree of coherence is undefined. The fact that the beam has null intensity at that point can be concluded from two different results. Firstly, in Fig. 5.14a we observe that the MI profile is zero around the discrepancy point. That could potentially mean that there is no correlation between the beam at the points $\mathbf{r}_0$ and $\mathbf{r}_s$. However, checking the beam intensity distribution we find that there is no intensity at point $\mathbf{r}_s$, identified by a green circle in Fig. 5.14c.

As a summary for this section we can conclude that PSTC allows revealing the coherence picture of partially coherent beams with Gaussian modulus of the degree of coherence. In particular, it distinguishes between the experimental beams of Fig. 5.12 which have the same intensity distribution but different degrees of coherence. Although there are discrepancies at the regions where the beam intensity is comparable to the noise level, the general behaviour of the technique is satisfactory and the results correspond to the theoretical expectations.

Partially Coherent Beams Generated by Time Multiplexing of Modes

To close this section we apply PSTC to more general partially coherent beams. These are generated by incoherent sum of orthogonal modes as explained in Sect. 1.1. These beams are specially interesting for optical communications [Wan12] since each mode can represent a independent channel to encode information.

We use LG beams as orthogonal modes. Hence, the MI of the beams that can be generated is described by:

$$\Gamma\left(\mathbf{r}_1, \mathbf{r}_2\right) = \sum_{p,l} a_{p,l} \mathscr{L}_p^l\left(\mathbf{r}_1\right) \left[\mathscr{L}_p^l\left(\mathbf{r}_2\right)\right]^*, \tag{5.24}$$

being $a_{p,l}$ the sum coefficient of the LG mode associated with p and l, refer to Eq. (1.4). Remember that the sum of all coefficients should equal one, $\sum_{p,l} a_{p,l} = 1$, so the generated beam is normalised.

Beams composed by incoherent sum of orthogonal modes posses useful properties for its experimental characterization. For example, the fractional power spectra of the generated beam, being intensity measurements, are equivalent to the sum of fractional power spectra of the composing modes. Similarly, the PSTC projections of the generated beam are equivalent to the incoherent sum of projections for the composing LG modes:

$$S^{\alpha_0,\gamma}\left(\mathbf{r}\right) = \sum_{p,l} a_{p,l} S_{p,l}^{\alpha_0,\gamma}\left(\mathbf{r}\right), \tag{5.25}$$

where $S_{p,l}^{\alpha_0,\gamma}$ is the PSTC projection for angles α_0 and γ of the LG mode with indices p and l. Therefore, we can experimentally obtain the PSTC projections of the generated beam by:

1. Measuring the PSTC projections of completely coherent LG modes following the instructions in Sect. 5.4
2. Summing the normalised PSTC projections for each composing LG mode according to its corresponding coefficient $a_{p,l}$.

According to these instructions, we measured 180 projections of the subset $S^{\alpha_0,\gamma}$ with $\alpha_0 = 0$ and γ ranging in $[\pi/2, 3\pi/2)$ for two different beams described by their MIs

$$\Gamma_{\mathrm{A}}\left(\mathbf{r}_1, \mathbf{r}_2\right) = \frac{1}{2}\left[\Gamma_0^3\left(\mathbf{r}_1, \mathbf{r}_2\right) + \Gamma_4^1\left(\mathbf{r}_1, \mathbf{r}_2\right)\right], \tag{5.26}$$

$$\Gamma_{\mathrm{B}}\left(\mathbf{r}_1, \mathbf{r}_2\right) = \frac{1}{4}\left[3\Gamma_0^3\left(\mathbf{r}_1, \mathbf{r}_2\right) + \Gamma_4^1\left(\mathbf{r}_1, \mathbf{r}_2\right)\right], \tag{5.27}$$

where Γ_p^l stands for the MI of the coherent LG mode with indices p and l. In terms of the level of coherence, which is defined in Sect. 1.1 and in this case it adopts the form

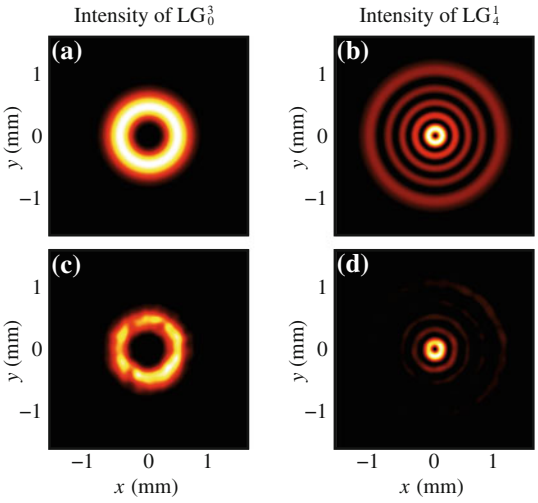

Fig. 5.15 **a** Theoretical and **c** experimental intensity distribution of $\mathscr{L}_0^3$. **b** Theoretical and **d** experimental intensity distribution of $\mathscr{L}_4^1$

$$\mu^2 = \sum_{p,l} a_{p,l}^2, \tag{5.28}$$

the beam A has a lower level of coherence, $\mu_A = \sqrt{8}/4$, than the beam B, $\mu_B = \sqrt{10}/4$. Their intensity distributions are displayed in Fig. 5.15. We recovered the degree of coherence $\gamma_{\alpha_0}(\mathbf{r}_1, s)$ with $\mathbf{r}_1 = (x_1, 0) = (0.12, 0)$ mm from the PSTC projections. The experimentally obtained (dashed coloured lines) and theoretically estimated (solid black lines) modulus of the degree of coherence for each beam are compared in Fig. 5.16a, b.

Notice that the degree of coherence modulus for both beams has a central lobe with value around unity, demonstrating that they are completely coherent around the point $(x_0, 0)$. The field at the points corresponding to the sides lobes, however, is less coherent respect to the field at the reference point $(x_0, 0)$. Moreover, the sides lobes for Γ_A are lower than for the Γ_B. These observations fit well to the theoretical expectations, except for some areas in which discrepancies are evident. We justify these differences by the inhomogeneity of the intensity distributions of the modes composing the generated beams, see Fig. 5.15.

The degree of coherence of a partially coherent beam generated by incoherent sum of orthogonal modes is governed by the the intensity and phase distributions of the composing modes. Let us illustrate this fact using the recovered degree of coherence for beam A at two different reference points. Figure 5.17c displays the modulus of the degree of coherence for beam A at the reference points: $\mathbf{r}_1 = (0.12, 0)$ mm represented in red, and $\mathbf{r}_2 = (0.35, 0)$ mm represented in green. The vertical intensity profiles of the composing modes for beam A centred at reference points $\mathbf{r}_1$ and $\mathbf{r}_2$ are shown in Fig. 5.17b, d, respectively. That way, Fig. 5.17 allows easily investigating the degree of coherent of beam A and the corresponding contributions of each composing mode.

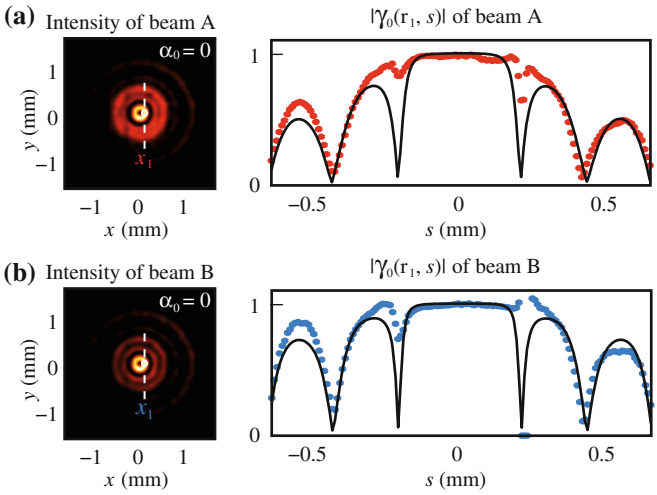

Fig. 5.16 **a** Intensity distribution and degree of coherence modulus associated to beam A for $|\gamma_{\alpha_0}(\mathbf{r}_1, s)|$ with $\alpha_0 = 0$ and $\mathbf{r}_1 = (x_1, 0) = (0.12, 0)$ mm. **b** Intensity distribution and degree of coherence modulus associated to beam B for the same $|\gamma_{\alpha_0}(\mathbf{r}_1, s)|$

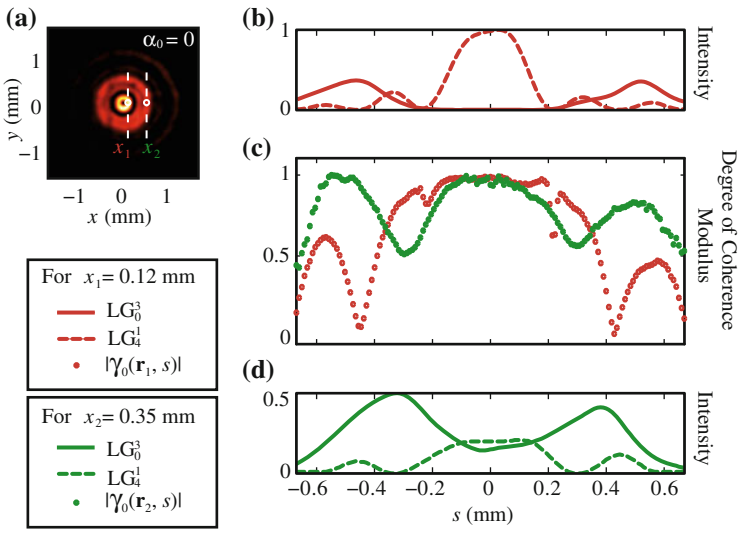

Fig. 5.17 **a** Intensity distribution of beam A. White dashed lines represent the points for which the degree of coherence is obtained. Intensity profiles associated with reference points **b** $\mathbf{r}_1 = (x_1, 0) = (0.12, 0)$ mm and **d** $\mathbf{r}_2 = (x_2, 0) = (0.35, 0)$ mm for the (*solid*) $\mathscr{L}_0^3$ and (*dashed*) $\mathscr{L}_4^1$ modes. Notice the reduced scale for the intensity of reference point $\mathbf{r}_2$ due a smaller relative energy respect to the profile for $\mathbf{r}_1$. **c** Modulus of the degree of coherence for beam A associated to reference points (*red*) $\mathbf{r}_1$ and (*green*) $\mathbf{r}_2$

On the first hand, consider the degree of coherence modulus for reference point $\mathbf{r}_1$ that is represented by red colour in Fig. 5.17c. Since around $s \sim 0$ the contribution of beam $\mathscr{L}_0^3$ is minimal, check solid line of Fig. 5.17b, the degree of coherence is only governed by $\mathscr{L}_4^1$, which is a coherent beam. Contrarily, around $|s| \sim 0.4$ mm the contribution of $\mathscr{L}_4^1$ is almost nonexistent. Since both composing modes are incoherent respect to each other, in that region the degree of coherence vanishes. That is, there are no correlations between the field at the reference point, where the major contribution is due to $\mathscr{L}_4^1$, and at the point associated with $|s| \sim 0.4$ mm, where the major contribution is due to $\mathscr{L}_0^3$.

On the other hand, consider the degree of coherence modulus for reference point $\mathbf{r}_2$ that is represented by green colour in Fig. 5.17c. In this case, both composing modes contribute significantly. Therefore, the analysis is not so straightforward as in the previous example. Nevertheless, a decrease of coherence degree can be observed around $|s| \sim 0.3$ mm. This is expected since the contribution by $\mathscr{L}_4^1$ is minimal and by $\mathscr{L}_4^1$ maximal. There cannot be much more inferred from Fig. 5.17c, because the phase distributions of the composing modes significantly affect the degree of coherence for the rest of points.

In this final experiment, we have analyzed in depth the degree of coherence of a partially coherent beam recovered using PSTC. The beam is generated by incoherent sum of orthogonal LG modes. We have observed that the degree of coherence of beams generated this way is more complex than for beams generated in the previous section using CGH. From the coherence analysis we have concluded that in some simple situations the degree of coherence depends on the intensity contributions of the beam composing modes. In more convoluted situations, the intensity information of the composing modes is not sufficient to predict the coherence behaviour of the beam.

5.6 Conclusions

The experiments considered in this chapter verify the suitability of PSTC for the quantitative and comprehensive study of completely and partially coherent optical fields. The technique offers diverse tools for the analysis of the beam spatial structure, including its MI, degree of coherence, and WD. In contrast to other methods, PSTC not only provides the modulus of the MI and the degree of coherence, but also their phases. This paves the way for the application of partially coherent light in imaging of weakly absorbing specimens [Dub99, Kol10]. In addition, the beam WD is invaluable for the design and characterization of optical systems, structurally stable beams, and spatially non-stationary fields [Alo11].

The optical system used for PSTC application is robust and allows the measurement of a broad diversity of WD projections. As future improvements, the replacement of the SLM devices by deformable mirrors [Nat11] or liquid lenses [Kui04] can be investigated to check if faster projection measurement can be achieved. Moreover, executing the algorithm in a general-purpose graphical compute unit (GPGPU) will certainly speed up the beam MI reconstruction since the whole PSTC characterization process is highly sensitive to concurrency.

Most of these results are published in [Cám13a] and were presented at the congresses [Cám10b, Cám10a, Cám11a, Cám12a, Cám13b].

Appendices

5.7 MI Reconstruction from Projection Subset for $\alpha = 0$

This section demonstrates the relation between the PSTC projection subset associated with $\alpha = 0$ and the beam MI. Consider the relation between the fractional power spectra and the beam WD projections established in Eqs. (1.52) and (1.54), i.e.[3]

$$S^{\gamma_x,\gamma_y}(\mathbf{r}) = \int \mathrm{d}\mathbf{p}\; W\left(\mathbf{r}', \mathbf{p}'\right), \tag{5.29}$$

where the primed variables $\mathbf{r}'$ are related to the non-primed ones via the FRFT phase-space rotation:

$$\begin{bmatrix} x' \\ u' \end{bmatrix} = \begin{bmatrix} \cos\gamma_x & -\sin\gamma_x \\ \sin\gamma_x & \cos\gamma_x \end{bmatrix} \begin{bmatrix} x \\ u \end{bmatrix}, \tag{5.30}$$

$$\begin{bmatrix} y' \\ v' \end{bmatrix} = \begin{bmatrix} \cos\gamma_y & -\sin\gamma_y \\ \sin\gamma_y & \cos\gamma_y \end{bmatrix} \begin{bmatrix} y \\ v \end{bmatrix}. \tag{5.31}$$

For the particular case of $\gamma_x = 0$ and $\gamma_y = \gamma$ the rotation only affects to the variables y and v,

$$S^{0,\gamma}(x, y) = \int \mathrm{d}u\mathrm{d}v\; W\left(x, y', u, v'\right). \tag{5.32}$$

We can integrate Eq. (5.32) with respect to the u variable expressing the WD in terms of the beam MI,

$$\begin{aligned} S^{0,\gamma}(x, y) &= \int \mathrm{d}x_1\mathrm{d}y_1\mathrm{d}u\mathrm{d}v\; \Gamma\left(x + \frac{1}{2}x_1, y' + \frac{1}{2}y_1, x - \frac{1}{2}x_1, y' - \frac{1}{2}y_1\right) \\ &\quad \times \exp\left[-\mathrm{i}2\pi\left(x_1 u + y_1 v'\right)\right] \\ &= \int \mathrm{d}x_1\mathrm{d}y_1\mathrm{d}v\; \Gamma\left(x + \frac{1}{2}x_1, y' + \frac{1}{2}y_1, x - \frac{1}{2}x_1, y' - \frac{1}{2}y_1\right) \\ &\quad \times \exp\left(-\mathrm{i}2\pi y_1 v'\right) \int \mathrm{d}u\; \exp\left(-\mathrm{i}2\pi x_1 u'\right) \\ &= \int \mathrm{d}y_1\mathrm{d}v\; \Gamma\left(x, y' + \frac{1}{2}y_1, x, y' - \frac{1}{2}y_1\right) \exp\left(-\mathrm{i}2\pi y_1 v'\right). \end{aligned} \tag{5.33}$$

[3] We have assumed $\sigma = 1$ m to simplify the equations.

The integration over y_1 yields the definition of the 2D WD of the 1D beam constructed by fixing the x variable on our original beam. As a result we obtain the tomographic projection relation for PSTC:

$$S^{0,\gamma}(x, y) = \int \mathrm{d}v \; W_x\left(y', v'\right). \tag{5.34}$$

One final caveat is that W_x does not correspond to a section of the beam WD, but rather to the WD projection in the u direction:

$$W_x\left(y', v'\right) = \int \mathrm{d}u \; W\left(x, y', u, v'\right). \tag{5.35}$$

5.8 Beam at the SLM Input Plane

In this section we calculate the MI of the beam incident to the SLM in the beam generation optical system introduced in Sect. 5.4. A fundamental Gaussian mode illuminates the input plane of the RGG diffuser. The diffuser rotates with sufficient speed to destroy the spatial coherence of the beam. Therefore, at the diffuser output plane we obtain a completely incoherent beam with Gaussian intensity profile described by the MI:

$$\Gamma_{\mathrm{RGG}}(\mathbf{r}_1, \mathbf{r}_2) = I_0 \exp\left(-\frac{2\pi}{w^2}\mathbf{r}_1^2\right)\delta(\mathbf{r}_1 - \mathbf{r}_2), \tag{5.36}$$

where I_0 is a power normalising constant and w is the waist of the input Gaussian beam. Notice that FL and CL form a telescope system that allows easily changing the beam waist by displacing the RGG diffuser.

The incoherent beam emerging from the diffuser is then propagated through the optical system between the RGG diffuser and the SLM. This propagation is described by the ABCD matrix resulting from multiplying the ABCD matrices of the constituent elemental systems, recall Sect. 1.2:

- a free-space propagation for distance $\mathrm{f_c} - d$,
- a quadratic phase associated with a convergent lens of focal length $\mathrm{f_c}$, and
- a free-space propagation for distance $\mathrm{f_c}$.

The resulting ABCD matrix is

$$\mathbf{T} = \begin{bmatrix} \mathbf{1} & \frac{\mathrm{f_c}}{\lambda}\mathbf{1} \\ \mathbf{0} & \mathbf{1} \end{bmatrix} \begin{bmatrix} \mathbf{1} & \mathbf{0} \\ -\frac{\lambda}{\mathrm{f_c}}\mathbf{1} & \mathbf{1} \end{bmatrix} \begin{bmatrix} \mathbf{1} & \frac{\mathrm{f_c}-d}{\lambda}\mathbf{1} \\ \mathbf{0} & \mathbf{1} \end{bmatrix} = \begin{bmatrix} \mathbf{0} & \frac{\mathrm{f_c}}{\lambda}\mathbf{1} \\ -\frac{\lambda}{\mathrm{f_c}}\mathbf{1} & \frac{d}{\mathrm{f_c}}\mathbf{1} \end{bmatrix}, \tag{5.37}$$

with an associated length constant $\sigma = \lambda$. Using the generalized Van Cittert-Zernike theorem [Goo00, Bor06], at the SLM input plane we observe a beam whose MI is calculated as

$$\Gamma_{\mathrm{SLM,in}}\left(\mathbf{r}_1, \mathbf{r}_2\right) = \frac{1}{\sigma^2} \int \mathrm{d}\mathbf{r}_1' \mathrm{d}\mathbf{r}_2' \, \Gamma_{\mathrm{RGG}}\left(\mathbf{r}_1', \mathbf{r}_2'\right) K_{\mathbf{T}}\left(\mathbf{r}_1', \mathbf{r}_1\right) K_{\mathbf{T}}^*\left(\mathbf{r}_2', \mathbf{r}_2\right), \quad (5.38)$$

where, c.f. Eq. (1.24),

$$K_{\mathbf{T}}\left(\mathbf{r}_\mathrm{i}, \mathbf{r}_\mathrm{o}\right) = \frac{-\mathrm{i}}{\lambda \mathrm{f_c}} \exp\left(-\frac{\mathrm{i}2\pi}{\lambda \mathrm{f_c}} \mathbf{r}_\mathrm{i} \cdot \mathbf{r}_\mathrm{o} + \frac{\mathrm{i}\pi d}{\lambda \mathrm{f_c^2}} \mathbf{r}_\mathrm{o}^2\right), \quad (5.39)$$

is the transformation kernel corresponding to $\mathbf{T}$.

In order to obtain the explicit expression for $\Gamma_{\mathrm{SLM,in}}$ we need to integrate Eq. (5.38). With the aid of the expression [Pru86, Bas05]

$$\int \mathrm{d}\mathbf{r} \, \exp\left(-\pi \mathbf{r} \cdot \mathbf{P}\mathbf{r} - \mathrm{i}2\pi \mathbf{r} \cdot \mathbf{q}\right) = \frac{1}{\sqrt{\det \mathbf{P}^{-1}}} \exp\left(-\pi \mathbf{q} \cdot \mathbf{P}^{-1}\mathbf{q}\right), \quad (5.40)$$

valid as long as $\mathbf{P}^{-1}$ exists and has non-null determinant, we find the result corresponding to Eq. (5.13):

$$\Gamma_{\mathrm{SLM,in}} = \frac{I_0 w^2}{\left(\lambda \mathrm{f_c}\right)^2} \exp\left[-\frac{\pi w^2}{2\left(\lambda \mathrm{f_c}\right)^2}\left(\mathbf{r}_1 - \mathbf{r}_2\right)^2 + \frac{\mathrm{i}\pi d}{\lambda \mathrm{f_c^2}}\left(\mathbf{r}_1^2 - \mathbf{r}_2^2\right)\right], \quad (5.41)$$

except that for Eq. (5.13) the normalisation constant I_0 includes the term $w^2/(\lambda \mathrm{f_c})^2$.

References

[Ali13] T. Alieva, J.A. Rodrigo, A. Cámara, E. Abramochkin, Partially coherent stable and spiral beams. J. Opt. Soc. Am. A **30**(11), 2237–2243 (2013)

[Alo11] M.A. Alonso, Wigner functions in optics: describing beams as ray bundles and pulses as particle ensembles. Adv. Opt. Photonics **3**(4), 272–365 (2011)

[Bas05] M.J. Bastiaans, T. Alieva, Generating function for Hermite-Gaussian modes propagating through first-order optical systems. J. Phys. A: Math. Gen. **38**(6), L73 (2005)

[Bor06] M. Born, E. Wolf, *Principles of Optics* (Cambridge University Press, Cambridge, 2006)

[Cám10a] A. Cámara, T. Alieva, J.A. Rodrigo, M.L. Calvo, Beam characterization via Wigner distribution projections, in *Proceedings of the 4th Tematic PRISMA Meeting*, (2010)

[Cám10b] A. Cámara, T. Alieva, J.A. Rodrigo, M.L. Calvo, Tomographic reconstruction of the Wigner distribution of non-separable beams, in *PIERS Proceedings*, Cambridge, 5–8 July 2010, pp. 526–530

[Cám11a] A. Cámara, T. Alieva, J.A. Rodrigo, M.L. Calvo, Optical systems and algorithms for phase-space tomography of one- and two-dimensional beams, in *Proceedings of the 22nd Congress of the ICO* (2011)

[Cám12a] A. Cámara, T. Alieva, *Experimental Reconstruction of the Mutual Intensity Based on Phase-Space Tomography*, Frontiers in Optics (Optical Society of America, New York, 2012)

[Cám13a] Alejandro Cámara, Jos A. Rodrigo, Tatiana Alieva, Optical coherenscopy based on phase-space tomography. Opt. Express **21**(11), 13169–13183 (2013)

[Cám13b] A. Cámara, J.A. Rodrigo, T. Alieva, *Phase-Space Tomography Towards Experimental Analysis of Partially Coherent Light*, Frontiers in Optics (Optical Society of America, New York, 2013)

[Dub99] F. Dubois, L. Joannes, J.-C. Legros, Improved three-dimensional imaging with a digital holography microscope with a source of partial spatial coherence. Appl. Opt. **38**(34), 7085–7094 (1999)

[Ger72] R.W. Gerchbrg, W.O. Saxton, A practical algorithm for the determination of phase from image and diffraction plane pictures. Optik **35**, 237–246 (1972)

[Goo00] J.W. Goodman, *Statistical Optics*, 1st edn. (Wiley, New York, 2000)

[Kol10] P. Kolman, R. Chmelík, Coherence-controlled holographic microscope. Opt. Express **18**(21), 21990–22003 (2010)

[Kui04] S. Kuiper, B.H.W. Hendriks, Variable-focus liquid lens for miniature cameras. Appl. Phys. Lett. **85**(7), 1128–1130 (2004)

[Mic04] P. Michel, C. Labaune, H.C. Bandulet, K. Lewis, S. Depierreux, S. Hulin, G. Bonnaud, V.T. Tikhonchuk, S. Weber, G. Riazuelo, H.A. Baldis, A. Michard, Strong reduction of the degree of spatial coherence of a laser beam propagating through a preformed plasma. Phys. Rev. Lett. **92**, 175001 (2004)

[Nat11] Adaptive optics kits, tabletop deformable mirrors and more. Nature Photonics **5**(1), 27–27 (2011). http://www.nature.com/nphoton/journal/v5/n1/full/nphoton.2010.296.html

[Pru86] A.P. Prudnikov, Y.A. Brychkov, O.I. Marichev, *Integral and Series*, vol. 1, Elementary Functions (Gordon and Breach, New York, 1986)

[Rad86] J. Radon, On the determination of functions from their integral values along certain manifolds. IEEE Trans. Med. Imaging **5**(4), 170–176 (1986)

[Ray94] M.G. Raymer, M. Beck, D.F. McAlister, Complex wave-field reconstruction using phase-space tomography. Phys. Rev. Lett. **72**(8), 1137–1140 (1994)

[Rod09] J.A. Rodrigo, T. Alieva, M.L. Calvo, Programmable two-dimensional optical fractional Fourier processor. Opt. Express **17**(7), 4976–4983 (2009)

[Rod11] J.A. Rodrigo, T. Alieva, A. Cámara, Ó. Martínez-Matos, P. Cheben, M.L. Calvo, Characterization of holographically generated beams via phase retrieval based on Wigner distribution projections. Opt. Express **19**(7), 6064–6077 (2011)

[Shi03] T. Shirai, A. Dogariu, E. Wolf, Mode analysis of spreading of partially coherent beams propagating through atmospheric turbulence. J. Opt. Soc. Am. A **20**(6), 1094–1102 (2003)

[Wan12] J. Wang, J.-Y. Yang, I.M. Fazal, N. Ahmed, Y. Yan, H. Huang, Y. Ren, Y. Yue, S. Dolinar, M. Tur, A.E. Willner, Terabit free-space data transmission employing orbital angular momentum multiplexing. Nat. Photonics **6**, 488–496 (2012)

[Zal00] Z. Zalevsky, D. Medlovic, H.M. Ozaktas, Energetic efficient synthesis of general mutual intensity distribution. J. Opt. A: Pure Appl. Opt. **2**(2), 83 (2000)

Chapter 6
Conclusions

This Thesis was devoted to the exploration of new non-interferometric techniques for the characterization of the coherence properties of optical beams. As a result, four different phase-space tomographic methods, some of which take advantage of beam symmetries, were established. Contrary to some recently proposed methods [Tia12, Wal12], all these techniques are coherence-agnostic, meaning that they make no assumptions on the beam level of coherence. Additionally, three optical setups were developed for their implementation. The Thesis provides valuable tools that reduce the complexity of analyzing the coherence picture of beams, making partially coherent beams more attractive for applications in science and technology.

Chapters 2, 3 and 4 presented characterization schemes for 1D, separable in Cartesian coordinates, and rotationally symmetric beams, respectively. Alternatively, a method for general beams, i.e. beams with no apparent symmetry, was introduced in Chap. 5. All proposed methods were theoretically, numerically, and experimentally studied to demonstrate their feasibility in real-world applications.

If the beam to characterize is 1D, or we are only interested in characterizing a 1D profile of it, all required information can be measured simultaneously using a RWD optical system. The beam WD, and therefore its MI, can be recovered from the fractional power spectra measured by a novel RWD setup composed by SLMs. Its experimental feasibility was demonstrated by recovering the WD of two example signals: window and chirped window. In addition, due to the dynamic nature of SLMs, our proposed RWD system allows improving the precision of the method at the expense of increasing the time of data acquisition.

In a first scheme, it allows taking multiple measurements, or shots, of different regions of the beam RWT. Assembling the shots into a complete multi-shot RWT results in a WD reconstruction with increased resolution.

A second scheme consists in taking a single-shot measurement, but only of a narrow region of the RWT instead of the whole angular range. This mode is specially useful to accurately determine certain beam characteristics that are localised in the RWT, like the chirp parameters of a multi-chirp signal.

A. Cámara, *Optical Beam Characterization via Phase-Space Tomography*,
Springer Theses, DOI 10.1007/978-3-319-19980-1_6

The rest of developed methods allow characterizing 2D beams. Assuming certain beam symmetries, which can be verified using the data required for beam coherence characterization, we established two simplified PST techniques for beams separable in Cartesian coordinates and rotationally symmetric beams.

Characterizing a separable beam is similar to characterizing two 1D beams. Each Cartesian coordinate uncouple into a 1D function that can be recovered independently. In Chap. 3 we proposed a novel technique that efficiently retrieves each of the composing 1D functions. It only requires measuring the beam antisymmetrical fractional power spectra, which can be acquired using the optical system composed of conventional elements that was proposed in Sect. 3.4. The method feasibility was experimentally demonstrated by characterizing a HG mode.

The separability test that was introduced in Sect. 3.3 allows verifying that a beam is separable in Cartesian coordinates. It requires the measurement of the beam antisymmetric fractional power spectra, so the same measurements can be used for the test and the characterization process.

RSBs, in particular fully and partially coherent optical vortices, are nowadays used for numerous applications, including but not limited to microparticle manipulation, optics communications, and imaging. They can be described by a MI that is invariant respect to rotations. In Chap. 4 we proposed a method specialized in characterizing RSBs. It only requires the already measured antisymmetric fractional power spectra. The feasibility of the technique was successfully proven in several simulated examples and in an experiment. Since the method only requires the beam antisymmetrical fractional power spectra, the same optical system based on conventional optical elements as for the separable case can be used.

Similarly to separable beams, we can verify that a beam is rotationally symmetric by applying the test introduced in Sect. 4.8. It also requires measuring the antisymmetrical fractional power spectra, so the test and characterization process for both separable and RSBs can be performed using the same data.

Applying a general characterization technique is the remaining option if the beam is neither separable nor rotationally symmetric. While a general characterization method can be used in this case, like the PST technique introduced in [Ray94], in Chap. 5 we proposed an alternative method that possesses two strong key features. First, the reconstruction algorithm has been specially designed for parallel computing. We showed that not only the acquisition and processing of projections can be performed simultaneously, but the actual projection processing steps can be executed concurrently. This provides a speed boost that places our technique closer to the real-time world.

The second advantage is that the MI of a 1D beam profile can be obtained from a subset of measurements. In the conventional PST method the beam MI is obtained from the whole beam WD, which in turn requires all projections to be acquired and processed. Conversely, we demonstrated that our method can process a subset of projections into a part of the beam MI, providing direct coherence information of the beam.

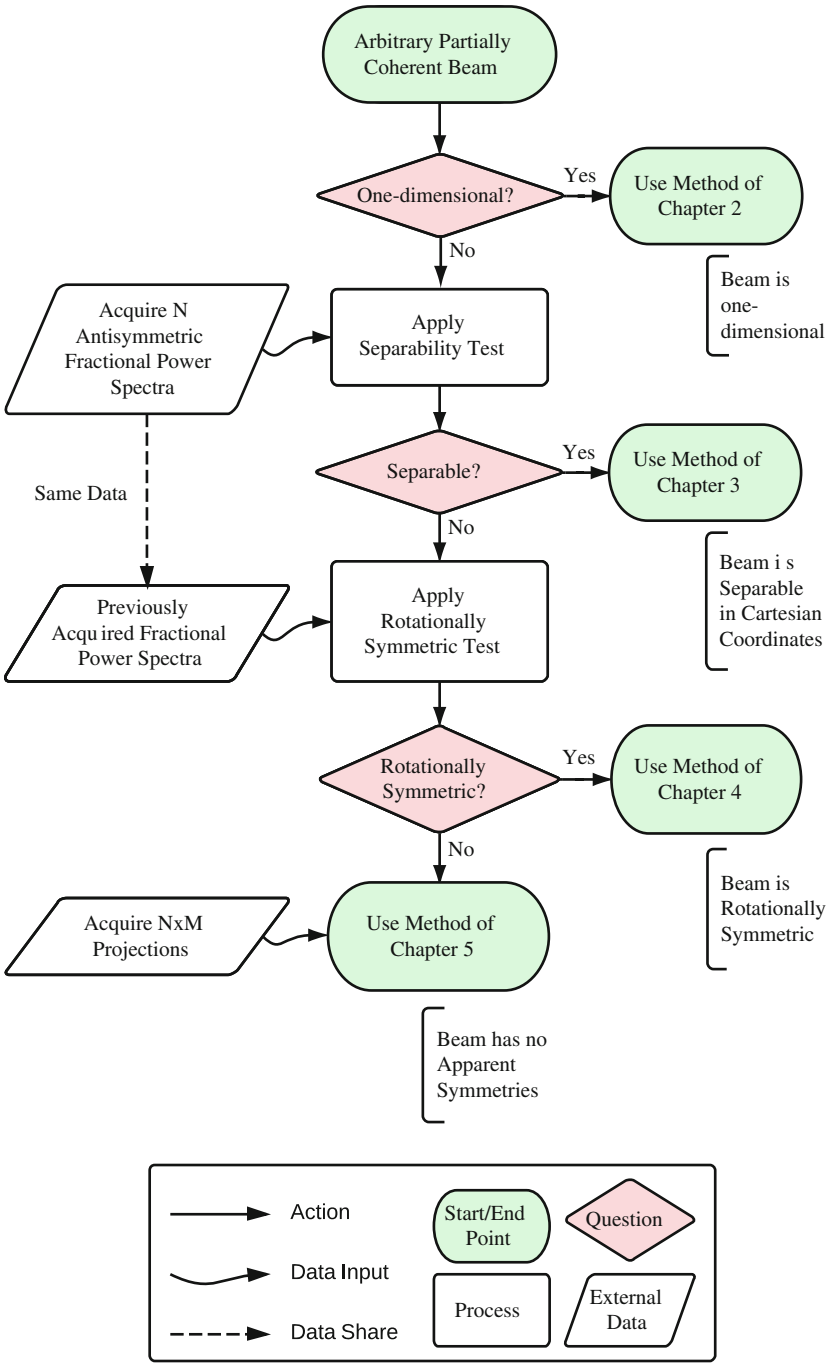

Fig. 6.1 Process diagram for the characterization of an a priori unknown beam based on its symmetries

This technique was experimentally proved in three different scenarios:

1. It was validated using coherent beams by comparing the results obtained with our method with the results of an alternative well-established method: IPR.
2. Its feasibility was demonstrated using partially coherent beams generated by illuminating a CGH with a GSMB. The obtained results were compared to the expected results. In particular, the width of the Gaussian degree of coherence modulus corresponded to the theoretical predictions.
3. Its feasibility was further demonstrated using partially coherent beams generated by incoherent sum of optical LG modes.

The WD projections required for this method, as well as the ones required for the rest of methods, can be obtained using the automatized programmable setup composed by two SLMs that was introduced in Sect. 5.3.

All these techniques can be thought of as part of the bigger characterization algorithm presented in Fig. 6.1. If we can safely assume certain beam symmetries, we can directly follow a specialized characterization method and use the optical system that best suits our requirements. For example, if we want to analyze 1D profiles of an unknown beam we can use our RWD setup and the method described in Chap. 2; if we want to analyze an optical vortex we can follow the instructions for RSBs of Chap. 4 and use the optical system formed by conventional elements described in Sect. 3.4. Otherwise, if we cannot make assumptions, we can use the more versatile setup composed by SLMs described in Sect. 5.3 and check for beams symmetries to discover the optimal characterization technique for the beam.

The proposed phase-space tomography techniques pave the way for a wider application of partially coherent light in different areas of knowledge such as imaging, optical communications, lithography, and atmosphere monitoring, to name a few.

References

[Ray94] M.G. Raymer, M. Beck, D.F. McAlister, Complex wave-field reconstruction using phase-space tomography. Phys. Rev. Lett. **72**(8), 1137–1140 (1994)

[Tia12] L. Tian, J. Lee, S.B. Oh, G. Barbastathis, Experimental compressive phase space tomography. Opt. Express **20**(8), 8296–8308 (2012)

[Wal12] L. Waller, G. Situ, J.W. Fleischer, Phase-space measurement and coherence synthesis of optical beams. Nature Photon. **6**(7), 474–479 (2012)

About the Author

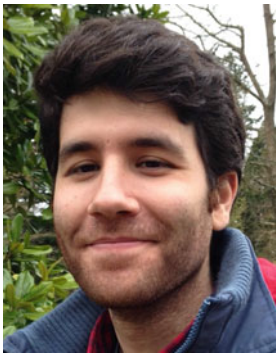

Alejandro Cámara grew up in Alicante, located in the sun-bathed east coast of Spain. He moved to the frenetic capital of Spain following his curiosity for how things work. In Madrid he finished a five-year degree in Physics and a M.Sc. in Fundamental Physics at Complutense University of Madrid (UCM). After five exciting years working in the Interdisciplinary Group of Computational Optics (GICO-UCM), he defended and passed with honours the Ph.D. thesis that you are reading right now. Today he's pursuing his dream of becoming an inspiring game developer in the United Kingdom, where he works as a Physics Software Engineer at Electronic Arts. What will he do tomorrow is still a mystery.

List of Publications

Patents

1. **Analizador de la estructura y coherencia espacial de haces luminosos**
   Tatiana Alieva, Alejandro Cámara, José A. Rodrigo
   Application P201200783, presented August 2nd, 2012

A. Cámara, *Optical Beam Characterization via Phase-Space Tomography*,
Springer Theses, DOI 10.1007/978-3-319-19980-1

Book Chapters

1. **Phase-Space Tomography of Optical Beams**
   Tatiana Alieva, Alejandro Cámara, José A. Rodrigo, María L. Calvo
   Optical and Digital Image Processing, (eds) G. Cristóbal, P. Schelkens, H. Thienpont (Wiley-VCH, 2011)
2. **Wigner distribution moments for beam characterization**
   Tatiana Alieva, Alejandro Cámara, Martin J. Bastiaans
   Mathematical Optics: Classical, Quantum, and Computational Methods, (eds) V. Lakshminarayanan, M. L. Calvo, T. Alieva (CRC-Press, 2013)

Articles and Letters

1. **Phase space tomography reconstruction of the Wigner distribution for optical beams separable in Cartesian coordinates**
   Alejandro Cámara, Tatiana Alieva, José A. Rodrigo, María L. Calvo
   Journal of the Optical Society of America A**26**(6), 1301–1306, 2009
2. **Propagation of broken stable beams**
   Alejandro Cámara, Tatiana Alieva
   Journal of Modern Optics **58**, 743–747, 2011
3. **Phase-space tomography with a programmable Radon–Wigner display**
   Alejandro Cámara, Tatiana Alieva, José A. Rodrigo, María L. Calvo
   Optics Letters **36**, 2441–2443, 2011
   Selected for the Virtual Journal of Biomedical Optics
4. **Characterization of holographically generated beams via phase retrieval based on Wigner distribution projections**
   José A. Rodrigo, Tatiana Alieva, Alejandro Cámara, Óscar Martínez-Matos, Pavel Cheben, María L. Calvo
   Optics Express **19**, 6064–6077, 2011
5. **Optical coherenscopy based on phase-space tomography**
   Alejandro Cámara, José A. Rodrigo, Tatiana Alieva
   Optics Express **21**, 13169–13183, 2013 Selected as OSA image of the week in May 2013
6. **Partially coherent stable and spiral beams**
   Tatiana Alieva, José A. Rodrigo, Alejandro Cámara, Eugeny G. Abramochkin
   Journal of the Optical Society of America A **30**, 2237–2243, 2013
   Top OSA downloaded article in October and November 2013
7. **Phase-space tomography for characterization of rotationally symmetric beams**
   Alejandro Cámara, Tatiana Alieva, Izan Castro, José A. Rodrigo
   Journal of Optics **16**, 015705, 2014
   Selected as paper of the week on January 2014
   Highlighted in IOPScience LabTalk